



Universität Hamburg

DER FORSCHUNG | DER LEHRE | DER BILDUNG

Eclipsing Time Variations from 3D Magnetohydrodynamical Simulations

Dissertation

zur Erlangung des Doktorgrades

an der Fakultät für Mathematik, Informatik und Naturwissenschaften

Fachbereich Physik der Universität Hamburg

vorgelegt von

Felipe Hernán Navarrete Noriega

Hamburg

2023

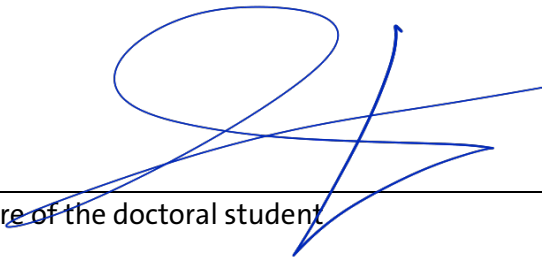
Gutachter/innen der Dissertation:	: Prof. Dr. Robi Banerjee
	: Dr. Petri Käpylä
Zusammensetzung der Prüfungskommission	: Prof. Dr. Robi Banerjee
	Prof. Dr. Peter Hauschildt
	Dr. Petri Käpylä
	Prof. Dr. Jochen Liske
	Prof. Dr. Dominik Schleicher
Vorsitzende/r der Prüfungskommission	: Prof. Dr. Jochen Liske
Datum der Disputation	: 16.08.2023
Vorsitzender des Fach-Promotionsausschusses PHYSIK	: Prof. Dr. Günter H. W. Sigl
Leiter des Fachbereichs PHYSIK	: Prof. Dr. Wolfgang J. Parak
Dekan der Fakultät MIN	: Prof. Dr.-Ing Norbert Ritter

Declaration on oath

I hereby declare in lieu of oath that I have written this dissertation myself and that I have not used any auxiliary materials or sources other than those indicated.

Hamburg, 11.05.2023

Signature of the doctoral student

A handwritten signature in blue ink, consisting of a large, stylized loop followed by several sharp, intersecting strokes.

To my mom

Contents

Acknowledgements	ix
Abstract	xi
Zusammenfassung	xiii
1 Introduction	1
1.1 Stellar magnetism	1
1.1.1 Observational evidence of stellar dynamos	3
1.1.2 Stellar dynamo simulations	6
1.2 Planets Around Close Binary Stars	8
1.2.1 Post-common-envelope binaries	8
1.2.2 ETVs and the planetary hypothesis	11
1.3 Period Variations from Magnetic Activity	13
1.3.1 The Applegate mechanism	14
1.3.2 Lanza mechanism	17
2 Aims and methods	21
2.1 Gravitational quadrupole moment from dynamo simulations	21
2.2 Numerical Setup	22
2.2.1 Initial conditions	23
2.2.2 Boundary conditions	25
2.2.3 Temporal evolution	25
3 Paper I	29
4 Paper II	45
5 Paper III	53
6 Conclusions and Outlook	63

List of Figures

1.1	Schematics of α^2 , $\alpha\Omega$, and $\alpha^2\Omega$ dynamos. Here, $\overline{\mathbf{B}}_{\text{pol}}$ is a mean poloidal field, and $\overline{\mathbf{B}}_{\text{tor}}$ is a mean toroidal field.	3
1.2	Sunspots position in latitude as a function of time. Image credits to NASA.	4
1.3	X-ray luminosity vs Rossby number for 824 solar and late-type stars. Figure from Wright et al. (2011).	5
1.4	Schematics of the common-envelope phase. The dashed vertical line denotes the Roche equipotential surface. Any material past this point will be pulled by the gravitational potential of the other star. (a) The more massive star, marked as “1”, enters the red giant (RG) branch. (b) As the star evolves, it expands past the Roche equipotential surface. (c) The RG fills its Roche lobe and the mass transfer begins. (d) The expansion of the RG continues and is faster than the mass than can be accreted. (e) A CE is formed. Image by Philip D. Hall and reproduced here under CC BY-SA 3.0	9
1.5	Simulation of a common envelope evolution. The “+” sign is the position of the core of the red giant (RG) and the “x” sign is the position of the secondary star. The gas density, which represents the convective envelope of the RG, is shown with the color map. After a period of 110 days, the binary went from a separation of about 25 solar radius to less than 10 solar radius. Figure from Ohlmann et al. (2016).	10
1.6	Observed-minus-calculated (O–C) diagram of the post-common-envelope binary NN Ser. The observations, shown as yellow and green data points, are fitted with the black line. The two green lines are the individual contributions to the model and are interpreted as circumbinary planets. Figure from Beuermann et al. (2010).	11
1.7	Expected period variations as a function of zero-age-main-sequence (ZAMS) mass. Figure from Völschow et al. (2018).	17

- 1.8 Illustration of the configuration considered by Lanza (2020). The plane xy lies on the plane of the binary, as well as ss' . The axis x points towards the companion star, shown in green, and s coincides with the axis of symmetry of the flux tube, shown in yellow with angular radius of θ_0 . The angle α is the angular separation between x and s . The effects of the flux tube can be modeled as two point masses A and A' which produce the forces F and $F_{A'}$, respectively, on the companion. Figure from Lanza (2020). 18
- 2.1 Initial (solid lines) and final (dashed lines) radial profiles of entropy (upper left), temperature (upper right), pressure (bottom left) and density (bottom right), of a typical run of the spherical wedge setup. All quantities have been normalized by the value at the bottom of the domain. 24
- 2.2 Temporal evolution of the rms velocity (top left), rms magnetic field (top right), thermal energy (bottom left), and gravitational quadrupole moment (bottom right). Each one is characterized by its own growth timescale and steady state. 26

Acknowledgements

I would like to thank Prof. Robi Banerjee for giving me the opportunity to come to his group at the Observatory of Hamburg. The support, freedom, and resources that I have received here have been of infinite importance to my development as a scientist and as a person. Thanks to all of my friends who I have made here for the laughs and conversations.

I also would like to give my most grateful thanks to Prof. Dominik Schleicher and Dr. Petri Käpylä for their constant support and guidance. Our weekly online and sporadic in-person meetings have been of uttermost importance for this thesis.

Also thanks to Prof. Axel Brandenburg for taking me as a visiting PhD student. Working at the relaxed and scientifically encouraging atmosphere of Nordita was a great experience.

Very kind and special thanks to my beloved girlfriend Chiara for her constant company and patience during my time in Hamburg.

Last but certainly not least, a huge thanks to my brothers Eduardo and Pablo and to my parents Luis and Carmen. This thesis is dedicated to my mother Carmen who sadly passed away in 2022 during my studies and unfortunately could not see the completion of my thesis.

Abstract

Magnetic fields are ubiquitous in the Universe. In particular, the magnetic activity of the Sun has been observed for centuries and studied for more than a century. Nowadays we know that most stars are magnetized. Yet, the mechanism by which magnetic fields are sustained is not well understood. Dynamo theory, which describes how magnetic fields are amplified and sustained, has mostly been used to explain solar phenomena with moderate success.

A field where dynamo theory has hitherto not been exploited is in binary stars. Most of our knowledge of stellar structure and evolution come from carefully inferring stellar parameters from binaries. Measures of magnetic fields in stars are much more difficult to obtain, therefore limiting our knowledge thereof. A possibility to overcome this is encountered in close binaries via gravitational quadrupole variations which arise from density fluctuations of magnetic origin. This is observed as periodic eclipsing time variations in some close binaries. Two mechanisms stand out as potential explanations, namely the Applegate and Lanza mechanisms.

This thesis expands previous analytical works by solving the magnetohydrodynamic equations in a convective shell, representing a Sun-like star. It is found that the density fluctuations are too small to explain the observations with the original Applegate mechanism. However, when the magnetic field has a strong non-axisymmetric component, the Lanza mechanism can predict the observations to an order-of-magnitude approximation.

The simplicity of the Lanza mechanism allows to overcome the problems of the Applegate mechanism and may offer a new way of studying stellar magnetic fields by measurements of eclipsing time variations in close binaries.

Zusammenfassung

Magnetfelder sind allgegenwärtig im Universum. Insbesondere wurde die magnetische Aktivität der Sonne seit Jahrhunderten beobachtet und seit über einem Jahrhundert erforscht. Heutzutage wissen wir, dass die meisten Sterne magnetisiert sind. Dennoch ist der Mechanismus, durch den Magnetfelder aufrechterhalten werden, nicht gut verstanden. Die Dynamotheorie, die beschreibt, wie Magnetfelder verstärkt und aufrechterhalten werden, wurde hauptsächlich verwendet, um solare Phänomene mit mäßigem Erfolg zu erklären.

Ein Bereich, in dem die Dynamotheorie bisher kaum genutzt wurde, sind Doppelsterne. Ein Großteil unseres Wissens über die Struktur und Evolution von Sternen stammt aus sorgfältigem Ableiten von stellaren Parametern aus Doppelsternen. Messungen von Magnetfeldern in Sternen sind jedoch viel schwieriger zu erhalten, was unser Wissen darüber einschränkt. Eine Möglichkeit, dies zu überwinden, findet sich in engen Doppelsternen über Gravitationsquadrupolvariationen, die aus Dichteschwankungen magnetischen Ursprungs resultieren. Dies wird als periodische Veränderungen der Verfinsterungszeit in einigen engen Doppelsternen beobachtet. Zwei Mechanismen zeichnen sich als potenzielle Erklärungen ab, nämlich der Applegate- und der Lanza-Mechanismus.

Diese Arbeit erweitert vorherige analytische Arbeiten, indem die magnetohydrodynamischen Gleichungen in einer konvektiven Schale gelöst werden, die einen sonnenähnlichen Stern darstellt. Es wird festgestellt, dass die Dichteschwankungen mit dem ursprünglichen Applegate-Mechanismus zu gering sind, um die Beobachtungen zu erklären. Wenn das Magnetfeld jedoch eine starke nichtachsensymmetrische Komponente hat, kann der Lanza-Mechanismus die Beobachtungen mit einer Genauigkeit von etwa einer Größenordnung vorhersagen.

Die Einfachheit des Lanza-Mechanismus ermöglicht es, die Probleme des Applegate-Mechanismus zu überwinden, und könnte einen neuen Weg bieten, um stellare Magnetfelder durch Messungen von Verfinsterungszeitvariationen in engen Doppelsternen zu untersuchen.

Chapter 1

Introduction

Magnetic fields in stars have been historically studied mostly in the Sun. It started with the observations of sunspots by Galileo Galilei¹, although little he knew about their origin. The solar cycle, now known to reproduce the butterfly diagram, was identified for the first time during the 1843 by Samuel Schwabe. By the second half of the 19th century, solar flares were already observed and spectroscopy was being used on the Sun. In the early 20th century, George Hale had applied the technique known as Zeeman effect to solar observation. He showed that the sunspots are magnetic structures in the photosphere which intensified the research in the field. By 1955, Eugene Parker published the first systematic study of hydromagnetic dynamos applied to the Sun (Parker 1955).

By now, we know that most stars are magnetically active all along the main sequence and beyond. The theory that explains the generation and maintenance of a magnetic field is called dynamo theory. There exists a plethora of different dynamo mechanism, such as slow and fast dynamos, small scale and large scale dynamos, $\alpha\Omega$, $\alpha^2\Omega$, and α^2 dynamos. Several comprehensive reviews exist that address the details of these dynamos such as Brandenburg and Subramanian (2005), Rincon (2019), and Tobias (2021).

1.1 Stellar magnetism

It is widely accepted that differential rotation plays a key role in generating and maintaining stellar magnetic fields. Equally accepted is the key role played by the kinetic helicity. To begin explaining this, we shall start with the induction equation,

$$\frac{\partial \mathbf{B}}{\partial t} = \nabla \times (\mathbf{u} \times \mathbf{B}) - \nabla \times (\eta \nabla \times \mathbf{B}), \quad (1.1)$$

¹Although Thomas Harriot, David Fabricius, and Johannes Fabricius observed the Sun before Galileo Galilei did, they did not record or publish drawings or detailed notes about them.

which describes the temporal evolution of a magnetic field \mathbf{B} , and where \mathbf{u} is the velocity field and η is the magnetic diffusivity. We can construct the mean-field induction equation by first introducing the Reynolds decomposition

$$\mathbf{u} = \bar{\mathbf{u}} + \mathbf{u}', \quad (1.2)$$

$$\mathbf{B} = \bar{\mathbf{B}} + \mathbf{B}', \quad (1.3)$$

where overlines denote averages and primes denote fluctuations. By applying this to Eq. 1.1, the mean-field induction equation can be written as

$$\frac{\partial \bar{\mathbf{B}}}{\partial t} = \nabla \times (\bar{\mathbf{U}} \times \bar{\mathbf{B}} + \bar{\boldsymbol{\mathcal{E}}} - \eta \bar{\mathbf{J}}), \quad (1.4)$$

where $\bar{\mathbf{J}} = \nabla \times \bar{\mathbf{B}}$ is the mean field current density, and $\bar{\boldsymbol{\mathcal{E}}} = \overline{\mathbf{u}' \times \mathbf{B}'}$ is the mean electromotive force (EMF), which can be recast as (Krause and Rädler 1980; Rincon 2019)

$$\bar{\mathcal{E}}_i = a_{ij} \bar{B}_j + b_{ijk} \partial_j \bar{B}_k, \quad (1.5)$$

$$\bar{\mathcal{E}}_i = \alpha_{ij} \bar{B}_j + (\boldsymbol{\gamma} \times \bar{\mathbf{B}})_i - \beta_{ij} (\nabla \times \bar{\mathbf{B}})_j - [\boldsymbol{\delta} \times (\nabla \times \bar{\mathbf{B}})]_i - \frac{1}{2} \kappa_{ijk} (\nabla_j \bar{B}_k + \nabla_k \bar{B}_j), \quad (1.6)$$

where

$$\alpha_{ij} = \frac{1}{2} (a_{ij} + a_{ji}), \quad (1.7)$$

$$\beta_{ij} = \frac{1}{4} (\epsilon_{ikl} b_{jkl} + \epsilon_{jkl} b_{ikl}), \quad (1.8)$$

$$\gamma_i = -\frac{1}{2} \epsilon_{ijk} a_{jk}, \quad (1.9)$$

$$\delta_i = \frac{1}{4} (b_{jji} - b_{jij}), \quad (1.10)$$

$$\kappa_{ijk} = -\frac{1}{2} (b_{ijk} + b_{ikj}), \quad (1.11)$$

and ϵ_{ijk} is the Levi-Civita symbol. The α effect amplifies the magnetic field via helical flows. β is similar to η in that it acts as a turbulent diffusion. The γ effect is interpreted as a turbulent pumping of $\bar{\mathbf{B}}$. The δ effect, also called the Rädler effect, is a term that can lead to dynamo action in nonhelical flows with shear. Lastly, there is no clear interpretation of κ .

Generally speaking, in the presence of differential rotation (shearing) there is also the contribution of the Ω effect, which enters in the RHS of the induction Eq. 1.4 as $\bar{\mathbf{B}} \cdot \nabla \bar{\mathbf{u}}$, but it cannot maintain a magnetic field on its own. This effect also amplifies

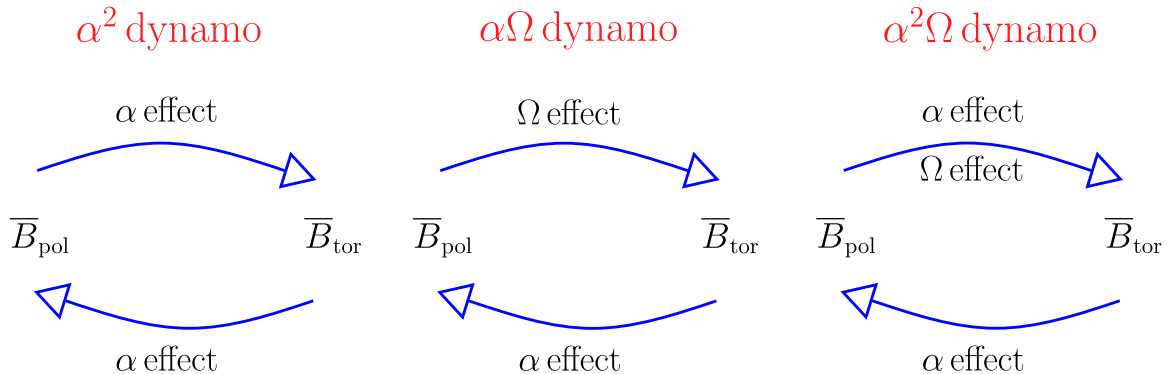


Figure 1.1: Schematics of α^2 , $\alpha\Omega$, and $\alpha^2\Omega$ dynamos. Here, $\overline{B}_{\text{pol}}$ is a mean poloidal field, and $\overline{B}_{\text{tor}}$ is a mean toroidal field.

the magnetic field like the α effect but via shearing. The interplay between these two effects gives rise to a family of three types of dynamos. Namely, the α^2 , $\alpha\Omega$, and $\alpha^2\Omega$ dynamos. A simple schematic of these dynamos is shown in Fig. 1.1. Starting from a mean poloidal field $\overline{B}_{\text{pol}}$, the α effect can convert a $\overline{B}_{\text{pol}}$ from and to a toroidal field $\overline{B}_{\text{tor}}$ and vice versa. In the presence of differential rotation, the Ω effect stretches the poloidal magnetic field lines differentially. For example, the rotation of the Sun is faster at the equator than in the poles and it converts $\overline{B}_{\text{pol}}$ to $\overline{B}_{\text{tor}}$. The α effect converts it back to $\overline{B}_{\text{pol}}$ by means of flow helicity which twists and breaks the toroidal field.

This simple qualitative description hides a great deal of complexity behind it. For example, there is a closure problem when attempting to solve the mean field induction equation. This is because, in order to solve it, we should express it in terms of mean quantities only but the fluctuating field appears in $\overline{\mathcal{E}}$. There is also the problem that the dynamics and energetics most relevant to dynamos are hidden under the stellar surfaces. As such, we have to resort to drawing conclusions based on what theories and simulations tell us about what happens in the stellar convection zone, and then attempt to link this to surface phenomena and then to observations of magnetic fields on the stellar surface. Alternatively, we can also infer the internal dynamics of stars by means of astero/helioseismology (Hanasoge, Gizon, and Sreenivasan 2016).

1.1.1 Observational evidence of stellar dynamos

Despite the great challenges related to studying stellar dynamos, we have observational hints of an internal mechanism that gives rise to the observed magnetic phenomena at the surface of stars. Most of it comes from observations of our nearest star, the Sun. It is characterized by cool spots with a particularly strong magnetic field, know

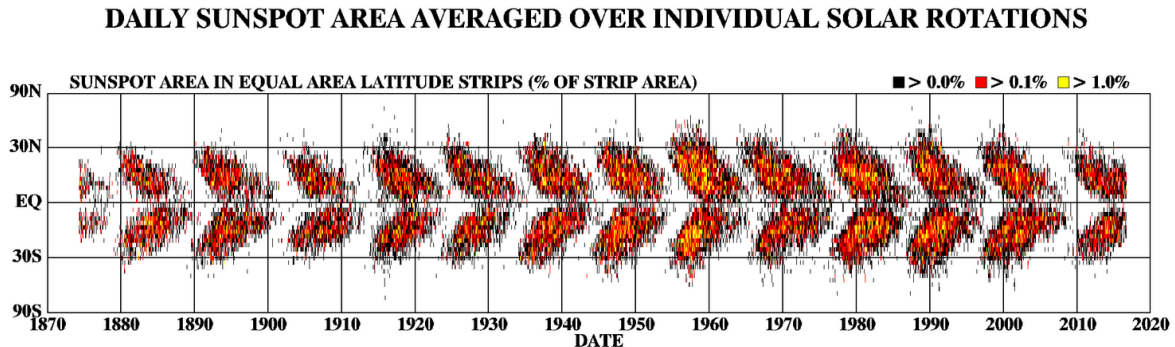


Figure 1.2: Sunspots position in latitude as a function of time. Image credits to NASA.

as sunspots, which start appearing at mid latitudes and at lower latitudes as the cycle progresses. The tracking of this migration pattern as a function of time and latitude is known as “butterfly diagram”, which is shown in Fig. 1.2. The cycle starts with sunspots appearing at mid latitudes ($\pm 30^\circ$) and newer sunspots appear at lower and lower latitudes with an average period of 11 years. This is only half the cycle as the polarity of the magnetic field over each hemisphere also changes every 11 years, and so the solar magnetic cycle is 22 years long. Another feature of the Sun are solar flares, which involve the release of at least 10^{20} J from the surface. It is believed that this release of energy is related to magnetic reconnection in the sunspots as flares usually coincide with spots. Furthermore, coronal mass ejections (CME) usually follow solar flares.

While a huge amount of detailed data exists for the Sun with a long baseline, this is not the case for other stars. Thus, for stars other than the Sun we have to deal with sparse data with a much lower level of detail as compared with the one of the Sun. For example, butterfly diagrams for other stars were only recently obtained for ϵ Eridani and 61 Cygni A by Jeffers et al. (2022). Both stars were found to have Sun-like characteristics, with two chromospheric cycles of ~ 3 and ~ 13 years for ϵ Eridani. It is yet unknown whether dynamo waves are a common feature among Sun-like stars.

A few interesting scaling properties can be identified. Wright et al. (2011) performed an analysis of more than 800 late-type main-sequence stars. It was found that the X-ray luminosity scales with the Rossby number (Ro), defined as

$$Ro = \frac{P_{\text{rot}}}{\tau_c}, \quad (1.12)$$

where P_{rot} is the rotation period of the star and τ_c is the convective turnover time. It was found that X-ray luminosity increases with decreasing Rossby number down to $Ro \sim 0.1$ and a saturated regime was found for lower values of Ro (see Fig. 1.3). Subsequently, Wright et al. (2018) extended this study by adding fully convective stars to the analysis

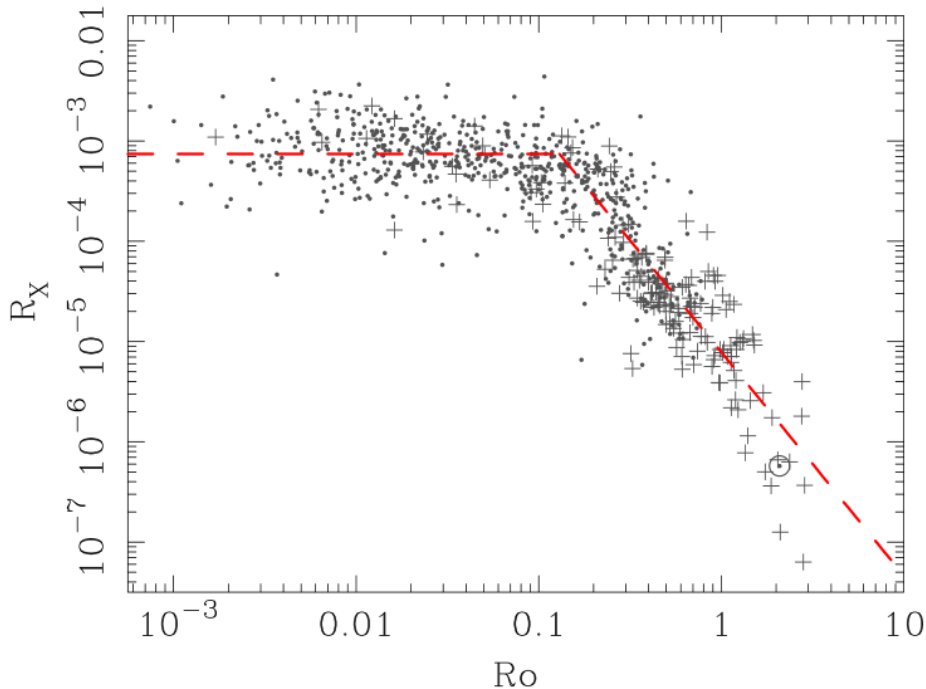


Figure 1.3: X-ray luminosity vs Rossby number for 824 solar and late-type stars. Figure from Wright et al. (2011).

and found that they follow the same scaling law. This is a very interesting result which might have deep theoretical implications. In the Sun, it was believed that the thin transition region between the radiative core and the convective envelope, called tachocline, was an important ingredient for the dynamo. This is because the tachocline is a region of strong shear and thus important for converting $\overline{\mathbf{B}}_{\text{pol}}$ to $\overline{\mathbf{B}}_{\text{tor}}$. However, due to the absence of tachoclines in fully convective stars and because they follow the same scaling properties, this might mean that a tachocline is not important for dynamos. To test this picture even further Lehtinen et al. (2020) identified a dependence of magnetic activity of post-main-sequence stars with Ro , The scaling is such that magnetic activity, which is derived by using chromospheric emissions of Ca II H and K as a proxy, increases with decreasing Ro , such that main-sequence and giant stars follow the same sequence.

One could question the link between the above results and the dynamo that takes place in the convective zone. Indeed, it is not yet clear how the magnetic field strength connects to chromospheric activity and/or X-ray emissions. A more direct measurement was presented by Reiners et al. (2022). The average surface magnetic field strength was derived for 292 low-mass main-sequence stars and a similar result to that of Wright and Drake (2016) was found. It now seems more clear that rotation

and differential rotation, a key ingredient of dynamo theory, is very well correlated to magnetic field strength. However, the reason for the scaling and saturated regimes are not understood.

Overall, there are many aspects of stellar magnetism what are not yet explained. It is currently not possible to directly access the interior of stars, thus making a direct comparison with results from dynamo theory unfeasible. We can attempt to bridge this gap with stellar dynamo simulations and look for similarities between the two.

1.1.2 Stellar dynamo simulations

Simulations of stellar dynamos can be divided in two main groups. These are:

1. (semi-)global simulations. Here, either the full extent of the convective zone or a large part of it is simulated.
2. local boxes. In this case, Cartesian box in the stellar region of interest is simulated. The box is small compared to the size of the star.

Both approaches come with pros and cons. The nature of global simulations implies that the parameter regime is far away from real stars. This is because the characteristic length scale, the stellar radius, greatly reduces dimensionless numbers such as the Reynolds number. Thus, even larger grid resolutions are needed to increase these numbers. However, in this case the gain is that global dynamics and global magnetic field features are captured. Examples of this type of simulations can be found in Dobler, Stix, and Brandenburg (2006), Browning et al. (2006), Käpylä et al. (2013), Hotta and Kusano (2021), and Popovas, Nordlund, and Szydlarski (2022). Local boxes have a much smaller characteristic length and in general the parameters can be pushed more to real stars, although in general they are still very far away (Kupka and Muthsam 2017). However, they come with the loss of global phenomena. Usually, these type of simulations are targeted towards more fundamental aspects of dynamo theory. Some examples include Brandenburg (2001) and Bushby et al. (2018).

This thesis makes use of global dynamo simulations for reasons that will become clear in the next chapters. Some aspects and results, with special emphasis on long standing problems of this type of simulations are summarized in the following to give a sense of what the current status of the field is.

Several dimensionless parameters are used to characterized convective flows with rotation and magnetic fields. The most important ones are the Coriolis number, fluid and magnetic Reynolds numbers, and fluid and magnetic Prandtl numbers. These are defined as

$$\text{Co} = \frac{\tau_c}{P_{\text{rot}}}, \quad \text{Re} = \frac{uL}{\nu}, \quad \text{Re}_M = \frac{uL}{\eta}, \quad \text{Pr} = \frac{\nu}{\chi}, \quad \text{Pr}_M = \frac{\nu}{\eta}, \quad (1.13)$$

where u is a typical flow velocity at a length scale L , ν is the viscosity of the flow, η is the magnetic diffusivity, and χ is the thermal diffusivity.

It is not exactly clear what any of these numbers are in the Sun. It is estimated that, in the convection zone, they range between (see Jermyn et al. 2022)

$$\text{Co} \sim 10^{-2} \dots 10, \quad (1.14)$$

$$\text{Re} \sim 10^{12} \dots 10^{14}, \quad (1.15)$$

$$\text{Re}_M \sim 10^6 \dots 10^{10}, \quad (1.16)$$

$$\text{Pr} \sim 10^{-6} \dots 10^{-3}, \quad (1.17)$$

$$\text{Pr}_M \sim 10^{-6} \dots 10^{-2}. \quad (1.18)$$

However, we can not achieve these parameters with simulations, with the only exception being the Coriolis number. The gap is as large as several order of magnitude and essentially boils down to the huge range of physically relevant scales in stars. For example, the magnetic Prandtl number is a property of the fluid and does not depend on the flow properties such as velocity. It can be seen as the scale separation between the kinetic and magnetic spectra. For very small Pr_M , this means that a lot of the magnetic energy is contained at scales larger than any scale relevant to turbulence. If we want to capture both the turbulent scale and scales relevant to magnetic fields, we would need a tiny grid spacing and so the timestep becomes infeasibly small. A similar issue is encountered with the magnetic Reynolds number. Due to the small values of η in the convective zone, Re_M is very large. These values are not possible to capture in simulations due to severely reducing the timestep. Furthermore, the resolution would have to be infeasibly high.

As a consequence, a few approaches are used in simulations to overcome these issues. For example, the simulations of Hotta and Kusano (2021) artificially reduce the speed of sound which would otherwise also negatively affect the timestep. More common approaches are the usage of the anelastic or Boussinesq equations. The anelastic equations simplify hydrodynamic equations by assuming that the density is a function of temperature and pressure only, and fluctuations of the density field are neglected. On the other hand, the Boussinesq approximation includes density fluctuations but assumes that they do not have an impact on the flow other than being important for buoyancy. These are accurate only in the deep convection zone where density variations are indeed small enough to justify both approaches.

Every approximation above is just a different approach to avoid solving the fully compressible MHD equations. A different approach is the so-called ‘‘enhanced luminosity’’ method. Here, the input luminosity of the model is artificially enhanced by several orders of magnitude. This has the effect to increase the Mach number so that it becomes computationally feasible. The thermal relaxation timescale (Kelvin-Helmholtz timescale) is also greatly reduced such that the required computational time to reach

the thermally saturated regime is achievable. It comes with the cost of increasing the velocity of the flow and so several timescales such as the convective timescale are shortened. To compared with real stars, a scaling procedure is employed (e.g. Käpylä et al. 2020).

1.2 Planets Around Close Binary Stars

It can be difficult to distinguish between planets and magnetic activity. This is especially difficult in post common envelope binaries (PCEBs), where eclipsing time variations (ETVs) can be interpreted as either being produced by planets or magnetic activity. Before turning to the observations and theory behind ETVs induced by magnetic activity in PCEBs, some aspects of planets around close binaries are presented.

1.2.1 Post-common-envelope binaries

PCEBs are close binaries composed of a white dwarf (the primary star) and a main-sequence star (the secondary star). In general, the main-sequence star is a red dwarf and a typical binary separation is very small, of the order of a solar radius and smaller. This small separation results in very short orbital periods which are generally shorter than a day. Furthermore, the intrinsic differences between the stellar parameters of the white dwarf and the red dwarf can be exploited to derive these parameters with great precision through eclipses.

The theory behind the formation of such short period binaries was proposed by Paczynski (1976) and a schematics of the process is shown in Fig. 1.4 Before the common envelope (CE) phase, the binary had a wider separation of the order of 1 AU. Due to differences in the mass between the two stars, the one with larger mass evolves faster and thus reaching the giant branch sooner. When the radius of the now red giant (RG) is larger than 1 AU, the secondary star is engulfed in the convective envelope of the RG. As the secondary star is now surrounded by a medium, the drag forces convert orbital energy into thermal energy. The secondary is now forced to move inwards towards the core of the RG and the envelope is slowly ejected from the system. If there is no merger between the companion and the RG core (i.e. white dwarf), then eventually a PCEB is revealed. In Fig. 1.5 a simulation of a common envelope phase is shown (Ohlmann et al. 2016). It should be noted that the timescale of this process is of the order of a few hundred days. As such, it is extremely unlikely to observe a CE in action. PCEBs are also believed to be the progenitors of type Ia supernovae. The latter would take place once the secondary star enters the RG branch and mass transfer into the white dwarf begins.

Binary stars, and in particular PCEBs, are of great interest in astrophysics. They can be used for precise measurements of stellar parameters and to test extreme astro-

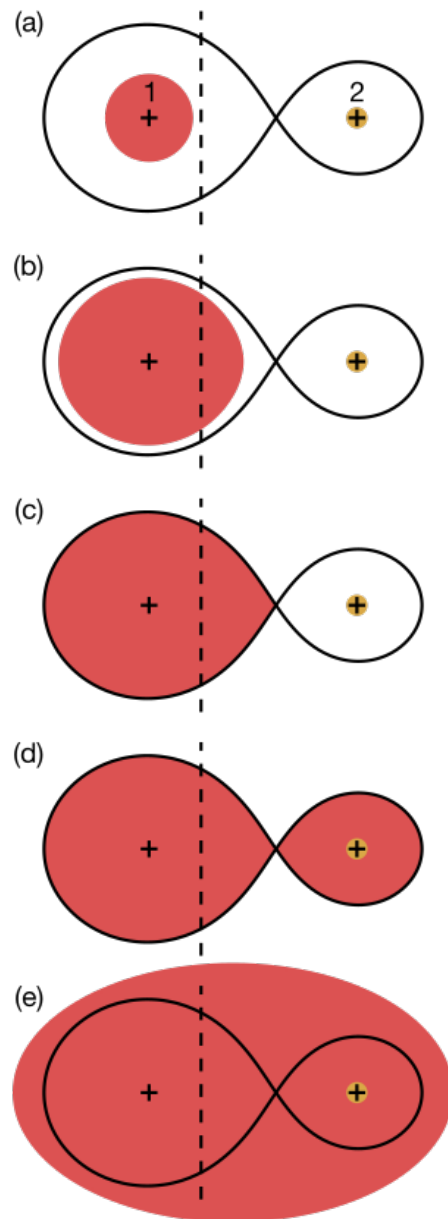


Figure 1.4: Schematics of the common-envelope phase. The dashed vertical line denotes the Roche equipotential surface. Any material past this point will be pulled by the gravitational potential of the other star. (a) The more massive star, marked as “1”, enters the red giant (RG) branch. (b) As the star evolves, it expands past the Roche equipotential surface. (c) The RG fills its Roche lobe and the mass transfer begins. (d) The expansion of the RG continues and is faster than the mass than can be accreted. (e) A CE is formed. Image by Philip D. Hall and reproduced here under CC BY-SA 3.0

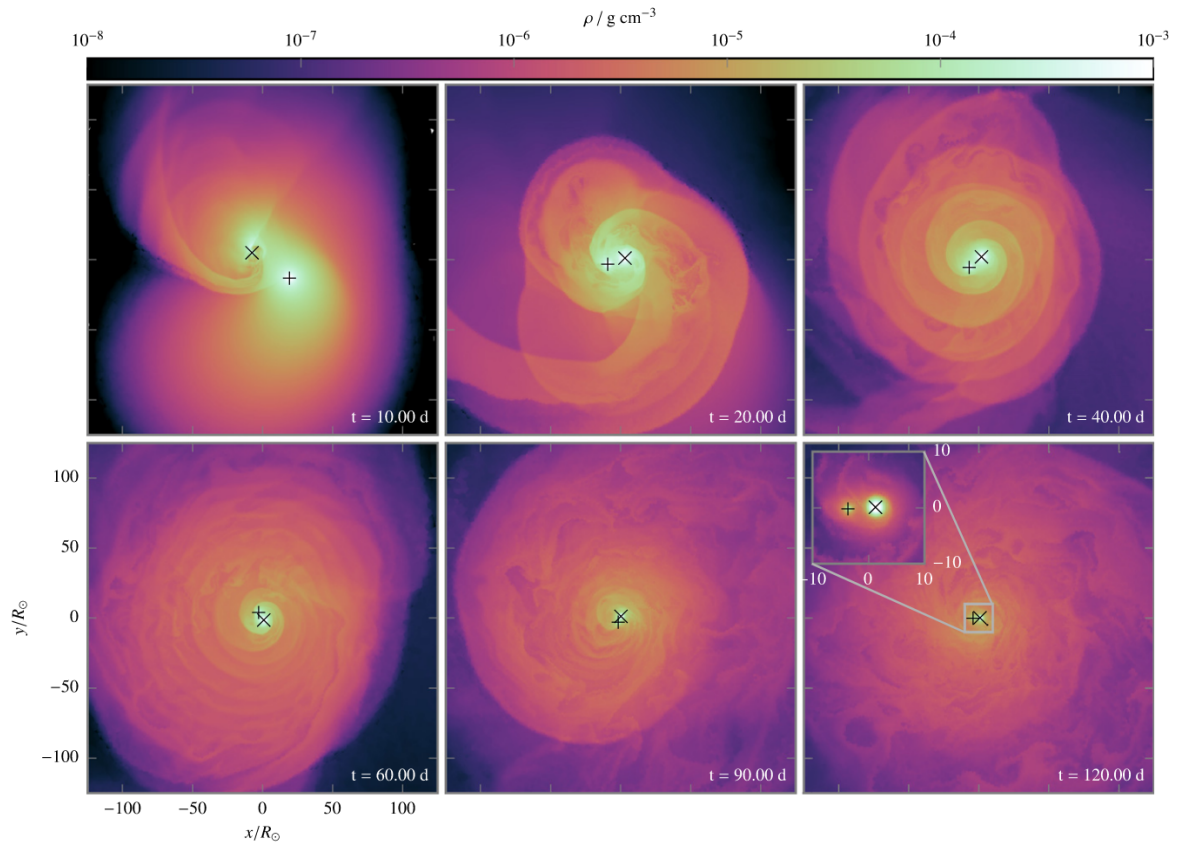


Figure 1.5: Simulation of a common envelope evolution. The “+” sign is the position of the core of the red giant (RG) and the “x” sign is the position of the secondary star. The gas density, which represents the convective envelope of the RG, is shown with the color map. After a period of 110 days, the binary went from a separation of about 25 solar radius to less than 10 solar radius. Figure from Ohlmann et al. (2016).

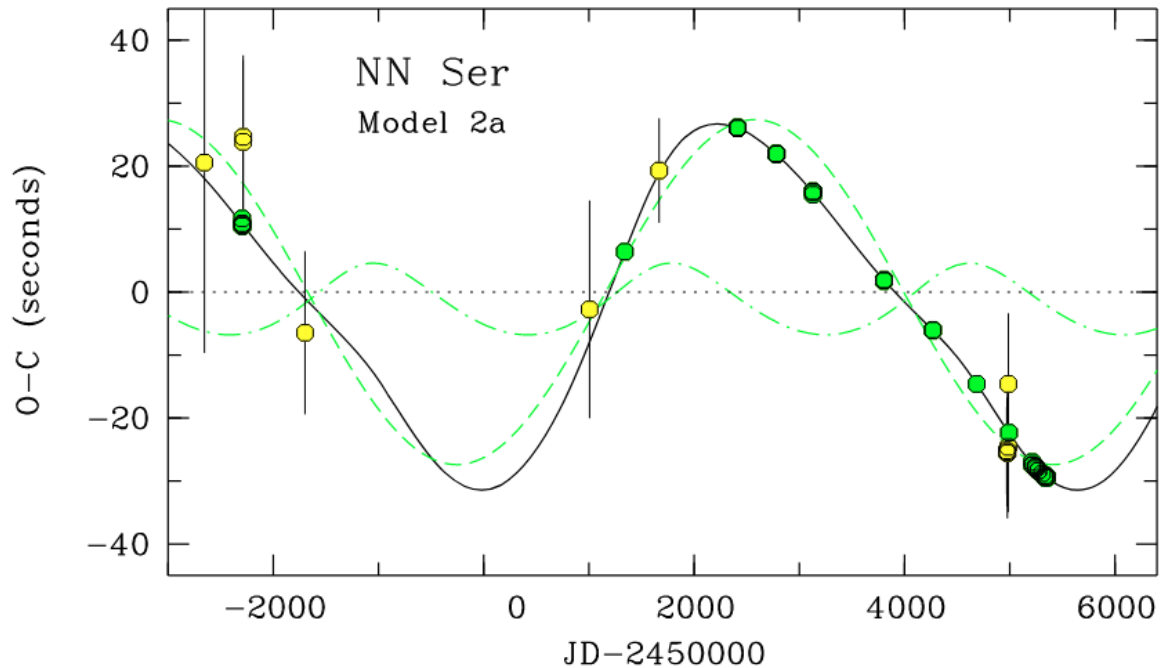


Figure 1.6: Observed-minus-calculated ($O - C$) diagram of the post-common-envelope binary NN Ser. The observations, shown as yellow and green data points, are fitted with the black line. The two green lines are the individual contributions to the model and are interpreted as circumbinary planets. Figure from Beuermann et al. (2010).

physical environments such as extreme mass transfers and mergers. One less explored physics is magnetic fields in close binaries and how it connects to dynamo theory specially because, due to the short binary separation, tidal locking should bring the main-sequence star to extreme rotation rates.

1.2.2 ETVs and the planetary hypothesis

Upon close inspection and after a relatively long observational baseline of the eclipsing times, it has become clear that approximately 90% of observed PCEBs have apparent period variations (Zorotovic and Schreiber 2013). A typical observed-minus-calculated ($O - C$) diagram of the eclipsing times is shown in Fig. 1.6. The $O - C$ diagrams of the eclipsing times are constructed by measuring the time of an eclipse. Then, one assumes that the orbits of the binary is governed by the Kepler laws and that no other bodies are present. The expected time when the eclipses would take place is computed and is subtracted from the observed time. Finally, the result is plotted as a function of

time. If the assumption of no extra physics such as gravitational pull by other bodies is correct, then the data points would lie on $O - C = 0$. Otherwise, the hypothesis is incorrect and a physical process is at place which the calculation did not account for. This is the case in PCEBs and the fact that $\sim 90\%$ of them show this phenomena points at a underlying systematic physical mechanism.

In the case of NN Ser, which is shown in Fig. 1.6, the quasi-periodic variation of the $O - C$ diagram has been interpreted as the gravitational pull from two circumbinary planets (e.g. Marsh et al. 2014). Another example includes V471 Tau, a prototypical PCEB for which the theory of common envelope evolution was developed (Paczynski 1976). A recent study revisited the binary parameters, and revealed that it consists of a main-sequence star of $M = 0.853M_{\odot}$ and $R = 0.816R_{\odot}$, and a white dwarf of $M = 0.792M_{\odot}$ and $R = 0.01134R_{\odot}$, while the binary separation is $a = 3.19R_{\odot}$ (Muirhead, Nordhaus, and Drout 2022). This system has been studied with unique detail. It was first reported by Lohsen (1974) that V471 Tau undergoes period variations. Beavers, Herczeg, and Lui (1986) proposed that a third body could be the responsible for the eclipsing time variations and it was later determined that the parameters of the third body would correspond to a brown dwarf (Guinan and Ribas 2001).

The planetary hypothesis attributes ETVs to circumbinary bodies, such as those above. These planets could have been formed together with the binary or from the common envelope material. These two hypothesis are know as first and second generation formation scenarios, respectively (e.g., Schleicher and Dreizler 2014; Völschow, Banerjee, and Hessman 2014). Regardless of when the planets were formed, they must fulfill the basic requirement of orbital stability over long periods of time. In this regard, it is commonly found in the literature that a proposed set of planets for a given PCEB fail to withstand orbital stability tests or fail to predict upcoming eclipsing times. This was recently summarized by Pulley et al. (2022) who reanalyzed the eclipsing times of seven PCEBs with new data and concluded that in all of them but one (NY Vir), the proposed circumbinary models fail to predict the new eclipsing times.

In the particular case of V471 Tau, the search of the proposed brown dwarf was pursued by Hardy et al. (2015). They attempted to directly image the brown dwarf with the SPHERE instrument which, however, resulted in a non-detection. Independently, Vanderbosch et al. (2017) studied the presence of a brown dwarf in V471 Tau by constructing an $O - C$ diagram of the spin-period of the white dwarf and of the orbital period of the binary. If there was a third body, the authors proposed that the wobbling barycenter would introduce variations of the same order of magnitude in the two $O - C$ diagrams. However, the authors found that the $O - C$ diagram of the spin-period is flat and thus ruled out the existence of a third body in V471 Tau. Overall, the data points to the inadequateness of the planetary hypothesis in this system (Kundra et al. 2022).

1.3 Period Variations from Magnetic Activity

Period variations were first connected to magnetic activity in binary stars by Applegate and Patterson (1987). The gravitational potential outside of the magnetically active star can be written as

$$\phi(r) = -\frac{GM}{r} - \frac{3G}{2} \sum_{i,j} Q_{ij} \frac{x_i x_j}{r^5}, \quad (1.19)$$

where r is the distance from the center of the active star, G is the gravitational constant, M is the mass of the active star, Q_{ij} are the quadrupole moment tensor components, and x_i, x_j are the Cartesian coordinates as measured from the center of the active star. The sum is performed over $i, j = 1, 2, 3$. Explicitly, the quadrupole moment can be computed as

$$Q_{ij} = I_{ij} - \frac{1}{3} \delta_{ij} \text{Tr } I, \quad (1.20)$$

where

$$I_{ij} = \int_V \rho(\mathbf{x}) x_i x_j dV \quad (1.21)$$

is the inertia tensor, $\text{Tr } I$ is the trace of the inertia tensor, δ_{ij} is the Kronecker delta, and ρ is the density at (x_i, x_j, x_k) . By adopting a coordinate system which rotates with the binary and points towards the secondary star, Applegate and Patterson (1987) showed that the period of the binary can be modulated as

$$\frac{\Delta P}{P} = -9 \frac{\Delta Q_{xx}}{Ma^2}. \quad (1.22)$$

Here, $\Delta P/P$ is the change of the orbital period as a fraction of the mean, ΔQ_{xx} is the change in the quadrupole moment, and a is the binary separation. Under the assumption of the coordinate system above, only the xx component of Q_{ij} survives. Equation 1.22 can be directly compared with observations by considering that (Applegate 1992)

$$\frac{\Delta P}{P} = 2\pi \frac{O - C}{P_{\text{mod}}}, \quad (1.23)$$

where $O - C$ is the amplitude of the $O - C$ diagram of the eclipsing times and P_{mod} is the period over which the $O - C$ diagram is modulated. Thus

$$\Delta Q_{xx} = -\frac{2}{9} \pi M a^2 \frac{O - C}{P_{\text{mod}}}. \quad (1.24)$$

All of the quantities of the right hand side of Eq. 1.24 are observable. The required changes of Q_{xx} that produce any observed $O - C$ variations can be estimated from here. However, it is unknown what the values of the quadrupole moment are. This is

because the density distribution of the star is hidden to observations. It can, however, be computed from numerical simulations.

Changes in the density field alter the moments of inertia as seen in Eq. 1.21, which in turn change the quadrupole moment (Eq. 1.20). The gravitational potential will thus change as seen in Eq. 1.19. The orbital period changes according to Eq. 1.22 and can be observed in eclipsing binaries if sufficiently long observations are available. At this point, the attention is shifted to finding a mechanism which can alter the quadrupole moment in such a way that explains observations.

1.3.1 The Applegate mechanism

Rapid rotation and convective envelopes, ingredients necessary for a dynamo, are quite common in post-common envelope binaries. As such, Applegate and Patterson (1987) proposed that a varying magnetic field of mean strength $B_{\text{surf}} = 100$ G could produce the necessary quadrupole moment variations. It was proposed that the quadrupole moment is connected to the magnetic field strength as

$$\Delta Q \sim I_p \frac{M_{\text{CZ}}}{M} \frac{B^2}{8\pi P}, \quad (1.25)$$

where I_p is the moment of inertia of the primary star, M_{CZ} is the mass of the convective region, M is the total mass of the star, and P is the total pressure. The ratio $B^2/8\pi P$ (in cgs units) was estimated to be 10^{-4} in V471 Tau in order to explain observations.

The first mechanism which explains eclipsing time variations through magnetic activity was presented by Applegate (1992). This is now known as the *Applegate mechanism*. We start by considering a thin shell that surrounds the interior of the star, modeled as a point mass at the center of the star. The idea is to find a mechanism which can change the angular momentum of the shell. The approximation is justified by considering that the moment of inertia tensor has a factor of r^2 , with r being the radius of the star. Thus, changes in the outer layers of the star will contribute much more to changes in the quadrupole moment. Because of the rotation Ω of the star, the shell of mass M_s is oblate. The quadrupole moment and moment of inertia of the shell are

$$Q = \frac{1}{9} M_s R^2 \left(\frac{\Omega^2 R^3}{GM} \right), \quad (1.26)$$

$$I = \frac{2}{3} M_s R^2. \quad (1.27)$$

The derivative dQ/dJ , where J is the angular momentum, of the shell, can be estimated as

$$\frac{dQ}{dJ} = \frac{1}{3} \frac{\Omega R^3}{GM}. \quad (1.28)$$

By combining Eqs. 1.22 and 1.28, Applegate (1992) showed that the necessary angular momentum exchange ΔJ to produce a period variation of ΔP is

$$\Delta J = -\frac{GM^2}{R} \left(\frac{a}{R}\right)^2 \frac{\Delta P}{6\pi}. \quad (1.29)$$

The periodic exchange of angular momentum between the core and the thin shell requires a torque N , which is

$$N = \pi \frac{\Delta J}{P_{\text{mod}}}, \quad (1.30)$$

where P_{mod} is the modulation period of the binary period. By assuming that the torque is provided by a magnetic field, the expected field strength is of the order of a few kilo Gauss. Such field strengths are common in stars and thus, the system seems feasible. A key aspect of the Applegate mechanism is that it relies on the centrifugal force of the star. The magnetic field provides the torque that redistributes the angular momentum within the star. As the outer layers carry more angular momentum, they spin-up and due to the centrifugal force they become more oblate.

Since then, the Applegate mechanism has gone through many improvements and tests. For example, Brinkworth et al. (2006) extended the Applegate mechanism to the scenario where the angular momentum is exchanged between the core and a shell which is no longer thin. This leads to an energy exchange between the two

$$\Delta E = (\Omega_s - \Omega_c)\Delta J + \frac{1}{2} \left(\frac{1}{I_s} + \frac{1}{I_c} \right) (\Delta J)^2, \quad (1.31)$$

where Ω_s and Ω_c are the rotation rates of the shell and core, respectively, and I_s and I_c their moments of inertia. The minimum energy that is required to drive these changes was shown to be ten times larger than what is available from the luminosity variations of the magnetically active star in NN Ser (Brinkworth et al. 2006). Völschow et al. (2016) used this formalism, together with more realistic stellar density profiles derived with the *Evolve ZAMS* code instead of density profiles calculated from the Lane-Emden equation as it was done by Brinkworth et al. (2006), and applied it to a set of 16 PCEBs. From energetic grounds, they found that the Applegate mechanism is more feasible for systems with smaller binary separation. In general, however, the energy required to drive the necessary quadrupole moment variations were still larger than the energy provided by the stellar luminosity.

Much more detailed studies exist to date. For example, a more general approach was first introduced by Lanza, Rodono, and Rosner (1998). Here, the effects of the internal magnetic fields were considered. It was found that in this case, the energetic requirements are reduced by a factor of two. The subsequent model of Lanza (2006) aimed at solving the angular momentum equation along the stellar convective zone. Building upon this framework, Völschow et al. (2018) extended the model of Lanza

(2006) by considering time-fluctuating velocity and magnetic fields. The angular momentum transfer equation within the star reads (Lanza 2006; Völschow et al. 2018)

$$\frac{\partial \omega}{\partial t} - \frac{1}{\rho r^4} \frac{\partial}{\partial r} \left(r^4 \eta_t \frac{\partial \omega}{\partial r} \right) - \frac{\eta_t}{\rho r^2} \frac{1}{1 - \mu^2} \frac{\partial}{\partial \mu} \left((1 - \mu^2)^2 \frac{\partial \omega}{\partial \mu} \right) = S(r, \mu, t), \quad (1.32)$$

where ω is the angular momentum, ρ is the mass density, r is the radius, $\eta_t = \eta_t(r)$ is the turbulent dynamical viscosity, and $\mu = \cos \theta$, where θ is the latitudinal angle. S is a source term which controls the transport of momentum via the Reynolds and Maxwell stress tensors. It is computed as (Völschow et al. 2018)

$$S = -\frac{\nabla \cdot \boldsymbol{\tau}}{\rho r^2 (1 - \mu^2)}, \quad (1.33)$$

where

$$\tau_i = r \sin \theta \left(\Lambda_{i\phi} + \frac{1}{\tilde{\mu}} (\overline{B_i B_\phi} + M_{i\phi}) \right). \quad (1.34)$$

Here, $\Lambda_{i\phi} = \overline{\rho v'_i v'_\phi}$ and $M_{i\phi} = \overline{B'_i B'_\phi}$ are the Reynolds and Maxwell stress tensors, respectively, and $\tilde{\mu}$ is the magnetic permeability. The magnetic field is chosen to be purely azimuthal and the velocity purely radial (convective) u_c . Both Λ and M are assumed to fluctuate with over the magnetic cycle of period P_{act} , with amplification coefficients A_v and A_B , and phase $f(t) = \sin(2\pi t/P_{\text{act}})$. Thus,

$$\Lambda_{i\phi} = \Lambda_{i\phi}(r, t) = \rho(r) A_v^2 u_c^2(r) \sin^2(2\pi t/P_{\text{act}}), \quad (1.35)$$

$$M_{i\phi} = M_{i\phi}(r, t) = A_B^2 B_{\text{surf}}^2 \sin^2(2\pi t/P_{\text{act}}), \quad (1.36)$$

where B_{surf} is the magnetic field at the surface.

By adopting moderate values of fluctuation amplitudes, $A_v = A_B$, and $B_{\text{surf}} = 1$ kG, Völschow et al. (2018) showed that the calculated $\Delta P/P$ is always smaller than observations. However, an interesting result was that the calculated period variations peaks at the transition from fully- to partially convective stars (see Fig. 1.7). The amplitude here is about 7×10^{-8} , which is still smaller than observations but expected to produce a significant contribution to the observed values of $\Delta P/P$.

It seems unlikely that the Applegate mechanism is an adequate explanation to ETVs in close binaries. From energetic grounds, it requires more energy than the available energy produced by nuclear reactions. With analytic models becoming more realistic, the energy requirements were relaxed but still too large (Brinkworth et al. 2006; Lanza, Rodono, and Rosner 1998; Völschow et al. 2018). However, this does not mean that the physics of the Applegate mechanism is flawed. On the contrary, it is very likely that it is working, but with just a smaller observable impact than what was initially thought. Careful monitoring of the period variations and re-analysis of the currently available O – C diagrams will help disentangle the third bodies from magnetic-activity induced perturbations.

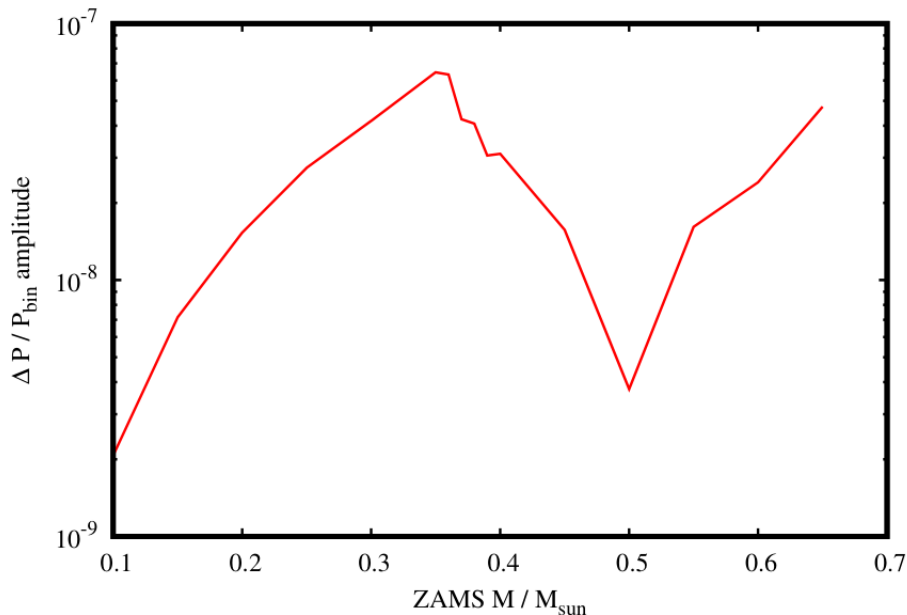


Figure 1.7: Expected period variations as a function of zero-age-main-sequence (ZAMS) mass. Figure from Völschow et al. (2018).

1.3.2 Lanza mechanism

An underlying assumption of the Applegate mechanism is the presence of a purely axisymmetric magnetic field. This forces the quadrupole moment perturbations to be axisymmetric. From a point of view of the binary, the assumption of non-tidally locked or tidally locked is irrelevant. This physical picture changes when the magnetic field is allowed to have modes different from $m = 0$.

Applegate (1989) had already considered this scenario. However, the period variations that he had in mind were of the order of a few years at most. Lanza (2020) extended the model and applied it to the modulation periods of eclipsing times in PCEBs, which are of the order of tens of years.

Consider a flux tube fixed in space and time inside the convective region of a star. The equation for the density perturbations inside (i) and outside (e) the flux tube can be written as

$$\frac{\partial p_{i,e}(r, \sigma)}{\partial r} = -\frac{GM(r)}{r^2} \rho_{i,e}, \quad (1.37)$$

where $p_{i,e}$ is the plasma pressure inside and outside the flux tube, $M(r)$ is the mass contained inside a radius r , and $\rho_{i,e}$ is the density inside and outside the flux tube. Furthermore, σ is the distance from the axis of symmetry of the flux tube to a point at constant radius. Figure 1.8 shows an illustration of the system under consideration.

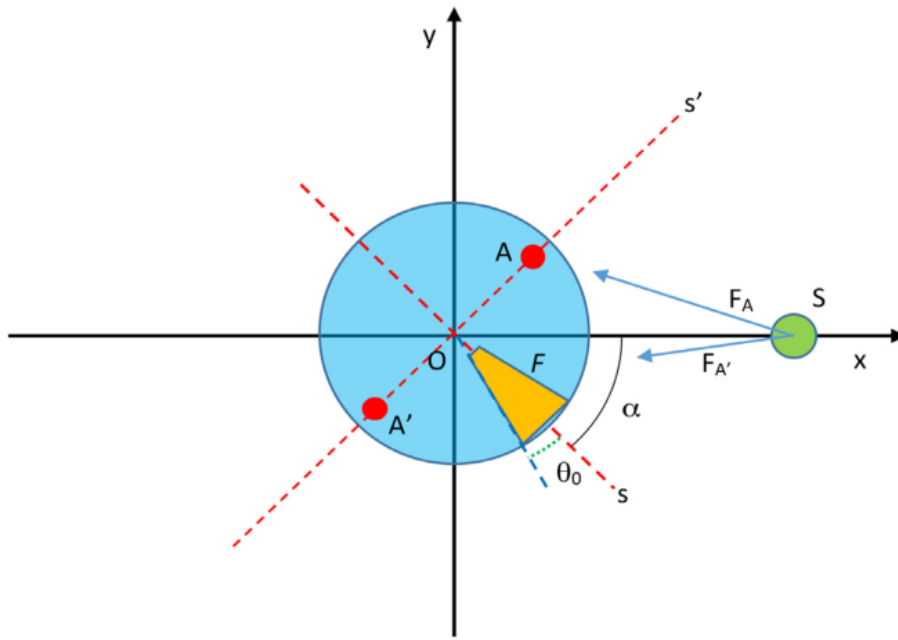


Figure 1.8: Illustration of the configuration considered by Lanza (2020). The plane xy lies on the plane of the binary, as well as ss' . The axis x points towards the companion star, shown in green, and s coincides with the axis of symmetry of the flux tube, shown in yellow with angular radius of θ_0 . The angle α is the angular separation between x and s . The effects of the flux tube can be modeled as two point masses A and A' which produce the forces F and $F_{A'}$, respectively, on the companion. Figure from Lanza (2020).

In this configuration, where there is a non-axisymmetric magnetic field which produces a non-axisymmetric quadrupole moment and without tidal locking, the gravitational potential can be written as

$$\phi = -\frac{GM}{r} - \frac{3G}{2r^3} (\delta Q_{xx} \sin^2 \theta \cos^2 \alpha + \delta Q_{yy} \sin^2 \theta \sin^2 \alpha + \delta Q_{zz} \cos^2 \theta), \quad (1.38)$$

where

$$\delta Q_{xx} = \delta Q + \frac{T}{2}, \quad (1.39)$$

$$\delta Q_{yy} = \delta Q - \frac{T}{2}, \quad (1.40)$$

$$\delta Q_{zz} = -2\delta Q, \quad (1.41)$$

$$T = \delta Q_{xx} - \delta Q_{yy}. \quad (1.42)$$

The deltas represent perturbations due to the presence of the flux tube, while θ is colatitude. The equation of motion of the binary is governed by the oscillation of the angle α , which can be written as

$$\frac{d^2\alpha}{dt^2} + \frac{1}{2}\omega_P^2 \sin 2\alpha = 0, \quad (1.43)$$

where

$$\omega_P^2 = 3\frac{Gm_S T}{r^3} \left(\frac{1}{mr^2} + \frac{1}{I_p} \right) \quad (1.44)$$

is the amplitude of the oscillation, m_S is the mass of the secondary star, m is the reduced mass of the binary, and I_p is the moment of inertia of the magnetically active star about the spin axis.

Two solutions to Eq. 1.43 were identified by Applegate (1989) and Lanza (2020). In particular, Lanza (2020) found solutions by looking at the first integral of Eq. 1.43, i.e.

$$\frac{1}{2} \frac{d\alpha^2}{dt} + \frac{1}{2}\omega_P^2 \sin^2 \alpha = \frac{1}{2}E^2, \quad (1.45)$$

where E is the integration constant which is a constant of motion that depends on the initial conditions. For $E \leq \omega_P$, the solution is a *libration* of α . That is, a pendulum-like oscillation with amplitude $\alpha_0 = \arcsin(E/\omega_P)$. If $E > \omega_P$, then α varies monotonically because it has enough energy to go over the maxima, solution which is referred as *circulation*.

Lanza (2020) applied this model to three close binaries: HR 1099, V471 Tau, and NN Ser. The solutions were found by finding the best parameters that would fit the observations. In the first case, the libration model was favored over the circulation as

the latter is not able to reproduce the observations. In V471 Tau, it was found the two models reproduce observations. The energy requirements are $10^2 - 10^3$ times smaller than in the previous models such as in Applegate (1992). Lastly, in NN Ser, the low luminosity of the active star does not appear to be high enough to power the models, and so the presence of planets that change the eclipsing times is favored.

Overall, this newer mechanism is much more energetically feasible than the previous models. The requirement of asynchronous stellar spin and binary period will need to be tested. For example, Lurie et al. (2017) identified 21 asynchronous eclipsing binaries with orbital periods less than 10 days. The authors attributed this asynchronization to either them being too young or having a complex dynamical history. The latter explanation would certainly fit post common envelope binaries because their formation history involves a complex common envelope interaction (Paczynski 1976). Thus, it seems at least plausible that PCEBs are not tidally locked, but a careful determination of it is still pending.

Chapter 2

Aims and methods

The Applegate mechanism have only been studied in detail with analytic tools. The value of the quadrupole moment has usually been worked out by taking the core-to-shell transition at position of the star where the energy required to drive the Applegate mechanism is minimized (Brinkworth et al. 2006; Völschow et al. 2016). In the studies of Lanza (2006) and Völschow et al. (2018), the period variations of the binaries were computed from a model where the magnetic and velocity fields and fluctuations were constant in the former and time-dependent in the latter. While more general, these models rely on adopting a certain value of the fields and their respective fluctuations.

This thesis is concerned on finding the gravitational quadrupole moment from a more self-consistent magnetohydrodynamical model. With Q_{ij} at hand, the goal is to look for the mechanism that gives rise to it and whether it is large enough to reproduce the observed eclipsing time variations in post-common-envelope binaries.

2.1 Gravitational quadrupole moment from dynamo simulations

Stellar dynamo models are already mature enough to start being used to tackle astrophysical questions other than the ones related to dynamos per se.

The gravitational quadrupole moment arises from an asymmetric distribution of density. The anelastic and Boussinesq approximations do not take the density fluctuations or only consider these as very small. These fluctuations can only be captured with the fully compressible (magneto) hydrodynamical equations. It is for this reason that this thesis focuses on solving these equations in particular. However, in the real scenario of a very rapidly rotating star with rotation rate more than fifty times the rotation of the Sun, one would expect a star that deviates from perfect spherical symmetry. On top of this, a sufficiently strong magnetic field in the surface layer would produce

an asymmetric density distribution with the possibility of inflating and deflating the star if the magnetic field is cyclic as those found in dynamo simulations. To capture such effects self-consistently, we would need a numerical model of a stellar dynamo with flexible boundary conditions that allow for stellar deformations, thus producing a time dependent ellipsoidal star. However, such models do not exist to date. The reason for this is that efforts to model stellar dynamo have focused on situations where these deformations are small such as in the Sun.

Still, it is possible to capture variations of Q from spherically symmetric stars. This was done by Navarrete et al. (2020) where it was shown that Q closely follows the magnetic cycles. This approach gives a good estimate of the expected variations of Q in a real physical star under the assumption of negligible variations of the shape and size of the secondary.

2.2 Numerical Setup

From a numerical perspective, it is extremely challenging to self-consistently model the Applegate or Lanza-Applegate mechanisms. One would need to model the physics of the interior of the secondary star, and also the dynamics of the binary. A way to overcome this is to model just the physics of the convective region of the secondary, which is where stellar dynamos take place. One can measure the changes in the quadrupole moment and attempt to find their origin, and use analytic results to estimate the eclipsing time variations. The numerical model used in this thesis is explained here.

Consider the convective region of a solar-like star without the polar caps. The computational domain is $0.7R \leq r \leq R$, $\theta_0 \leq \theta \leq \pi - \theta_0$, and $0 \leq \phi < 2\pi$, where (r, θ, ϕ) are the usual spherical coordinates, and $\theta_0 = \pi/12$. The equation of compressible magnetohydrodynamics are solved in this domain. These are

$$\frac{\partial \mathbf{A}}{\partial t} = \mathbf{u} \times \mathbf{B} - \eta \mu_0 \mathbf{J}, \quad (2.1)$$

$$\frac{D \ln \rho}{Dt} = -\nabla \cdot \mathbf{u}, \quad (2.2)$$

$$\frac{D \mathbf{u}}{Dt} = \mathcal{F}^{\text{grav}} + \mathcal{F}^{\text{Cor}} + \mathcal{F}^{\text{cent}} - \frac{1}{\rho} (\nabla p - \mathbf{J} \times \mathbf{B} - \nabla \cdot 2\nu \rho \mathbf{S}), \quad (2.3)$$

$$T \frac{Ds}{Dt} = \frac{1}{\rho} [\eta \mu_0 \mathbf{J}^2 - \nabla \cdot (\mathbf{F}^{\text{rad}} + \mathbf{F}^{\text{SGS}})] + 2\nu \mathbf{S}^2, \quad (2.4)$$

where $\mathbf{B} = \nabla \times \mathbf{A}$ is the magnetic field and \mathbf{A} is the magnetic vector potential, \mathbf{u} is the velocity field, η is the magnetic diffusivity, μ_0 is the vacuum permeability, $\mathbf{J} = \nabla \times \mathbf{B} / \mu_0$ is the electric current density, ρ is the mass density, p is the pressure,

ν is the viscosity, T is the temperature, and s is the specific entropy. Furthermore,

$$S_{ij} = \frac{1}{2}(u_{i;j} + u_{j;i}) - \frac{1}{3}\delta_{ij}\nabla \cdot \mathbf{u} \quad (2.5)$$

is the rate-of-strain tensor and where semi-colons denote covariant differentiation. The above system of equations is closed by an equation of state which here is assumed as ideal, i.e.

$$p = (\gamma - 1)\rho e, \quad (2.6)$$

where $\gamma = 5/3$ and e is the specific internal energy.

Two fluxes can be identified in the energy equation 2.4. These are the radiative flux

$$\mathbf{F}^{\text{rad}} = -K\nabla T, \quad (2.7)$$

which models transport of heat by radiation with K being the radiative heat conductivity, and the sub-grid scale (SGS) flux

$$\mathbf{F}^{\text{SGS}} = -\chi_{\text{SGS}}\rho T\nabla s, \quad (2.8)$$

which models the unresolved heat transport by turbulence and where χ_{SGS} is the turbulent entropy diffusivity.

Three forces appear in Eq. 2.3,

$$\mathcal{F}^{\text{grav}} = -\frac{GM}{r^2}\hat{\mathbf{r}}, \quad (2.9)$$

$$\mathcal{F}^{\text{Cor}} = -2\boldsymbol{\Omega}_0 \times \mathbf{u}, \quad (2.10)$$

$$\mathcal{F}^{\text{cent}} = -c_f\boldsymbol{\Omega}_0 \times (\boldsymbol{\Omega}_0 \times \mathbf{u}), \quad (2.11)$$

which are the gravitational, Coriolis, and centrifugal terms, respectively. Here, G is the gravitational constant and $\boldsymbol{\Omega}_0 = \Omega_0(\cos\theta, -\sin\theta, 0)$ is the rotation vector of the star. The factor c_f that appear in the centrifugal term is added as a control parameter, which we keep equal to zero in Paper I and vary it in Papers II and III. It is needed in simulations that enhance the luminosity, as otherwise $\mathcal{F}^{\text{cent}}$ would be too large and blow up the star (see below).

2.2.1 Initial conditions

For the initial conditions, we choose an isentropic state. The density stratification follows from hydrostatic equilibrium. Velocity and magnetic fields are initialized with low-amplitude, Gaussian white noise. As such, these two fields peak at the grid scale and the magnetic field quickly decay due to dissipative effects. For an evolution of volumetric quantities such as root-mean-squared velocity and magnetic fields, see Sect. 2.2.3.

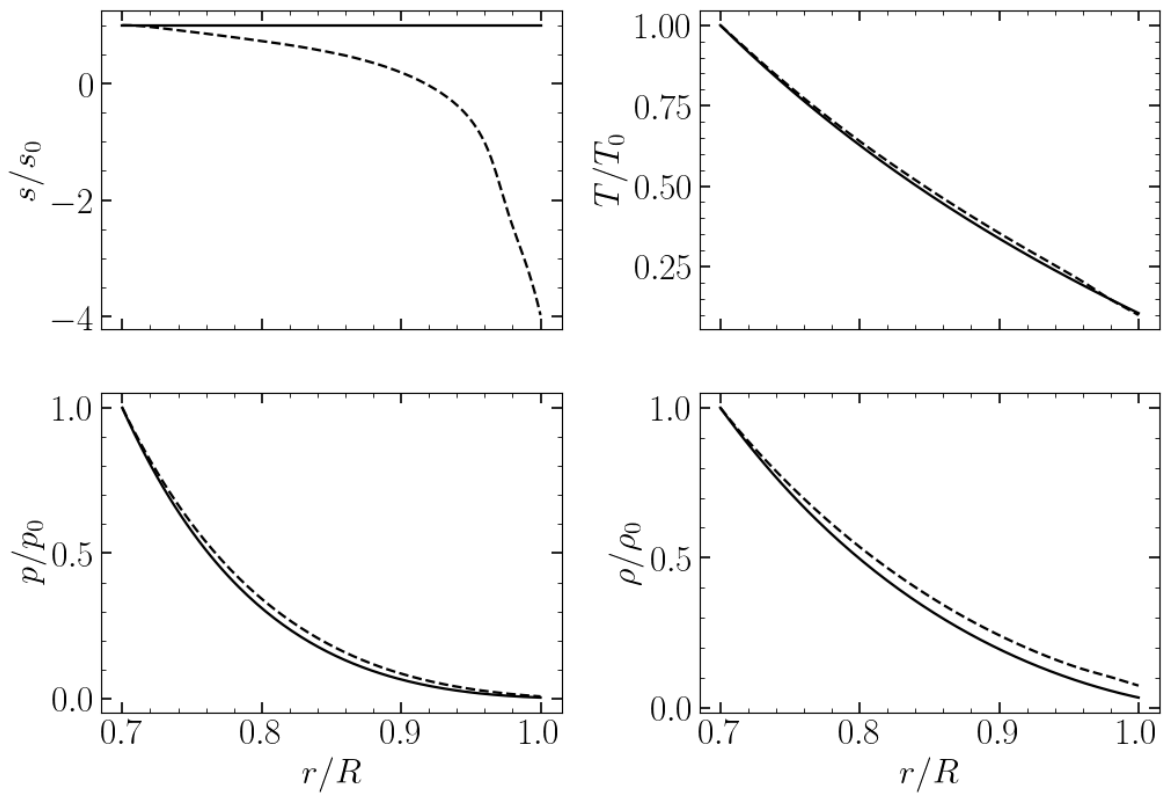


Figure 2.1: Initial (solid lines) and final (dashed lines) radial profiles of entropy (upper left), temperature (upper right), pressure (bottom left) and density (bottom right), of a typical run of the spherical wedge setup. All quantities have been normalized by the value at the bottom of the domain.

Figure 2.1 shows the initial and final radial profiles of thermodynamical quantities in a typical run.

The simulations are characterized by several input parameters. These are the Coriolis, Taylor, Reynolds, magnetic Reynolds, Prandtl, magnetic Prandtl, SGS Prandtl, and Péclet number, which are defined as

$$\text{Co} = \frac{2\Omega_0}{u_{\text{rms}}k_1}, \quad \text{Ta} = \left[\frac{2\Omega_0(0.3R)^2}{\nu} \right]^2, \quad \text{Re} = \frac{u_{\text{rms}}}{\nu k_1}, \quad (2.12)$$

$$\text{Re}_M = \frac{u_{\text{rms}}}{\eta k_1}, \quad \text{Pr} = \frac{\nu}{\chi_m}, \quad \text{Pr}_M = \frac{\nu}{\eta}, \quad \text{Pr}_{\text{SGS}} = \frac{\nu}{\chi_{\text{SGS}}^m}, \quad (2.13)$$

$$\text{Pe} = \frac{u_{\text{rms}}}{\chi_{\text{SGS}}^m k_1}, \quad (2.14)$$

where u_{rms} is the rms velocity, $k_1 = 2\pi/0.3R$ is an estimate of the wavenumber of the largest eddies, and $\chi_{\text{SGS}}^m = 0.4\nu$ is the subgrid scale entropy diffusion in the middle of the convective region.

2.2.2 Boundary conditions

Boundary conditions for \mathbf{u} , \mathbf{A} , $\ln \rho$, and s have to be chosen for the radial and latitudinal boundaries, but as the model considers the full azimuthal extent, the boundary conditions there are periodic.

The radial velocity is anti-symmetric at the radial boundaries (vanishing u_r) and is symmetric at the latitudinal boundaries (vanishing first derivative). At the latitudinal boundary, the first derivative of u_θ is also set to vanish. All of the other boundary conditions for the velocity field are chosen as stress-free. For the magnetic field, we set the boundary at the bottom as a perfect conductor. The same applies to the latitudinal boundaries, and the magnetic field at the surface is chosen as radial. Both the density and entropy are chosen to have vanishing first derivative and so there are no outflows and no heat flux through these boundaries.

2.2.3 Temporal evolution

The temporal evolution of some quantities of interest is shown in Fig. 2.2. The velocity quickly reaches a saturated regime after about 3 years of simulated time. The magnetic field is quickly dissipated as mentioned earlier, but after a quick exponential growth it reaches a saturated regime after 10 years. The thermal energy takes about 15 years to saturate. This is a typical characteristic of stellar convection simulations, namely, convection is slow at transporting heat. This is the reason why we use the enhanced luminosity method. When compared to the Sun, our input luminosity is about six

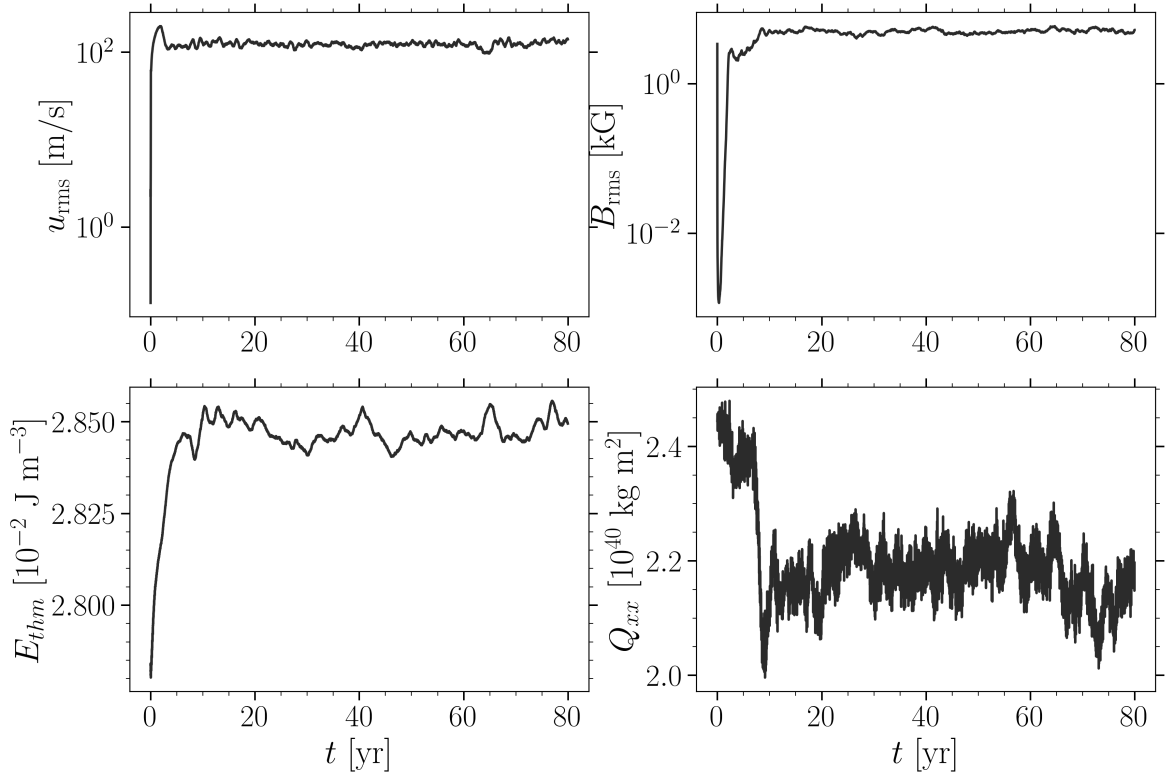


Figure 2.2: Temporal evolution of the rms velocity (top left), rms magnetic field (top right), thermal energy (bottom left), and gravitational quadrupole moment (bottom right). Each one is characterized by its own growth timescale and steady state.

orders of magnitude larger. This makes the Kelvin-Helmholtz time scale, which quantifies the time it takes to reach thermal saturation, corresponding to a factor of 10^6 times shorter.

The xx component of the gravitational quadrupole moment, a key quantity of interest in this thesis, is shown in the lower right panel of Fig. 2.2. It reaches a steady state plus some fluctuations on top at 15 years, which is the same time it takes to reach thermal saturation. The effects that the enhanced luminosity method has on Q_{xx} are discussed in Paper I.

The temporal evolution of some quantities follow a much longer timescale. For example, in one run we find that the axisymmetric magnetic field evolves over a timescale of 80 – 100 years. In general, we need to run until we see at least one cycle of Q_{xx} , which closely follows the cycles we see in the magnetic energy (see Paper I and II).





Chapter 3

Paper I

Contribution

In the following paper, the three simulations were run by me at the HLRN cluster in Germany. To do so, I wrote a computing proposal and planned the simulations. All of the data analysis was performed by me as well as the preparation of the manuscript.

Origin of eclipsing time variations: Contributions of different modes of the dynamo-generated magnetic field

Felipe H. Navarrete^{1,2} , Petri J. Käpylä^{3,2} , Dominik R. G. Schleicher⁴ , Carolina A. Ortiz⁴ , and Robi Banerjee¹

¹ Hamburger Sternwarte, Universität Hamburg, Gojenbergsweg 112, 21029 Hamburg, Germany
e-mail: felipe.navarrete@hs.uni-hamburg.de

² Nordita, Stockholm University and KTH Royal Institute of Technology, Hannes Alfvéns väg 12, 106 91 Stockholm, Sweden

³ Institut für Astrophysik, Georg-August-Universität Göttingen, Friedrich-Hund-Platz 1, 37077 Göttingen, Germany

⁴ Departamento de Astronomía, Facultad de Ciencias Físicas y Matemáticas, Universidad de Concepción, Av. Esteban Iturra s/n Barrio Universitario, Casilla 160-C, Chile

Received 2 February 2022 / Accepted 22 May 2022

ABSTRACT

Context. The possibility to detect circumbinary planets and to study stellar magnetic fields through eclipsing time variations (ETVs) in binary stars has sparked an increase of interest in this area of research.

Aims. We revisit the connection between stellar magnetic fields and the gravitational quadrupole moment Q_{xx} and compare different dynamo-generated ETV models with our simulations.

Methods. We present magnetohydrodynamical simulations of solar mass stars with rotation periods of 8.3, 1.2, and 0.8 days and perform a detailed analysis of the magnetic and quadrupole moment using spherical harmonic decomposition.

Results. The extrema of Q_{xx} are associated with changes in the magnetic field structure. This is evident in the simulation with a rotation period of 1.2 days. Its magnetic field has a more complex behavior than in the other models, as the large-scale nonaxisymmetric field dominates throughout the simulation and the axisymmetric component is predominantly hemispheric. This triggers variations in the density field that follow the magnetic field asymmetry with respect to the equator, affecting the zz component of the inertia tensor, and thus modulating Q_{xx} . The magnetic fields of the two other runs are less variable in time and more symmetric with respect to the equator, such that the variations in the density are weaker, and therefore only small variations in Q_{xx} are seen.

Conclusions. If interpreted via the classical Applegate mechanism (tidal locking), the quadrupole moment variations obtained in the current simulations are about two orders of magnitude below those deduced from observations of post-common-envelope binaries. However, if no tidal locking is assumed, our results are compatible with the observed ETVs.

Key words. magnetohydrodynamics (MHD) – dynamo – convection – turbulence – stars: activity – binaries: eclipsing

1. Introduction

Post-common-envelope binaries (PCEBs) are commonly composed of a white dwarf and a low-mass main-sequence star. Observations of eclipses in these systems reveal deviations from the calculated eclipsing times in approximately 90% of these systems (Zorotovic & Schreiber 2013), with binary period variations on the order of 10^{-6} – 10^{-7} modulated over periods on the order of decades.

The two main explanations, although not mutually exclusive, are the planetary hypothesis (Brinkworth et al. 2006; Völschow et al. 2014) and the Applegate mechanism (Applegate 1992; Lanza et al. 1998; Völschow et al. 2018; Lanza 2020). In the planetary hypothesis, sufficiently massive planets can force the barycenter of the binary to change its location as they orbit, which would then explain the observed-minus-calculated (O–C) diagram of the eclipsing times. On the other hand, the Applegate mechanism explains the variations via the connection between stellar magnetic fields and the gravitational quadrupole moment Q . The idea behind this mechanism is that when Q increases, the gravitational field also increases. For this to happen, there must be a redistribution of angular momentum within the star. When angular momentum is carried to the outer parts of the convective zone (CZ), these layers rotate faster and, overall, the

star becomes more oblate, which is reflected by an increase in the gravitational quadrupole moment. As there is no angular momentum exchange between the orbit and the star, the orbital velocity increases and the radius decreases in order to maintain the angular momentum of the binary. Thus, the orbital period shortens. In order for this mechanism to work, Applegate (1992) invoked the presence of a cyclic subsurface magnetic field on the order of 10 kG which is responsible for redistributing the internal angular momentum of the star.

Confirming the planetary hypothesis requires a detection of the proposed circumbinary bodies in PCEBs either by directly imaging them, as attempted by Hardy et al. (2015), or via indirect methods such as those employed by Vanderbosch et al. (2017). However, these studies did not detect the proposed third body, a brown dwarf, in V471 Tau, which is a PCEB with a Sun-like main-sequence star and a white dwarf. It was the system Paczynski (1976) used to develop the theory of PCEB formation. Direct modeling of the Applegate mechanism is challenging, and targeted numerical simulations that may help to understand observations have been lacking. Navarrete et al. (2020) presented the first self-consistent 3D magnetohydrodynamical (MHD) simulations of stellar magneto-convection addressing this problem. In that study, the time evolution of the gravitational quadrupole moment and its correlation with the stellar

magnetic field and rotation was studied using two simulations of a solar mass star with three and twenty times solar rotation, corresponding to rotation periods of 8.3 and 1.2 days. However, the centrifugal force, a key ingredient in the original Applegate mechanism, was not included in these simulations. Nevertheless, there were still significant temporal variations of Q due to the response of the stellar structure to the dynamo-generated magnetic field. Such variations were absent in hydrodynamical simulations, confirming their magnetic origin.

Recently, [Lanza \(2020\)](#) presented an alternative to the Applegate mechanism by extending the earlier work of [Applegate \(1989\)](#). He assumed the presence of a persistent nonaxisymmetric magnetic field inside the CZ of the main-sequence star that was modeled as a single flux tube lying at the equatorial plane. The density is lower within the magnetic region in comparison to the rest of the CZ, and the effects of the magnetic field were modeled as two point masses lying on a line perpendicular to the axis of the flux tube at the equator. By further assuming that the star is not tidally locked with the primary, this nonaxisymmetric contribution to the quadrupole moment exerts an additional force onto the companion. [Applegate \(1989\)](#) and [Lanza \(2020\)](#) identified two possible scenarios: the libration model, where the orientation of the flux tube oscillates around a fixed position, and the circulation model, where the axis of the flux tube changes in a monotonic way. These models reduce the energetic requirements by a factor of 10^2 to 10^3 in comparison to the Applegate mechanism, which is much more restrictive from an energetic point of view (see e.g., [Brinkworth et al. 2006](#); [Völschow et al. 2016, 2018](#); [Navarrete et al. 2018](#)). Previous models generally require luminosity variations on the order of 10%, whereas the improved model of [Lanza \(2020\)](#) reduces the energy requirement by a factor of 10^2 – 10^3 .

The transition to predominantly nonaxisymmetric large-scale magnetic fields in solar-like stars for rapid rotation was investigated by [Viviani et al. \(2018\)](#) with the same model as that used by [Navarrete et al. \(2020\)](#). They found that the dominant dynamo mode switches from axi- to nonaxisymmetric at roughly three times the solar rotation rate. However, this study also showed that the dominant dynamo mode depends on the resolution of the simulations such that rapidly rotating models at modest resolutions were again more axisymmetric. In the present study we revisit both simulations presented in [Navarrete et al. \(2020\)](#) with a more detailed analysis and include an additional run to explore the importance of (non-) axisymmetric magnetic fields in the modulation of the gravitational quadrupole moment. The main goal of this study is to investigate whether dynamo-generated quadrupole moment variations can lead to the observed period variations and to compare the classical Applegate mechanism with the one of [Lanza \(2020\)](#) by means of our simulations. The dynamo solution is particularly sensitive to the rotation rate, which is the parameter we focus on in the present study.

In Sect. 2 we present the model and the methods that we use. The results are presented in Sect. 3 and a more in-depth discussion follows in Sect. 4. The conclusions are drawn in Sect. 5.

2. The model

The model employed here is the same as that described in [Käpylä et al. \(2013\)](#) and [Navarrete et al. \(2020\)](#). We solve the compressible MHD equations in a spherical shell configuration resembling the solar convection zone with the PENCIL CODE¹

¹ <https://github.com/pencil-code>

([Pencil Code Collaboration 2021](#)). The equations are

$$\frac{\partial \mathbf{A}}{\partial t} = \mathbf{u} \times \mathbf{B} - \mu_0 \eta \mathbf{J}, \quad (1)$$

$$\frac{D \ln \rho}{Dt} = -\nabla \cdot \mathbf{u}, \quad (2)$$

$$\frac{D \mathbf{u}}{Dt} = \mathbf{g} - 2\boldsymbol{\Omega}_0 \times \mathbf{u} + \frac{1}{\rho} (\mathbf{J} \times \mathbf{B} - \nabla p + \nabla \cdot 2\nu \rho \mathbf{S}), \quad (3)$$

$$T \frac{Ds}{Dt} = \frac{1}{\rho} [-\nabla \cdot (\mathbf{F}^{\text{rad}} + \mathbf{F}^{\text{SGS}}) + \mu_0 \eta \mathbf{J}^2] + 2\nu \mathbf{S}^2, \quad (4)$$

where \mathbf{A} is the magnetic vector potential, \mathbf{u} is the velocity field, $\mathbf{B} = \nabla \times \mathbf{A}$ is the magnetic field, and $\mathbf{J} = \mu_0^{-1} \nabla \times \mathbf{B}$ is the electric current density where μ_0 is the vacuum permeability. Also, $D/Dt = \partial/\partial t + \mathbf{u} \cdot \nabla$ is the convective derivative, and ρ is the density. $\mathbf{F}^{\text{rad}} = -K \nabla T$ is the radiative flux and $\mathbf{F}^{\text{SGS}} = -\chi_{\text{SGS}} \rho T \nabla s$ is the subgrid-scale (SGS) flux. The former accounts for the flux coming from the radiative core to the CZ whereas the latter represents the unresolved turbulent transport of heat. K is the radiative heat conductivity and χ_{SGS} is the turbulent entropy diffusivity. s is the specific entropy, p is the pressure, and T the temperature. We assume an ideal gas law, that is,

$$p = (\gamma - 1)\rho e, \quad (5)$$

where $\gamma = c_p/c_v = 5/3$ is the ratio of specific heats at constant pressure and volume, and $e = c_v T$ is the specific internal energy. The traceless rate-of-strain tensor, \mathbf{S} , is defined as

$$\mathbf{S}_{ij} = \frac{1}{2}(u_{i;j} + u_{j;i}) - \frac{1}{3}\delta_{ij} \nabla \cdot \mathbf{u}, \quad (6)$$

where semicolons denote covariant differentiation. $\mathbf{g} \propto \hat{\mathbf{r}}/r^2$ is the gravitational acceleration. The rotation vector is given by $\boldsymbol{\Omega}_0 = (\cos \theta, -\sin \theta, 0)\Omega_0$.

2.1. Initial and boundary conditions

The thermodynamic initial state is isentropic. The density profile follows from hydrostatic equilibrium. The simulations are characterized by a number of input parameters. These are the energy flux at the bottom, the angular velocity, viscosity, magnetic diffusivity, and the radiative and turbulent heat conductivities and the radial profiles of the latter two. We keep all of them fixed except for the angular velocity (see Sect. 2.3). Velocity and magnetic fields are initialized with small-scale low-amplitude Gaussian noise perturbations. These have amplitudes of 0.25 m s^{-1} and 4 G, respectively.

The computational domain is given by $0.7R \leq r \leq R$, $\theta_0 \leq \theta \leq \pi - \theta_0$, $0 \leq \phi \leq 2\pi$, for the radial, latitudinal, and longitudinal coordinates, respectively, with $\theta_0 = \pi/12$. Both radial boundaries are impenetrable and stress-free for the flow. The bottom boundary is a perfect conductor and the magnetic field at the surface is radial. The upper boundary follows a blackbody condition. The latitudinal boundaries are stress-free and perfect conductors. The derivatives of the density and entropy are zero on both latitudinal boundaries. This implies that there is no heat flux through these surfaces.

The modeled star is assumed to have one solar mass with a convective envelope covering 30% of the stellar radius. The simulations labeled as Run A and Run B are run3x and run20x presented in [Navarrete et al. \(2020\)](#). The main difference is that a significantly longer (over 160 instead of 85 years) time series is available for Run B. Furthermore, we perform a more in-depth analysis of both simulations and include a third simulation,

labeled as Run C, to ascertain the significance of the non-axisymmetric magnetic fields for the gravitational quadrupole moment (see Sect. 3). Runs A and B have a resolution of $128 \times 256 \times 512$ in the radial, latitudinal, and azimuthal directions respectively, and Run C has a resolution of $128 \times 288 \times 512$.

2.2. Spherical harmonic decomposition

To investigate the proposed connection between the nonaxisymmetric component of the magnetic field and the fluid density, we perform the same decomposition as in Viviani et al. (2018) for the radial magnetic field and density field at various radial depths (see Figs. B.1–B.4 for snapshots of the first and second nonaxisymmetric modes near the surface of the three runs). A function $f = f(\theta, \phi)$ can be written as

$$f(\theta, \phi) = \sum_{l=0}^{l_{\max}} \sum_{m=-l}^l \tilde{f}_l^m(\theta, \phi) Y_l^m(\theta, \phi), \quad (7)$$

where

$$\tilde{f}_l^m = \int_0^{2\pi} \int_{\theta_0}^{\pi-\theta_0} f(\theta, \phi) Y_l^{m*} \sin \theta \, d\theta \, d\phi. \quad (8)$$

For the radial magnetic field $B_r(\theta, \phi)$, we impose the condition (see Krause & Rädler 1980)

$$B_{r,l}^{-m} = (-1)^m B_{r,l}^{m*}, \quad (9)$$

and because the same property applies to the spherical harmonics Y_l^m , we have

$$B_r(\theta, \phi) = \sum_{l=1}^{l_{\max}} B_{l,r}^0 Y_l^0 + 2 \operatorname{Re} \left(\sum_{l=1}^{l_{\max}} \sum_{m=1}^l B_{l,r}^m Y_l^m \right). \quad (10)$$

The term containing $l = 0$ has been dropped because it violates solenoidality of the magnetic field.

2.3. Simulation parameters

Each run is characterized by the Taylor, Coriolis, fluid and magnetic Reynolds numbers, and fluid, SGS and magnetic Prandtl numbers. These are defined as

$$\operatorname{Ta} = \left[\frac{2\Omega_0(0.3R)^2}{\nu} \right]^2, \quad \operatorname{Co} = \frac{2\Omega_0}{u_{\text{rms}} k_1}, \quad (11)$$

$$\operatorname{Co}^{(\omega)} = \frac{2\Omega_0}{\omega_{\text{rms}}}, \quad \operatorname{Re} = \frac{u_{\text{rms}}}{\nu k_1}, \quad \operatorname{Re}_M = \frac{u_{\text{rms}}}{\eta k_1}, \quad (12)$$

$$\operatorname{Pr} = \frac{\nu}{\chi_m}, \quad \operatorname{Pr}_M = \frac{\nu}{\eta}, \quad \operatorname{Pr}_{\text{SGS}} = \frac{\nu}{\chi_{\text{SGS}}^m}, \quad (13)$$

where ν is the viscosity, u_{rms} the root-mean-square velocity, $\operatorname{Co}^{(\omega)}$ is an alternative definition of the Coriolis number based on the rms vorticity, $k_1 = 2\pi/0.3R$ an estimate of the wavenumber of the largest convective eddies, η the magnetic diffusivity, and χ_{SGS}^m is the SGS entropy diffusion at $r = 0.85 R_\odot$.

3. Results

We present the results of three runs, labeled as A, B, and C, with rotation periods of 8.3, 1.2 days, and 0.8 days, corresponding to 3, 20, and 30 times the solar rotation rate. We keep all other system parameters fixed. We summarize input and diagnostic quantities that characterize each simulation in Table 1.

3.1. Magnetic activity and quadrupole moment evolution

We begin our analysis by comparing the time-dependent diagnostics of magnetic fields and the gravitational quadrupole moment. In Fig. 1 we show the azimuthally averaged radial magnetic field (\bar{B}_r) near the surface of the stars at $r/R = 0.98$ (color contours), along with the evolution of the xx component of the gravitational quadrupole moment Q (black lines)². The latter is defined as

$$Q_{ij} = I_{ij} - \frac{1}{3} \delta_{ij} \operatorname{Tr} I, \quad (14)$$

where

$$I_{ij} = \int \rho(\mathbf{x}) x_i x_j \, dV \quad (15)$$

is the ij component of the inertia tensor expressed in Cartesian coordinates and $\rho(\mathbf{x})$ is the density. All of the simulations show low-amplitude variations of Q_{xx} on a timescale of roughly 0.2 years. These are attributed to sound waves and have a purely hydrodynamic origin (Navarrete et al. 2020). Hence such signals are left out of the data in this study by working with low-cadence snapshots and interpolating the data with a cubic interpolator. In Run A, the variations of Q_{xx} are small, on the order of $10^{39} - 2 \times 10^{39} \text{ kg m}^2$ and by visual inspection we estimate that they have a similar period (roughly 6–8 years) as the axisymmetric part of the magnetic field. Run B shows a larger amplitude long-term variation of Q_{xx} that repeats at least once in the data. Roughly half of the data for Run B, up to about 80 years, was presented in Navarrete et al. (2020). The steady decrease of Q_{xx} between $t \approx 30$ to $t \approx 85$ years was interpreted as a transient due to insufficient thermodynamic and magnetic saturation. However, with the longer time series we see that the quadrupole moment is modulated on a timescale of about 80 years. It also appears that Q_{xx} is roughly correlated to \bar{B}_r : low values of the quadrupole moment approximately coincide with times when \bar{B}_r is weak on both hemispheres ($t = 70$ – 85 and $t = 140$ – 160 years, respectively). The cycle is perhaps starting again at $t = 160$ as the magnetic activity appears to be resuming with a corresponding change in Q_{xx} . The largest variation of Q_{xx} occurs between $t = 100$ – 155 years, with an amplitude of 10^{40} kg m^2 . It corresponds to the largest variation of Q_{xx} of the three runs. Overall, the gravitational quadrupole moment appears to follow the radial magnetic field strength near the surface of the star independently of the hemispheric asymmetry. In contrast to the other two runs, diagnostics for Q_{xx} in Run C are available starting at $t = 0$ yr. The quadrupole moment in this run remains more or less constant and only starts to decrease after the magnetic field approaches the saturated regime at $t \approx 10$ yr. The magnetic field back-reacts and re-adjusts the thermodynamic quantities, such as density, after which Q_{xx} settles to a state with smaller variations around a mean value of $1.70 \times 10^{40} \text{ kg m}^2$. These variations are about half of those in Run A. As seen in Fig. 1, the axisymmetric part of B_r is similar in Runs A and C, but clearly different in Run B. In the first two, \bar{B}_r migrates toward higher latitudes in a regular fashion and in the latter the dynamo is more hemispheric such that activity alternates between both hemispheres seemingly every 50 to 60 years. Overall, cycles of Q_{xx} in Runs A and C follow more closely the polarity reversals of the magnetic

² We note that the values of Q_{xx} for Runs A and B differ from Navarrete et al. (2020). This is because in that study, I_{zz} was erroneously calculated (see Navarrete et al. 2021). However, this difference does not change their conclusions.

Table 1. Summary of simulation parameters.

Run	Ω/Ω_{\odot}	P_{rot} (days)	Ta	Co	$\text{Co}^{(\omega)}$	Ma	Re	Re_M	Pr	Pr_M	Pr_{SGS}	Δt (yr)
A	3	8.3	5.68×10^7	2.8	1.28	6.46×10^{-2}	66.6	66.6	58	1.0	2.5	39
B	20	1.2	2.52×10^9	62.4	12.4	3.29×10^{-2}	20.3	20.3	58	1.0	2.5	138
C	30	0.8	5.68×10^9	139.1	22.4	2.06×10^{-2}	13.6	13.6	58	1.0	2.5	145

Notes. Ω/Ω_{\odot} is the rotation rate in units of the mean solar angular velocity. Co and $\text{Co}^{(\omega)}$ are the Coriolis numbers, Ma is the volume and time averaged Mach number, Re and Re_M are the fluid and magnetic Reynolds numbers. Pr, Pr_M , and Pr_{SGS} are the fluid, magnetic, and subgrid scale Prandtl numbers, respectively. Δt is the total simulated time.

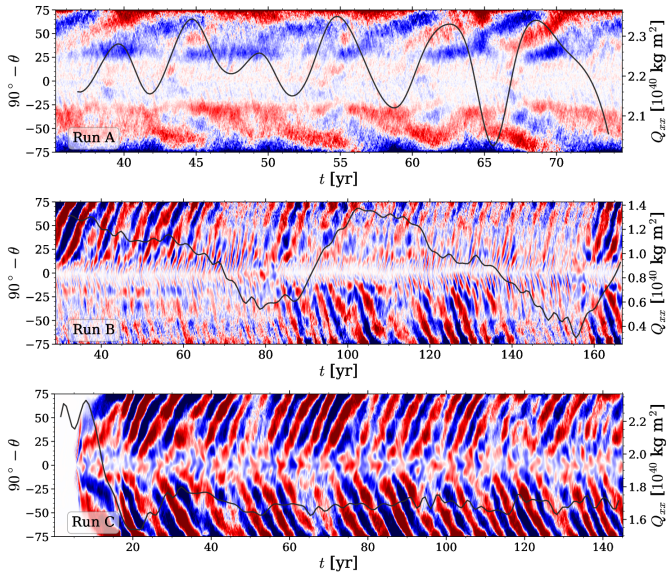


Fig. 1. Azimuthally averaged radial magnetic field (\overline{B}_r) near the surface of the domain at $r = 0.98R$ as a function of latitude and time for Run A (top, $P_{\text{rot}} = 8.3$ d), Run B (middle, $P_{\text{rot}} = 1.2$ d), and Run C (bottom, $P_{\text{rot}} = 0.8$ d). Q_{xx} for each run is shown from the time periods where this diagnostic is available. The color scale of \overline{B}_r in each panel has been clipped at ± 8 kG.

field. There are also such cycles in Run B. However, they are hidden by the longer cycle that follows the migration of the hemispheric component of the magnetic field.

In Fig. 2 we show instantaneous snapshots of the radial magnetic field near the surface of the three runs at the times of interest, that is, maxima (minima) of Q_{xx} at top (bottom) row. These correspond to $t = 62, 74$ yr for Run A, $t = 110, 155$ yr for Run B, $t = 64, 98$ yr for Run C. In Run A, a predominantly $m = 1$ large-scale mode is seen at high latitudes but this is subdominant in comparison to the axisymmetric ($m = 0$) component (see Appendix B). In Run B there is a dominant $m = 1$ mode on the northern hemisphere, while a predominantly $m = 2$ mode dominates on the southern hemisphere at the maximum. At the minimum of Q_{xx} (middle panel in the lower row), B_r is symmetric with respect to the equator with a dominating $m = 1$ mode on both hemispheres. These large-scale structures cover the entire hemispheres from the equator to the latitudinal boundaries. This is qualitatively similar to Run H of Viviani et al. (2018) and Run C of Cole et al. (2014). As suggested by Fig. 1, a similar pattern repeats for Run B at $t \approx 36$ yr and $t \approx 75$ yr but in opposite hemispheres. Run C is similar to Run B in the sense that the large-scale nonaxisymmetric structures are prominent over a large region, but the $m = 1$ and $m = 2$ modes appear to be similar in strength. These modes appear to alternate between the

hemispheres but the variations in the gravitational quadrupole moment are weak in this case in comparison to Run B. However, the low-order nonaxisymmetric fields in Run C are of the same order of magnitude as the $m = 0$ mode whereas in Run B the $m = 1$ mode is clearly stronger than the axisymmetric fields. A possible explanation of the smaller cycles of Q_{xx} found in Run C can be attributed to the dynamo solution. Slow rotators tend to produce dominant $m = 0$ modes. Faster rotators typically show a predominant $m = 1$ mode although sometimes the $m = 0$ component can become dominant again at very high rotation rates if the convection is only weakly supercritical (Viviani et al. 2018). It is plausible that this is happening in our Run C. These results suggest that a dominant nonaxisymmetric magnetic field with hemispheric asymmetry is associated with the strongest variations of Q .

3.2. Density variations and structural changes due to magnetic fields

The variations of the gravitational quadrupole moment are related to changes in the mass distribution within the star as can be seen from Eqs. (14) and (15). Snapshots of the density from all three runs near the surface of the star are shown in Fig. 3. As before, the shown times correspond to maxima (top row) and minima (bottom row) of Q_{xx} . Snapshots of the $m = 1$ and $m = 2$ modes of density are shown in the Appendix B.

In Run A there is an overall change in density between the two times. At $t = 62$ yr (top panel), when the gravitational quadrupole moment is larger, there are no noticeable large-scale nonaxisymmetric features, whereas when Q_{xx} is at a minimum ($t = 74$ yr), weak nonaxisymmetric features appear. This can be seen from the two blue stripes around $\theta = \pm 30^\circ$ where the overall density decreases with patches of increased (decreased) density around $\phi = 270^\circ$ ($\phi = 60^\circ$). Closer to the poles and near the equator the average density increases but no clear nonaxisymmetric features are present. In Run B we identify a few characteristics. First, when the quadrupole moment is larger at $t = 110$ yr, there is a clear asymmetry with respect to the equator, such that the density is larger close to the north pole. As Q_{xx} decreases, the asymmetry disappears, and nonaxisymmetric structures become visible at $230^\circ < \phi < 340^\circ$ and $\theta = \pm 40^\circ$. As the magnetic field changes its configuration from one that is dominated by an $m = 1$ mode only at the northern hemisphere to predominantly $m = 1$ on both hemispheres (see Fig. 2), the density field reacts and also changes to a nonaxisymmetric configuration with a corresponding change in the gravitational quadrupole moment. In contrast, large-scale density variations in Run C between the two times are clearly weaker. The density field at the surface remains symmetric with respect to the equator as well as in the azimuthal direction.

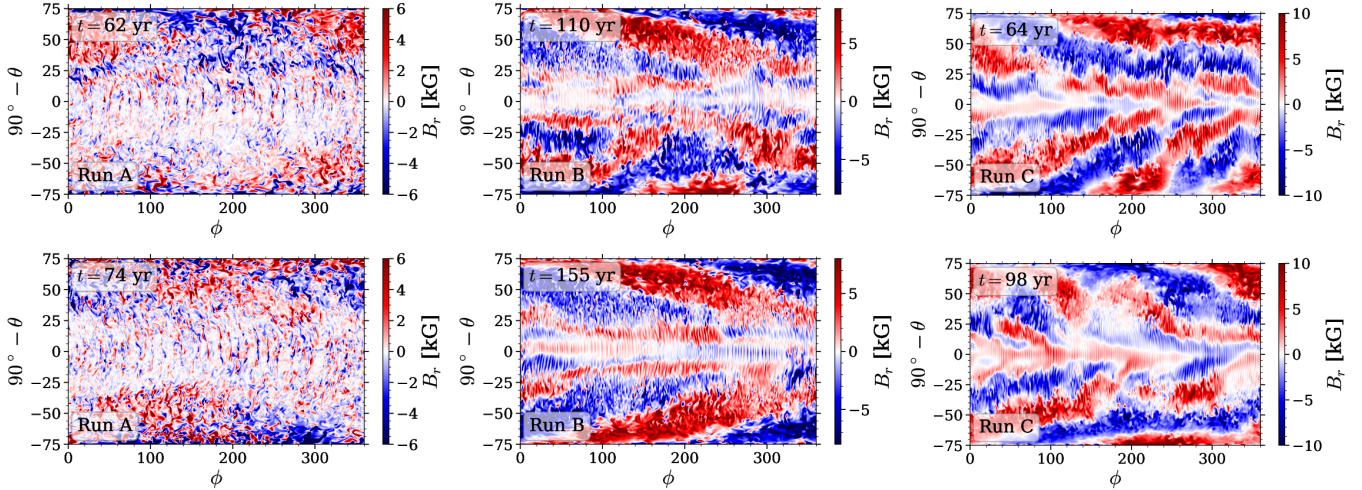


Fig. 2. Instantaneous radial magnetic field at $r = 0.98R$ for each run at two times. *Top (bottom) row*: corresponds to a maxima (minima) of Q_{xx} .

To investigate the importance of equatorial asymmetry on the gravitational quadrupole moment, we define the equatorially asymmetric part of density as

$$\rho_{\text{asym}}(r, \theta, \phi) = \frac{\rho(r, \theta, \phi) - \rho(r, -\theta, \phi)}{2} \quad (16)$$

and compute the root mean square according to

$$\rho_{\text{s,rms}} = \left(\langle \rho_{\text{asym}}^2 \rangle_{\theta\phi} \right)^{1/2}. \quad (17)$$

The time evolution of $\rho_{\text{s,rms}}$, together with Q_{xx} , is shown in the top row of Fig. 4. In Run A (left panel) there is an anticorrelation between the two. However, in the case of Run B (middle panel) there is a positive correlation between the two but with an apparent time delay. The rms value of $\rho_{\text{s,rms}}$ lags behind Q_{xx} by roughly 10 yr for example near the extrema between 80 and 100 yr. In Run C both the variations of the density and Q_{xx} are weak. It is also less clear whether a correlation between the two exists. The variations of $\rho_{\text{s,rms}}$ are between 6 to 10 times larger in Run B than in Runs A and C, indicating that the former is in a different dynamo regime where the magnetic field is more strongly coupled to the density field leading to stronger quadrupole moment variations.

The differences in density with respect to the equator should translate in variations of the moment of inertia aligned with the rotational axis of the star, namely, I_{zz} . The lower row of Fig. 4 shows the evolution of the three components of the inertia tensor that contribute to Q_{xx} , which is computed from

$$Q_{xx} = I_{xx} - \frac{1}{3} (I_{xx} + I_{yy} + I_{zz}). \quad (18)$$

The vertical component I_{zz} is always smaller than the two other components. In Runs A and C all components of I_{ij} have comparable variations, whereas in Run B (middle panel) the variations of I_{zz} are significantly larger. This coincides with larger variations of $\rho^{m=1,2}$ in this run. In Run B a maximum of Q_{xx} coincides with a minimum of I_{zz} . This corresponds to the star rotating slightly faster at maxima (minima) of Q_{xx} (I_{zz}).

To see such differences, we compute the azimuthally averaged rotation profiles

$$\bar{\Omega}(r, \theta) = \Omega_0 + \frac{\bar{u}_\phi(r, \theta)}{r \sin \theta} \quad (19)$$

for all runs, average them over time, and show the deviations from such averages during the two times of interest in Fig. 5. There are minor differences in the rotation profiles of Runs A and B between maxima and minima of Q_{xx} , while almost no differences are observed in Run C. Runs A and B have a larger difference between angular velocities of polar and equatorial regions at a minima of Q_{xx} (lower panels), but an accelerated northern pole is seen in the top panel of Run B. A large difference in differential rotation implies that the star would deform and adopt an ellipsoidal shape as a consequence of the centrifugal force, adding a further contribution to the quadrupole moment. However, as we have fixed boundary conditions, we cannot model such a reaction. All of our runs show a solar-like rotation profile with equatorial regions rotating faster than the poles as a consequence of Coriolis numbers above the transition region from antisolar to solar-like differential rotation. This transition occurs around $\text{Co} \gtrsim 1$ (see e.g., Gastine et al. 2014; Käpylä et al. 2014) whereas the rotation profile approaches solid body rotation for rapid rotation (e.g., Viviani et al. 2018; Käpylä 2021).

The energies of the axisymmetric and first two nonaxisymmetric modes of B_r are shown in the lower row of Fig. 6 and a scatter plot between $B_r^{m=i}$ and Q_{xx} is shown in the upper row. In Run A (first column) the axisymmetric $m = 0$ is dominant, which seems to be anticorrelated with Q_{xx} . There are short episodes where the $m = 0$ and $m = 1$ modes have comparable energies. The latter is correlated to Q_{xx} . In Run A, the $m = 2$ mode is always subdominant. From the scatter plot we see that no noticeable increase in magnetic energy is needed to reach a larger quadrupole moment. The situation in Run B is different as there is a persistent $m = 1$ mode that dominates throughout the simulation with minor fluctuations in its energy. The axisymmetric mode seems to be correlated to Q_{xx} . This is because, as explained in the previous section, it produces equatorially asymmetric density fluctuations that modulate the moment of inertia aligned with the rotation axis of the star. The second nonaxisymmetric mode ($m = 2$) is as strong as the axisymmetric mode and also correlates with Q_{xx} . Larger quadrupole moment values are related to higher energies in the $m = 0$ and $m = 2$ modes. In Run C all modes have similar energy levels, with $m = 0$ being slightly stronger than the other two. The scatter plot reveals that there is no relation between the magnetic energy and the quadrupole moment.

To quantify the relation between magnetic field modes and quadrupole moment, we perform a correlation analysis. We use the Pearson correlation coefficient to study the linear correlation

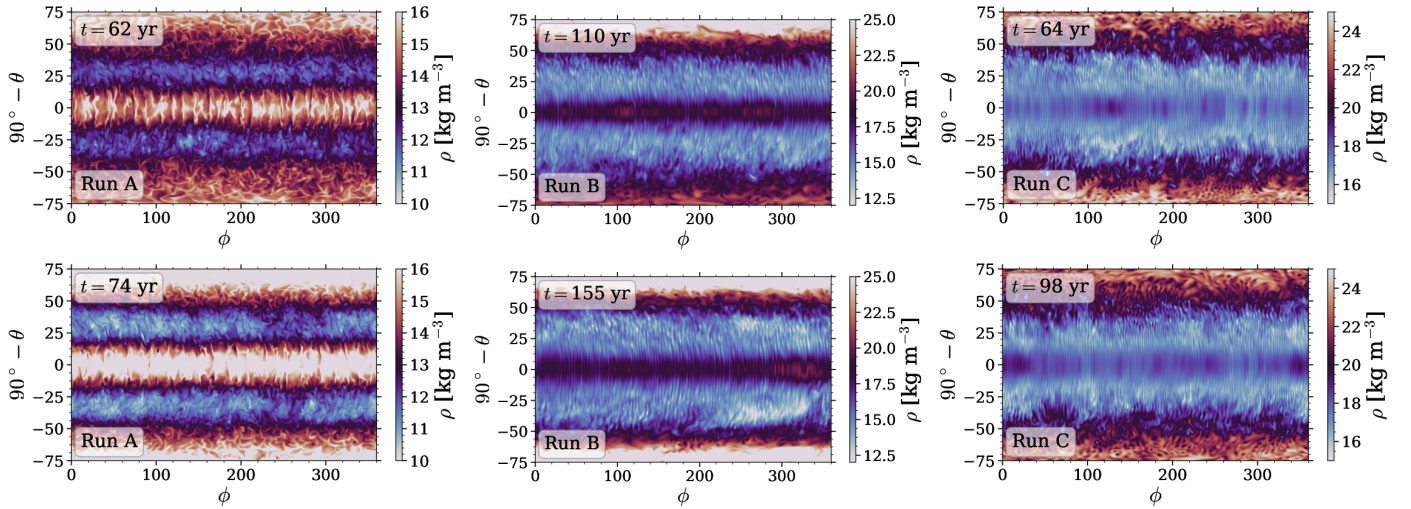


Fig. 3. Instantaneous snapshots of density at $r = 0.98R$ for each run.

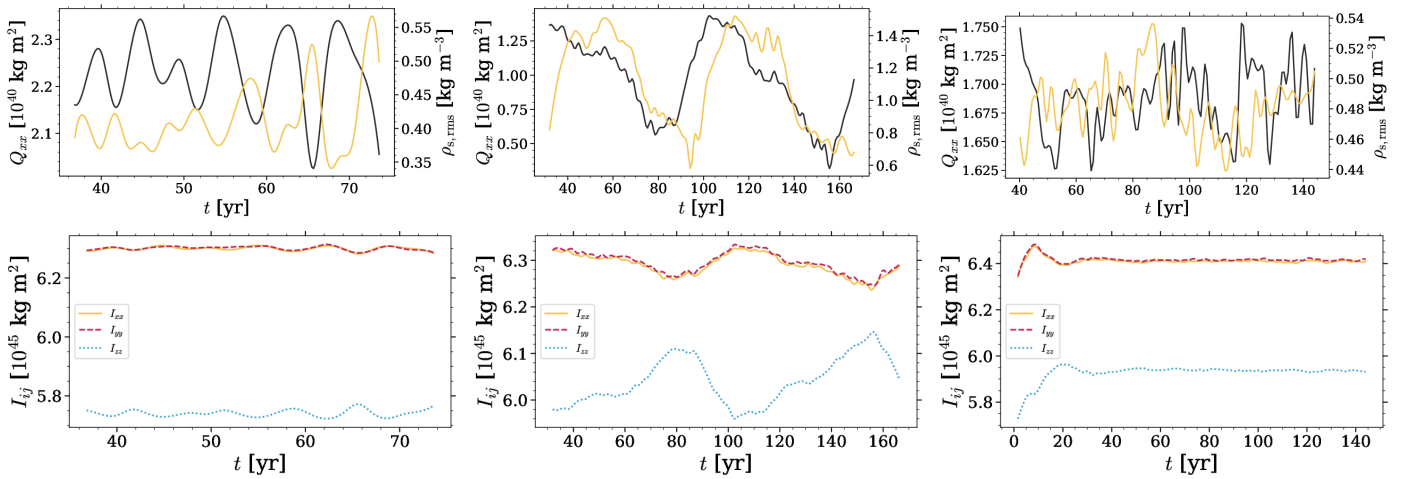


Fig. 4. *Top row:* Q_{zx} (black) and rms value of the equatorially asymmetric part of density $\rho_{s,rms}$ (yellow) according to Eq. (17) as functions of time. *Bottom row:* time evolution of the diagonal components of the inertia tensor. First, second, and third columns correspond respectively to runs A, B, and C.

between the density and magnetic fields. The coefficient between a paired data (x, y) of n pairs is defined as

$$x|y = \frac{\sum_{i=1}^n (x_i - \bar{x})(y_i - \bar{y})}{\sqrt{\sum_{i=1}^n (x_i - \bar{x})^2} \sqrt{\sum_{i=1}^n (y_i - \bar{y})^2}}, \quad (20)$$

where \bar{x} and \bar{y} are the sample mean and $-1 \leq x|y \leq 1$. A value of $x|y = 1$ ($x|y = -1$) implies perfect (anti-)correlation.

The correlations between the gravitational quadrupole moment and magnetic energy are calculated using the data presented in Fig. 6 and in this case the barred quantities in Eq. (20) represent time averages of Q_{zx} and E_{mag} , whereas x_i and y_i are the time-dependent quantities of Q_{zx} (calculated over the whole volume) and E_{mag} (calculated over the surface layer). This is shown in the second, third, and fourth columns of Table 2. In general, we find correlations higher than 0.5 for the $m = 1$ mode in Run A and for the $m = 1$ and $m = 2$ modes in B.

Next, we compute the correlation coefficients between the mean surface density $\bar{\rho}_{surf}$ and quadrupole moment, and $\bar{\rho}_{surf}$ and the magnetic energies. These are shown in the last four columns of Table 2. In each run we find that the values of $\bar{\rho}_{surf}|Q_{zx}$ are relatively large. This is due to the direct relation between the

density distribution and Q_{zx} . The outer regions of the stars are particularly important due to the x^2 dependence of the inertia tensor. As noted earlier, the dynamo solution in Run B alternates between the two hemispheres and so does the density field. As $\bar{\rho}_{surf}$ increases, so does I_{zz} and thus Q_{zx} decreases (see Eq. (18)). Overall, we see the clearest correlations in Run B.

The magnetic energy increases with the rotation rate as expected, but this does not suffice to explain the variations in the gravitational quadrupole moment. Overall, Run B has the largest magnetic energy and Run A and C have comparable energies (see Table 3). However, Run C has smaller fluctuations in Q_{zx} which can be attributed to the fact that the variations of the magnetic field do not result in significant density perturbations relevant for the quadrupole moment.

3.3. Azimuthal dynamo waves

Azimuthal dynamo waves (ADWs) are magnetic structures that migrate in the azimuthal direction. ADWs can be prograde or retrograde and their propagation is unaffected by the differential rotation of the star (see e.g., Krause & Rädler 1980; Cole et al. 2014; Viviani et al. 2018). The periods of ADWs are usually on

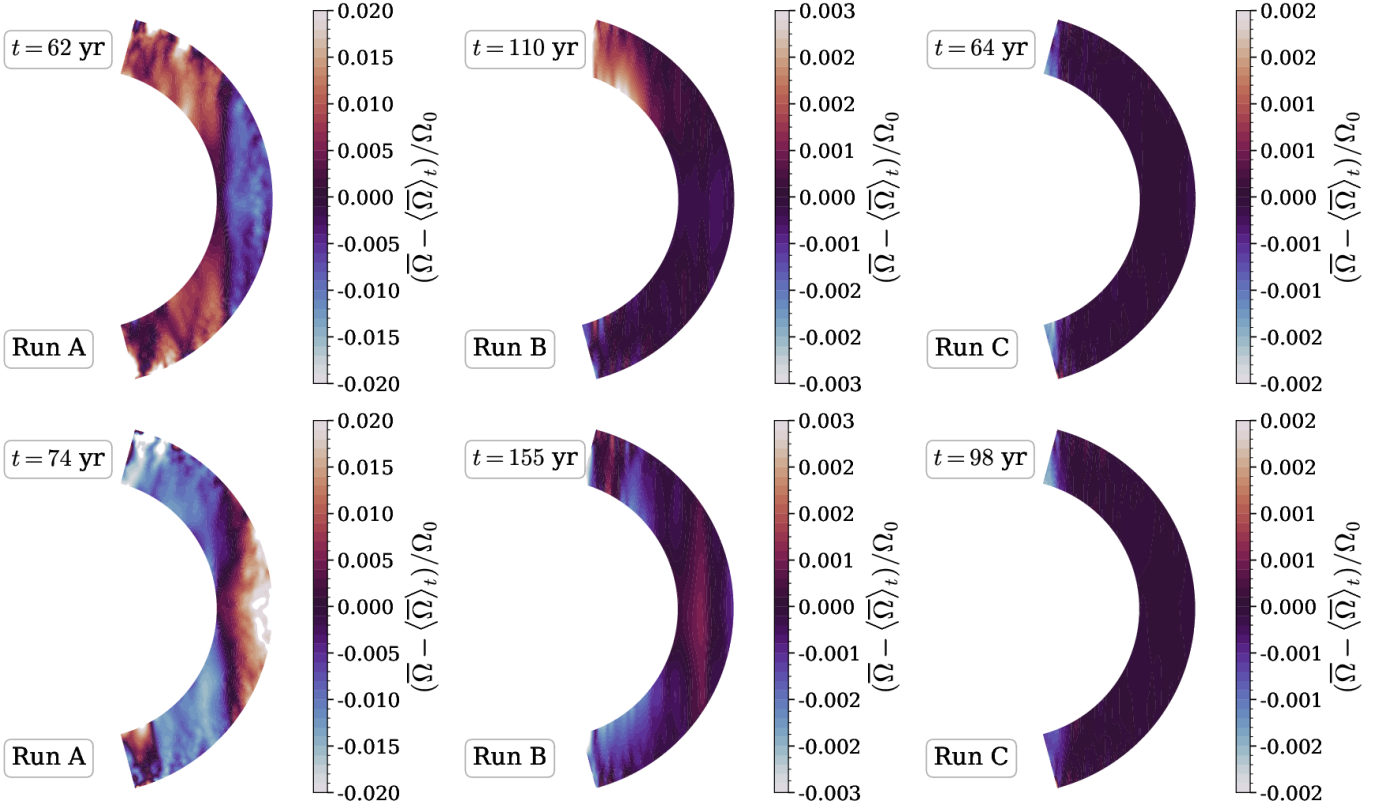


Fig. 5. Deviations from the time-averaged mean angular velocity ($\bar{\Omega} - \langle \bar{\Omega} \rangle_t$) normalized by the angular velocity of the frame of reference (Ω_0) for each run from the times indicated in the legends.

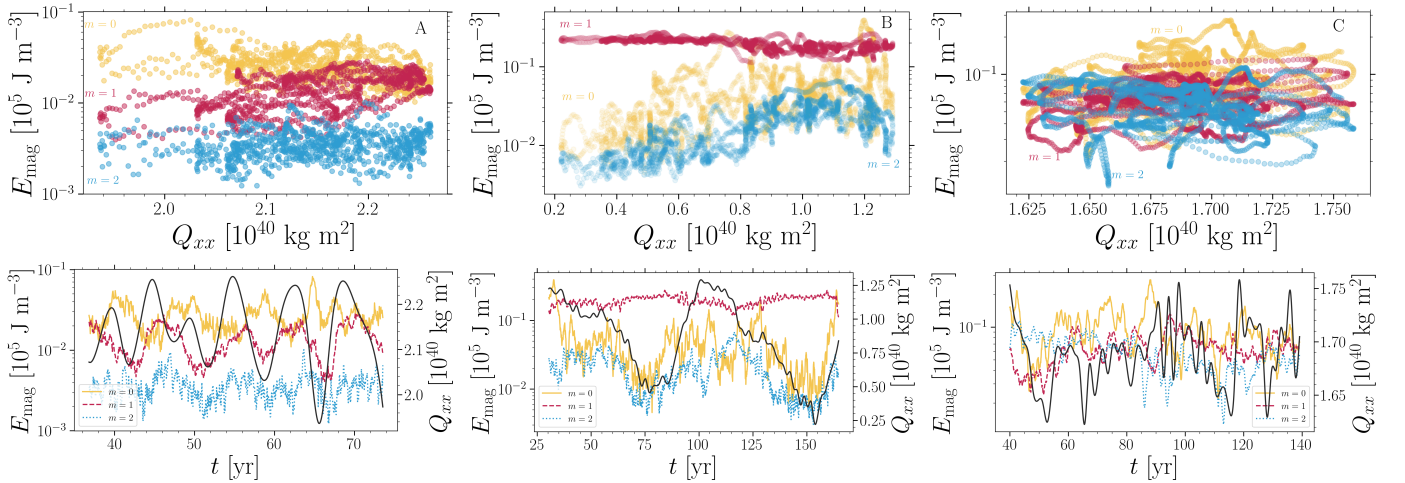


Fig. 6. Quadrupole moment, density, and moments of inertia. *Top row:* scatter plot of the magnetic field energy and the quadrupole moment. *Bottom row:* time evolution of the gravitational quadrupole moment (black line) together with the magnetic energy contained in the axisymmetric mode ($m = 0$, yellow), as well as the first ($m = 1$, red) and second ($m = 2$, blue) non-axisymmetric modes. Run A, Run B, and Run C are shown in the left, middle, and right columns respectively.

Table 2. Correlation coefficients between the time series of the quadrupole moment and magnetic energy, mean surface density and quadrupole moment, and mean surface density and magnetic energy.

Run	$Q_{xx} E_{\text{mag}}^{m=0}$	$Q_{xx} E_{\text{mag}}^{m=1}$	$Q_{xx} E_{\text{mag}}^{m=2}$	$\bar{\rho}_{\text{surf}} Q_{xx}$	$\bar{\rho}_{\text{surf}} E_{\text{mag}}^{m=0}$	$\bar{\rho}_{\text{surf}} E_{\text{mag}}^{m=1}$	$\bar{\rho}_{\text{surf}} E_{\text{mag}}^{m=2}$
A	-0.41	0.54	0.13	-0.67	0.20	-0.18	-0.07
B	0.38	-0.64	0.66	-0.94	-0.40	-0.53	-0.57
C	0.26	0.22	-0.34	-0.40	0.25	0.11	-0.11

Table 3. Summary of some quantities of interest corresponding to data shown in Fig. 1.

Run	Q_{xx}^{\max}	Q_{xx}^{\min}	\bar{B}_r^{\max}	\bar{B}_r^{\min}	$E_{\text{mag,total}}^{\max}$	$E_{\text{mag,total}}^{\min}$
A	2.25	1.94	8.65	-9.70	2.98	1.26
B	1.38	0.315	24.7	-19.7	3.98	2.28
C	1.80	1.54	16.8	-13.8	2.32	1.30

Notes. Q_{xx} is in units of 10^{40} kg m² and \bar{B}_r in units of kG. $E_{\text{mag,total}}$ is the volume-averaged magnetic energy in units of 10^5 J m⁻³.

the order of a few years for slow rotators and of tens of years for faster rotators (Viviani et al. 2018). This is comparable to the period of the quadrupole moment variations of the present study. We therefore briefly study ADWs. We take $m = 1$ and $m = 2$ modes of the radial magnetic field near the surface of each run at latitude $+60^\circ$ and show the evolution of the field in Fig. 7 and its phase in Fig. 8.

Run A has an $m = 1$ ADW that migrates in the retrograde direction with a period of ~ 8 years in particular after around $t = 60$ yr. Meanwhile, the $m = 2$ ADW has a similar amplitude with no clear periodicity. In Run B there is a clear $m = 1$ wave which migrates in the prograde direction. However, between 115 and 145 yr the migratory process is stalled for nearly thirty years. The ADW in Run B has a period of roughly ~ 80 – 100 years. There is an $m = 2$ ADW but it is only noticeable during the first ~ 40 years of the simulation. In Run C there are two equally strong ADWs. Both migrate in a prograde way with the difference that the period of the $m = 1$ wave is shorter than the one of $m = 2$.

The evolution of the phase of the $m = 1$ mode correlates well with the evolution of the gravitational quadrupole moment in Runs A and B, whereas the second nonaxisymmetric mode is noisier and does not correlate with Q_{xx} . The phase of $B_r^{m=1}$ does not show any particular evolution in Run C, while for $m = 2$ the phase is constantly decreasing which is uncorrelated with Q_{xx} . The cases of Runs A and B point to an underlying relation between a nonaxisymmetric dynamo mode and the gravitational quadrupole moment evolution.

4. Discussion and implications

The Applegate mechanism (Applegate 1992) is based on the redistribution of angular momentum throughout the star due to the centrifugal force. More recently, Lanza (2020) presented a new mechanism where the centrifugal force is no longer needed. In this work the quadrupole moment is constant in the frame of reference of the magnetically active star due to a time-invariant nonaxisymmetric magnetic field modeled by a single flux tube. The companion star experiences a time-varying nonaxisymmetric gravitational quadrupole moment due to the assumption that the active star is not tidally locked.

In our simulations we compute the gravitational quadrupole moment in the rotating frame of reference of the star. The simulations thus provide a test whether magnetic activity can significantly influence stellar structure. We stress that the physical process occurring here is not the classical Applegate mechanism which is based on the centrifugal force, and which is not included in our simulations. The results described in Sect. 3 show that the connection between magnetic fields and gravitational quadrupole moment is quite complex. It is due to the asymmetry of the magnetic field with respect to the equator rather than due to nonaxisymmetry, which is particularly notice-

able in Run B. The three simulations we present differ only in the rotation rate of the star and yet they present different scenarios of quadrupole moment variations.

4.1. Behavior of the dynamo itself

Simulations of stellar magneto-convection have shown that dynamo solutions depend mainly on the rotation rate of the star. For example, Viviani et al. (2018) studied the transition from axi- to nonaxisymmetric magnetic fields as a function of rotation and found that the transition to nonaxisymmetry occurs for $\Omega \gtrsim 1.8\Omega_\odot$. However, Viviani et al. (2018) found that at sufficiently rapid rotation, the magnetic field returns to a predominantly axisymmetric configuration if the resolution is not high enough. A similar sequence is also observed in the simulations described in this paper. Run A is at a regime where the axisymmetric mode is slightly stronger than the first nonaxisymmetric mode. The rotation rate in Run B is 6.7 times greater than in Run A and there the $m = 1$ mode dominates, while $m = 0$ and $m = 2$ are comparable. In Run C, with 10 times faster rotation than in Run A, the dominant mode is again $m = 0$. If the resolution was to be increased, corresponding to higher Reynolds numbers, it is possible that a nonaxisymmetric solution with stronger quadrupole moment variations would be recovered.

Besides resolution effects, it is possible that Run B is in a parameter regime where hemispherical dynamos are preferred; see, for example, Grote & Busse (2000), Busse (2002), and Käpylä et al. (2010). Brown et al. (2020) reported a cyclic single-hemisphere dynamo in a simulation of a fully convective star, and mentioned that such dynamos are present in other simulations with similar parameters. Käpylä (2021) presented a set of simulations of fully convective stars where in a single run short periods of hemispheric dynamo action were seen, but even in this case the dynamo is predominantly present on both hemispheres. It is important to explore this parameter regime in more detail as it can potentially help to address the question of whether the ETVs in PCEBs have a magnetic origin. If this is the main ingredient, however, it would imply that PCEBs that show variations in the O–C diagram are in this particular regime.

4.2. Classical Applegate mechanism

If we first consider the case where the eclipsing time variation is due to a time-dependent quadrupole moment (classical Applegate mechanism), the expected period variation due to a change of the gravitational quadrupole moment can be computed from (Applegate 1992)

$$\frac{\Delta P}{P} = -9 \frac{\Delta Q_{xx}}{M a^2} = 2\pi \frac{\text{O-C}}{P_{\text{mod}}}, \quad (21)$$

where $\Delta P/P$ is the amplitude of the orbital period modulation, M the stellar mass, and a the binary separation, O–C is the amplitude of the observed-minus-calculated diagram and P_{mod} its modulation period. We choose V471 Tau as a reference system with which we compare our results, The reason for this is that its main-sequence star has a mass of $M = 0.93 M_\odot$ and is thus structurally similar to the Sun and the current simulations. It is also rotating at a speed that is computationally feasible to achieve, whereas in many other systems the main-sequence stars have lower masses and rotation rates up to a hundred times the one of the Sun. Our results are only applicable to PCEBs where the magnetically active star has a Sun-like structure. This is because our model is constructed to resemble such stars. We

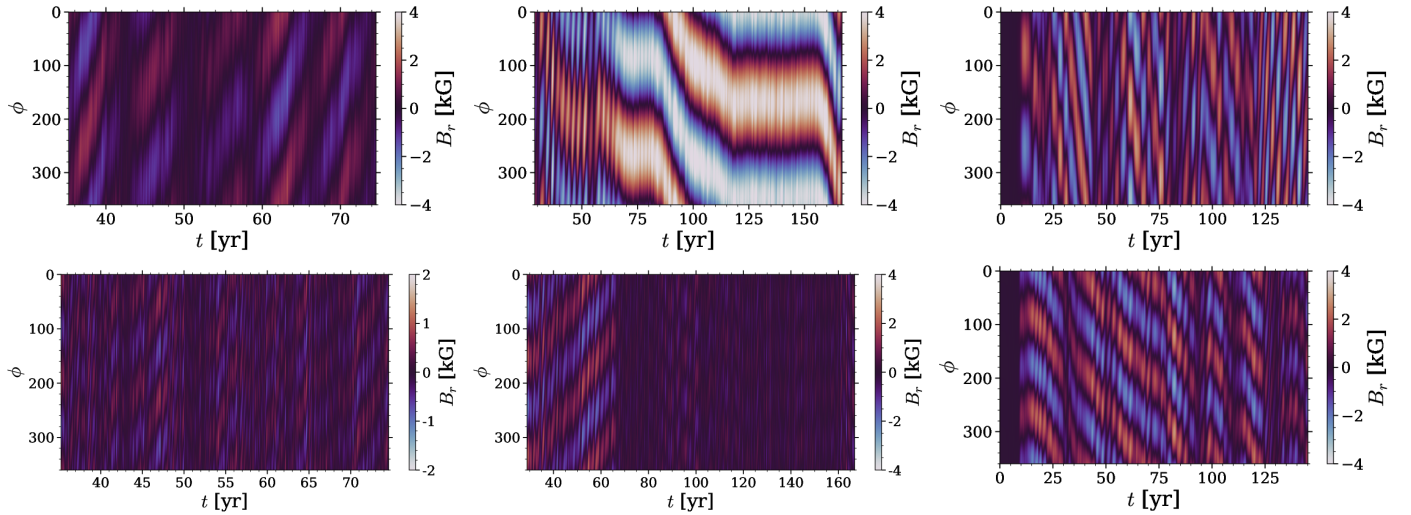


Fig. 7. Migration of the $m = 1$ (top row) and $m = 2$ (bottom row) modes of the radial magnetic field at the surface along the longitudinal direction, for Run A (left), Run B (middle), and Run C (right).

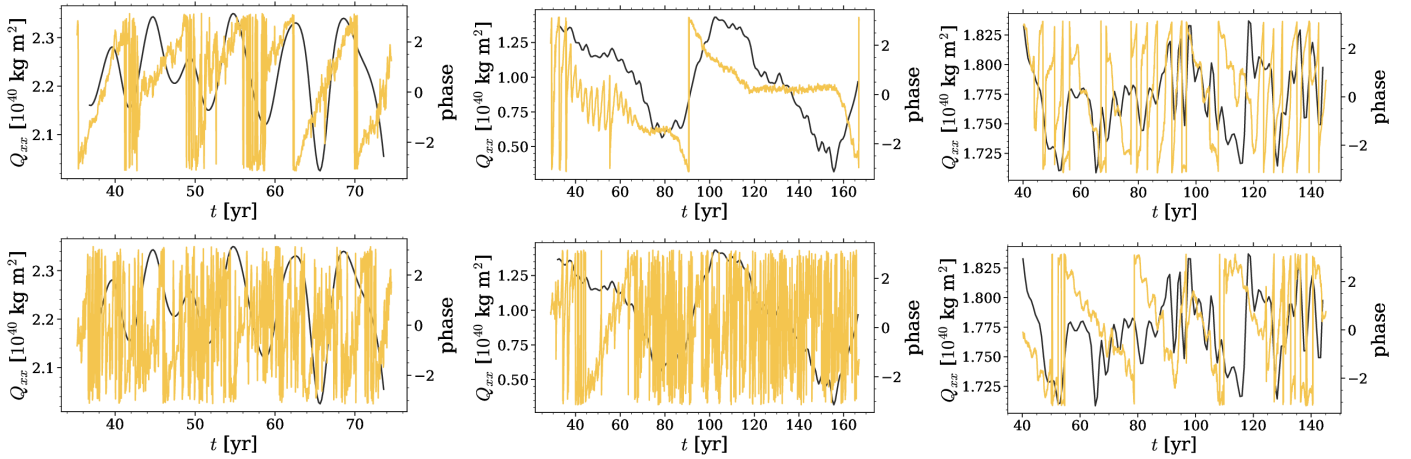


Fig. 8. Time evolution of the phase of the $m = 1$ (top row) and $m = 2$ modes (bottom row) of radial magnetic field at $\phi = 180^\circ$ for Run A (left panels), Run B (middle panels), and Run C (right panels) in yellow. The black line corresponds to Q_{xx} .

nevertheless note that this comparison is very approximate, as for example the Reynolds numbers of a real stellar system cannot be numerically reproduced.

For V471 Tau, the orbital separation is $a = 3.3 R_\odot$ and there are two contributions to the orbital period modulation that individually result in two orbital period modulations (Marchioni et al. 2018). These are

$$(\Delta P/P)_1 = 8.5 \times 10^{-7}, \quad (22)$$

$$(\Delta P/P)_2 = 4.5 \times 10^{-7}. \quad (23)$$

The corresponding quadrupole moment variations are

$$\Delta Q_{xx,1} = 9.4 \times 10^{41} \text{ kg m}^2, \quad (24)$$

$$\Delta Q_{xx,2} = 4.5 \times 10^{41} \text{ kg m}^2. \quad (25)$$

For the purpose of comparing with the quadrupole moment variations in simulations, we recall here that density fluctuations and the quadrupole moment itself need to be scaled as explained in Navarrete et al. (2020). They scale as

$$\Delta \rho \sim \mathcal{L}_r^{2/3}, \quad (26)$$

where \mathcal{L}_r is the ratio between the luminosities in the simulation and the target star, that is,

$$\mathcal{L}_r = \frac{\mathcal{L}_{\text{sim}}}{\mathcal{L}_\star}, \quad (27)$$

so the quadrupole moment is accordingly scaled as

$$Q_\star = \frac{1}{\mathcal{L}_r^{2/3}} Q_{\text{sim}}. \quad (28)$$

Details of the scaling are presented in Appendix A.

In Run B the amplitude of the variation is $\Delta Q_{xx} = 1.2 \times 10^{40} \text{ kg m}^2$ corresponding to $\Delta P/P = 1 \times 10^{-8}$. By adopting a modulation period of $P_{\text{mod}} = 80 \text{ yr}$, which corresponds to the period of Q_{xx} , we have an observed minus calculated value of O-C = 4.7 s. This O-C amplitude is still four and thirty times smaller than the values reported by Marchioni et al. (2018). There are a few possible reasons behind this mismatch. First, we are not including the centrifugal force and so the quadrupole moment fluctuations are produced by the evolution of the magnetic field and the resulting redistribution of the density rather than by the deformation of the star like in the Applegate mechanism. Secondly, the stars we are modeling have convective

envelopes of 30% of the radius, whereas the main-sequence star in the target system V471 Tau has a mass of $0.93 M_{\odot}$ and therefore a slightly more extended CZ. In a deeper CZ it is possible to perturb the density and the angular momentum distribution in a larger portion of the star (Völschow et al. 2018), although we expect this contribution to be very small. Lastly, we are imposing sphericity which is especially important at the surface of the star. Boundary conditions that dynamically react to the physical quantities inside of the star may allow larger variations of the quadrupole moment, especially if the star change its shape and size.

4.3. Models without tidal locking

In the previous calculation of $\Delta P/P$ following Applegate (1992), we made the implicit assumption of tidal locking and that the stellar rotation axis is perpendicular to the plane of the orbital motion. In this scenario, the \hat{x} axis points towards the companion and thus it rotates together with the stellar spin. Under those conditions, only the Q_{xx} component of the gravitational quadrupole moment contributes to the modulation of the binary period (Applegate 1992). In contrast, in the scenario put forward by Applegate (1989) and Lanza (2020), the star is not yet tidally locked, and its companion effectively experiences a time-varying quadrupole moment due to the relative rotation of the magnetically active star. This holds even if the quadrupole moment in the corotating frame of the star was constant. This implies then that different components of Q_{ij} contribute. In the simplified Lanza (2020) scenario, the magnetic field is modeled as a permanent single flux tube that lies at the equator and produces a nonaxisymmetric density distribution and thus, a permanent nonaxisymmetric gravitational quadrupole moment.

While there is a strong nonaxisymmetric magnetic field in our Run B, it is stronger at mid- and at high latitudes rather than at the equator. In our simulations, the choice of the \hat{x} and \hat{y} axes in the equatorial plane along which the moments of inertia are calculated is arbitrary, that is, as the companion star is not being modeled. Once fixed, we perform rotations about the \hat{z} axis in steps of $\pi/16$ up to π , and then we calculate the two moments of inertia about the rotated axes. These axes would correspond to \hat{s} and \hat{s}' of Lanza (2020). The former is the rotated \hat{x} axis, and the latter is the rotated \hat{y} axis. In Lanza (2020) \hat{s} is chosen to be along the axis of symmetry of the magnetic flux tube, which is the only magnetic structure in the CZ of the magnetically active star. In our simulations the rotation is not unique as there is no single radial magnetic field structure that extends from the bottom to the surface of the CZ in our simulations that would otherwise allow us to unequivocally choose \hat{s} . However, a clear radial magnetic structure at the equator is seen at $t = 155$ yr (see Fig. 9), but magnetic fields with different structure and strength dominate at different latitudes. In this configuration, the nonaxisymmetric quadrupole moment is defined as $T = I_s - I'_s$, where I_s and I'_s are the moments of inertia about the \hat{s} and \hat{s}' axes. The moment of inertia of the active star about the spin axis is $I_p = I_{xx} + I_{yy}$. The order of magnitude of the period variations can then be estimated as (Eq. (2) of Lanza 2020)

$$\frac{T}{I_p} \approx \frac{4}{3} \left(\frac{M_T}{m_S} \right) \left(\frac{ma^2}{I_p} \right) \left(\frac{P}{P_{\text{mod}}} \right) \left| \frac{\Delta P}{P} \right|, \quad (29)$$

where M_T is the total mass of the binary, m_S is the mass of the companion, m is the reduced mass, P is the orbital period, and P_{mod} is the modulation period. We take the density fields of Run B at $t = 110$ yr and $t = 155$ yr and compute the two

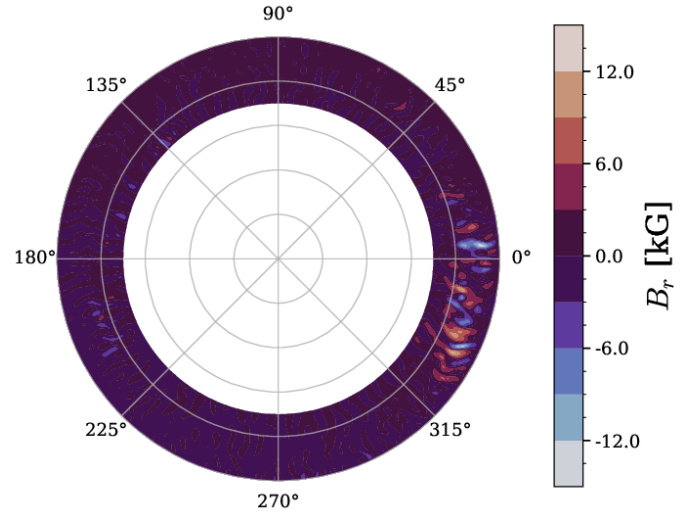


Fig. 9. Radial magnetic field of Run B at the equator at $t = 155$ yr. The \hat{x} and \hat{y} axes lie at $\phi = 0^\circ$ and $\phi = 90^\circ$, respectively. The \hat{s} and \hat{s}' axes are obtained by performing clockwise rotations.

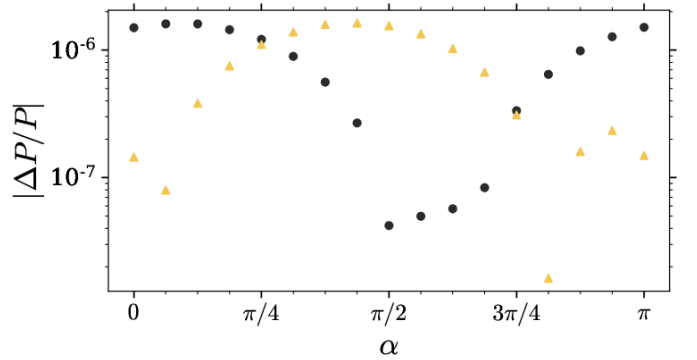


Fig. 10. Absolute value of $\Delta P/P$ as a function of separation angle α between \hat{x} and \hat{s} for $t = 110$ yr (black dots) and $t = 155$ yr (yellow triangles).

quadrupole moments T and I_p . By using Eq. (29) and the parameters of V471 Tau (see e.g., Hardy et al. 2015; Vaccaro et al. 2015) we can obtain an order of magnitude estimate of $\Delta P/P$. Figure 10 shows the absolute value of the amplitude of the orbital period modulation as a function of separation angle α between \hat{x} and \hat{s} for $t = 110$ yr (black dots) and $t = 155$ yr (yellow triangles). $|\Delta P/P|$ ranges between 1.5×10^{-7} and 1.5×10^{-6} , which contains the two contributions to the observed variations as well as their sum (Marchioni et al. 2018). From our simulations we get a value of I_p that is of the same order of magnitude as in Lanza (2020), while T is about one order of magnitude larger here. It is important to note that we have obtained T based on a detailed 3D magneto-hydrodynamical simulation, while Lanza (2020) simply calculated which T would be required to explain the observed ETVs.

In general, the gravitational potential felt by the companion can be written as (Applegate 1992; Lanza 2020)

$$\Phi = -\frac{GM}{r} - \frac{3G}{2r^3} \sum_{i,j} \frac{Q_{ij}x_i x_j}{r^2}, \quad (30)$$

where G is the gravitational constant, M is the mass of the active star, r is the distance between the center of the active star and the

companion, Q_{ij} is the quadrupole moment tensor, and \mathbf{x} refers to Cartesian coordinates. Writing out the summation explicitly and expressing x_i and x_j in a spherical coordinate system (r, θ', ϕ') with its origin coinciding with the center of the star, we arrive at

$$\begin{aligned} \Phi = & -\frac{GM}{r} - \frac{3G}{2r^3} \left\{ Q_{xx} \sin^2 \theta' \cos^2 \phi' \right. \\ & + Q_{yy} \sin^2 \theta' \sin^2 \phi' \\ & + Q_{zz} \cos^2 \theta' \\ & + 2 \left(Q_{xy} \sin^2 \theta' \cos \phi' \sin \phi' \right. \\ & + Q_{xz} \sin \theta' \cos \theta' \cos \phi' \\ & \left. \left. + Q_{yz} \sin \theta' \cos \theta' \sin \phi' \right) \right\}. \end{aligned} \quad (31)$$

The case of $\theta' = \pi/2$ and $\phi' = 0$ is analogous to the assumptions that the rotation axis is perpendicular to the plane of the orbit and that the orbital motion is tidally locked, respectively. By assuming only the former, Eq. (31) is reduced to

$$\begin{aligned} \Phi = & -\frac{GM}{r} - \frac{3G}{2r^3} \left(Q_{xx} \cos^2 \phi' \right. \\ & \left. + Q_{yy} \sin^2 \phi' + 2Q_{xy} \cos \phi' \sin \phi' \right). \end{aligned} \quad (32)$$

Here the effects of deviations from tidal locking can be modeled by making ϕ' time-dependent. There are two alternatives, namely

$$\phi'_1 = \alpha \cos(\omega t), \quad (33)$$

$$\phi'_2 = \omega t. \quad (34)$$

In the former case, the companion is seen in the frame of reference of the rotating star as oscillating in the orbital plane with amplitude α and angular velocity ω . In that case, ϕ'_1 corresponds to the analogous of the libration model. The latter expression for ϕ'_2 corresponds to the circulation model presented by Lanza (2020). This introduces two further contributions to the binary period variation that come from Q_{yy} and Q_{xy} (see Eq. (32)). In Run B Q_{yy} is, on average, the same as Q_{xx} . Meanwhile, Q_{xy} is 10^2 – 10^3 times smaller so it can be neglected. Thus,

$$\Phi = -\frac{GM}{r} - \frac{3G}{2r^3} \left(Q_{xx} \cos^2 \phi' + Q_{yy} \sin^2 \phi' \right). \quad (35)$$

In contrast to previous studies, we can directly calculate each component of the gravitational quadrupole moment from our simulations. In this case it is advantageous to use Eqs. (31) and (32) rather than taking the limit of $\phi' = 0$. However, we would need to use new expressions to derive $\Delta P/P$ considering the libration and circulation models. Alternatively, it is also possible to try different values of α and ω , and then directly solve Eq. (31) in a two-body simulation, which is however beyond the scope of the presented study. The influence of differences between Q_{xx} and Q_{yy} can be studied with N -body simulations by prescribing their time evolution and varying their amplitudes. It would be interesting to derive the parameters that can reproduce the observations and to compare them with our simulations.

5. Conclusions

We have presented three MHD simulations of stellar convection with different rotation rates, and studied the gravitational quadrupole moment and its connection to dynamo-generated

magnetic fields. The analysis is based on a spherical harmonic decomposition of density and magnetic fields. Our results for Run B ($P = 1.2$ days) show that a hemispheric dynamo mode can be an important ingredient for the eclipsing time variations in close binaries. This hemispheric dynamo produces equatorially asymmetric density variations and changes the moment of inertia along the rotation axis. The hemispheric activity migrates seemingly periodically between hemispheres and modulates the gravitational quadrupole moment. Furthermore, nonaxisymmetric magnetic fields modulate the other two diagonal components of the inertia tensor, adding a further modulation of Q . We also expect to have a further modulation of Q that comes from the centrifugal force which will be included in a future work as it is the responsible for the angular momentum redistribution in the Applegate mechanism (Applegate 1992). Linear correlation analysis confirms the role of the magnetic field in changing the quadrupole moment via density variations (Table 2) and the scatter plot between magnetic energy and quadrupole moment shows that large quadrupole moments are related to increased magnetic energy (see Fig. 6).

When our results are interpreted in the context of the classical Applegate mechanism, that is the star is tidally locked, then only the Q_{xx} component of the quadrupole moment contributes to the period variations. In this scenario, we obtain orbital period modulations between one and two orders of magnitude smaller than observed in the target system V471 Tau (Marchionni et al. 2018). We emphasize that our results here should be taken with caution. We model the CZ of a Sun-like star while the CZ extends inward for less massive stars which are more common among PCEBs. It is yet to be investigated if large enough quadrupole moments are found in magnetohydrodynamical simulations of fully convective stars.

In the context of the models by Applegate (1989) and Lanza (2020), the order of magnitude estimate of the amplitude of the period modulation is 10^{-6} – 10^{-7} . This range encompasses the two observed contributions to the O–C diagram, as well as their combined effect. The observed period variations could be a combination of both, namely, both the axi- and nonaxisymmetric quadrupole moments contribute to them. The implication of the first interpretation is that there must be a hemispheric dynamo with an alternating active hemisphere in order to modulate Q_{xx} as seen in our simulations. The second interpretation implies that the star is not tidally locked and that there is a nonaxisymmetric magnetic field in the CZ of the magnetically active star. We emphasize, however, given the caveats of the model such as imposed spherical symmetry, the coincidence in the order of magnitude between the ETVs, and in our model must be taken with caution. More importantly, relaxing the assumption of tidal locking leads to period variations that are between one and two orders of magnitude larger than in the tidal-locking scenario.

Observational studies suggest that both scenarios discussed, namely asymmetric magnetic fields and nontidally locked stars, are plausible. Firstly, a recent study by Klein et al. (2021) reported the reconstruction of the surface magnetic field of Proxima Centauri using Zeeman-Doppler imaging (ZDI). They found that the magnetic field is mainly poloidal with a dominant feature that is tilted at 51° to the rotation axis (see their Fig. 3) with a strength of 135 G, that is a field distribution that is asymmetric with respect to the equator. This is a rather weak field so density fluctuations should be smaller than what we find in our simulations. However, Proxima Centauri is a slowly rotating M5.5 fully-convective star. The magnetic field strength of fully-convective

stars increases with rotation until a saturation regime is reached, as measured by X-ray emission (see e.g., [Wright & Drake 2016](#)), so density variations in magnetically active components of PCEBs are expected to be larger due to the increased magnetic field strength. This might also be the case for more evolved partially convective stars as a similar scaling property was recently found ([Lehtinen et al. 2020](#)). Studying the differences of stellar spots during a minima and maxima of O–C diagrams in PCEBs will provide direct evidence of the connection between the underlying dynamo and the orbital period variations. Secondly, the determination of tidal synchronization is equally important, as a deviation from synchronization results in a more complex relation between the gravitational quadrupole moment and eclipsing time variations and potentially larger binary period variations (see [Lanza 2020](#), and also Sect. 4.3 of this paper). [Lurie et al. \(2017\)](#) studied tidal synchronization of F, G, and K stars in short-period binaries. The authors find 21 eclipsing binaries that are not synchronized and argue that this could be explained either because they are young or have a complex dynamical history. Considering the dynamical evolution of PCEBs, where the secondary star is engulfed by the companion and spirals inwards toward the core of the more massive star ([Paczynski 1976](#)), it is conceivable that they fall in this category.

The determination of the degree of synchronization in post common envelope binaries would be beneficial to further improve the understanding of the ETVs. The surface magnetic field distribution would be as equally important because such nonaxisymmetric fields produce larger quadrupole moments. Furthermore, there is also unexplored grounds in the simulations, such as the impact of the centrifugal force. Numerical models, specially for fully convective stars such as those in [Käpylä \(2021\)](#), that allow more freedom on the surface and near-surface layers of stars are desired as changes in the oblateness of the star can be captured.

Acknowledgements. We thank the anonymous referee for comments that helped us improve the manuscript. F.H.N. acknowledges financial support from the DAAD (Deutscher Akademischer Austauschdienst; code 91723643) for his doctoral studies. P.J.K. acknowledges the financial support from the DFG (Deutsche Forschungsgemeinschaft) Heisenberg programme grant No. KA 4825/2-1. D.R.G.S. thanks for funding via Fondecyt regular (project code 1201280), ANID Programa de Astronomia Fondo Quimal QUIMAL170001 and the BASAL Centro de Excelencia en Astrofísica y Tecnologías Afines (CATA) grant PFB-06/2007. R.B. acknowledges support by the DFG under Germany's Excellence Strategy – EXC 2121 “Quantum Universe” – 390833306. R.B. is also thankful for funding by the DFG through the projects No. BA 3706/14-1, No. BA 3706/15-1, No. BA 3706/17-1, and No. BA 3706/18. The simulations were run on the Leftraru/Guacolda supercomputing cluster hosted by the NLHPC

(ECM-02), the Kultrun cluster hosted at the Departamento de Astronomía, Universidad de Concepción, and on HLRN-IV under project grant hhp00052.

References

- Applegate, J. H. 1989, *ApJ*, **337**, 865
 Applegate, J. H. 1992, *ApJ*, **385**, 621
 Brinkworth, C. S., Marsh, T. R., Dhillon, V. S., & Knigge, C. 2006, *MNRAS*, **365**, 287
 Brown, B. P., Oishi, J. S., Vasil, G. M., Lecoanet, D., & Burns, K. J. 2020, *ApJ*, **902**, L3
 Busse, F. H. 2002, *Phys. Fluids*, **14**, 1301
 Cole, E., Käpylä, P. J., Mantere, M. J., & Brandenburg, A. 2014, *ApJ*, **780**, L22
 Gastine, T., Yadav, R. K., Morin, J., Reiners, A., & Wicht, J. 2014, *MNRAS*, **438**, L76
 Grote, E., & Busse, F. H. 2000, *Phys. Rev. E*, **62**, 4457
 Hardy, A., Schreiber, M. R., Parsons, S. G., et al. 2015, *ApJ*, **800**, L24
 Käpylä, P. J. 2021, *A&A*, **651**, A66
 Käpylä, P. J., Korpi, M. J., Brandenburg, A., Mitra, D., & Tavakol, R. 2010, *Astron. Nachr.*, **331**, 73
 Käpylä, P. J., Mantere, M. J., Cole, E., Warnecke, J., & Brandenburg, A. 2013, *ApJ*, **778**, 41
 Käpylä, P. J., Käpylä, M. J., & Brandenburg, A. 2014, *A&A*, **570**, A43
 Klein, B., Donati, J.-F., Hébrard, É. M., et al. 2021, *MNRAS*, **500**, 1844
 Krause, F., & Rädler, K.-H. 1980, *Mean-Field Magnetohydrodynamics and Dynamo Theory* (Oxford: Pergamon Press, Ltd.)
 Lanza, A. F. 2020, *MNRAS*, **491**, 1820
 Lanza, A. F., Rodono, M., & Rosner, R. 1998, *MNRAS*, **296**, 893
 Lehtinen, J. J., Spada, F., Käpylä, M. J., Olsper, N., & Käpylä, P. J. 2020, *Nat. Astron.*, **4**, 658
 Lurie, J. C., Vyhmeister, K., Hawley, S. L., et al. 2017, *AJ*, **154**, 250
 Marchionni, L., Guinan, E. F., Engle, S. G., et al. 2018, *Res. Notes Am. Astron. Soc.*, **2**, 179
 Navarrete, F. H., Schleicher, D. R. G., Zamponi Fuentealba, J., & Völschow, M. 2018, *A&A*, **615**, A81
 Navarrete, F. H., Schleicher, D. R. G., Käpylä, P. J., et al. 2020, *MNRAS*, **491**, 1043
 Navarrete, F. H., Schleicher, D. R. G., Käpylä, P. J., et al. 2021, *MNRAS*, **504**, 1676
 Paczynski, B. 1976, in *Structure and Evolution of Close Binary Systems*, eds. P. Eggleton, S. Mitton, & J. Whelan, *IAU Symp.*, **73**, 75
 Pencil Code Collaboration (Brandenburg, A., et al.) 2021, *J. Open Sour. Softw.*, **6**, 2807
 Vaccaro, T. R., Wilson, R. E., Van Hamme, W., & Terrell, D. 2015, *ApJ*, **810**, 157
 Vanderbosch, Z. P., Clemens, J. C., Dunlap, B. H., & Winget, D. E. 2017, in *20th European White Dwarf Workshop*, eds. P. E. Tremblay, B. Gaensicke, & T. Marsh, *ASP Conf. Ser.*, **509**, 571
 Viviani, M., Warnecke, J., Käpylä, M. J., et al. 2018, *A&A*, **616**, A160
 Völschow, M., Banerjee, R., & Hessman, F. V. 2014, *A&A*, **562**, A19
 Völschow, M., Schleicher, D. R. G., Perdelwitz, V., & Banerjee, R. 2016, *A&A*, **587**, A34
 Völschow, M., Schleicher, D. R. G., Banerjee, R., & Schmitt, J. H. M. M. 2018, *A&A*, **620**, A42
 Wright, N. J., & Drake, J. J. 2016, *Nature*, **535**, 526
 Zorotovic, M., & Schreiber, M. R. 2013, *A&A*, **549**, A95

Appendix A: Scaling of the quadrupole moment with Mach number

In Navarrete et al. (2020) the scaling of the quadrupole moment was assumed to be

$$Q_{xx,\text{phys}} \propto \mathcal{L}_r^{-2/3} Q_{xx,\text{code}}, \quad (\text{A.1})$$

where $Q_{xx,\text{phys}}$ is the physical quadrupole moment, and \mathcal{L}_r^3 is the ratio of simulation to solar luminosities at the bottom of the CZ, and $Q_{xx,\text{code}}$ is the quadrupole moment in code units. Equivalently,

$$Q_{xx,\text{phys}} \propto \text{Ma}^2 Q_{xx,\text{code}}, \quad (\text{A.2})$$

where Ma is the Mach number. We test this scaling with two sets of simulations. Set L uses the same parameters as in Run B but we omit magnetic fields and rotation. Set M includes both rotation and magnetic fields. In particular, Run L2 has the same input parameters as Run B such as \mathcal{L}_r , but without rotation and magnetic fields. Relevant quantities are shown in Table 1. Run L2 produces a maximum variation of the quadrupole moment $\Delta Q_{xx} = 6.8 \times 10^{38} \text{ kg m}^2$, which is about 18 times smaller than in Run B. These variations develop on a timescale of 5 years and remain below the aforementioned level after that.

The rms value of the quadrupole moment fluctuations as a function of Mach number is shown in Fig. A.1 for Set L and in Fig. A.2 for Set M. The results are in reasonable agreement with the theoretical scaling, which is indicated by the dotted line in each plot.

Table A.1. Parameters of sets L and M.

Run	\mathfrak{F}_r	Ma	$\Delta Q_{xx}^{\text{rms}}$
L1	2.74×10^5	5.67×10^{-2}	1.07×10^{-5}
L2	8.07×10^5	7.97×10^{-2}	2.85×10^{-5}
L3	2.34×10^6	1.11×10^{-1}	6.87×10^{-5}
M1	2.12×10^5	9.60×10^{-2}	3.44×10^{-5}
M2	6.37×10^5	1.25×10^{-1}	5.60×10^{-5}
M3	2.12×10^6	1.42×10^{-1}	9.30×10^{-5}

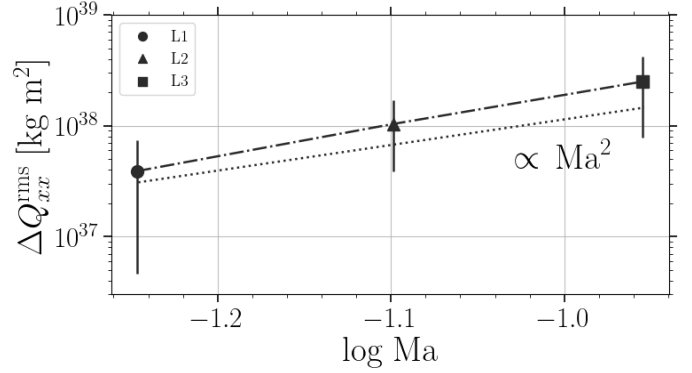


Fig. A.1. Root-mean-squared quadrupole moment fluctuations as a function of Mach number for Set L (without rotation and magnetic fields). The dotted line is proportional to the Mach number squared and the dash-dotted line joins the data points.

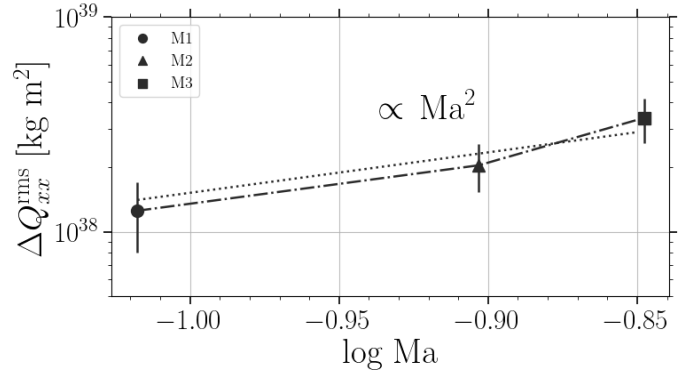


Fig. A.2. Root-mean-squared quadrupole moment fluctuations as a function of Mach number for Set M (with rotation and magnetic fields). The dotted line is proportional to the Mach number squared and the dash-dotted line joins the data points.

³ \mathcal{L}_r corresponds to \mathfrak{F}_r of Navarrete et al. (2020).

Appendix B: Figures of the decomposed fields

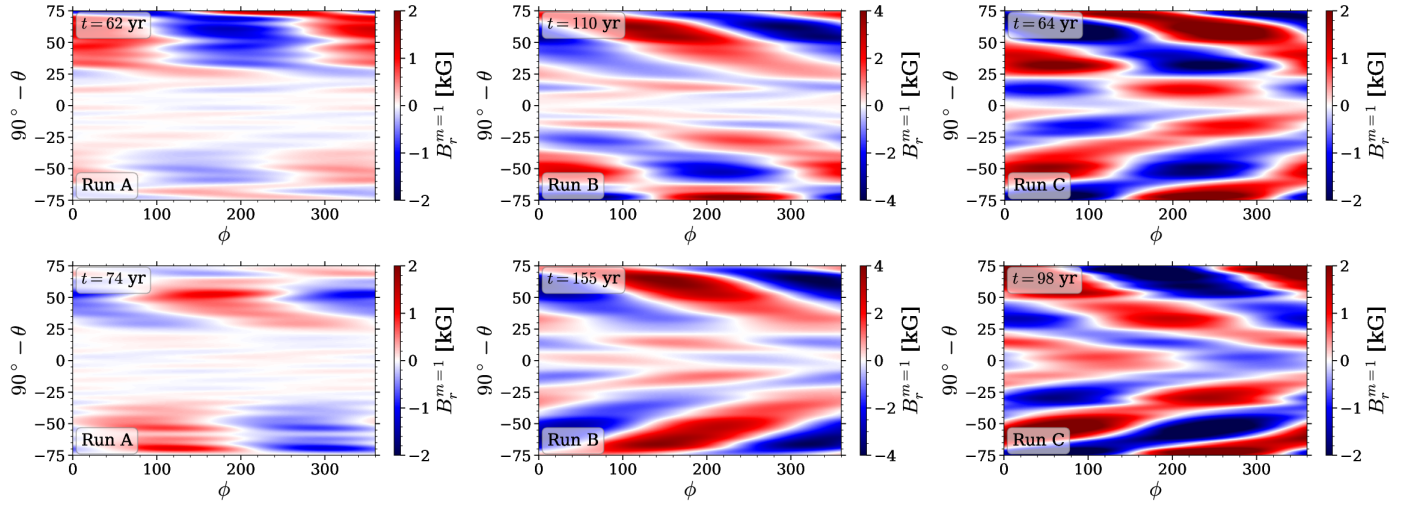


Fig. B.1. First nonaxisymmetric mode of the radial magnetic field ($B_r^{m=1}$) at $r = 0.98R$ for each run.

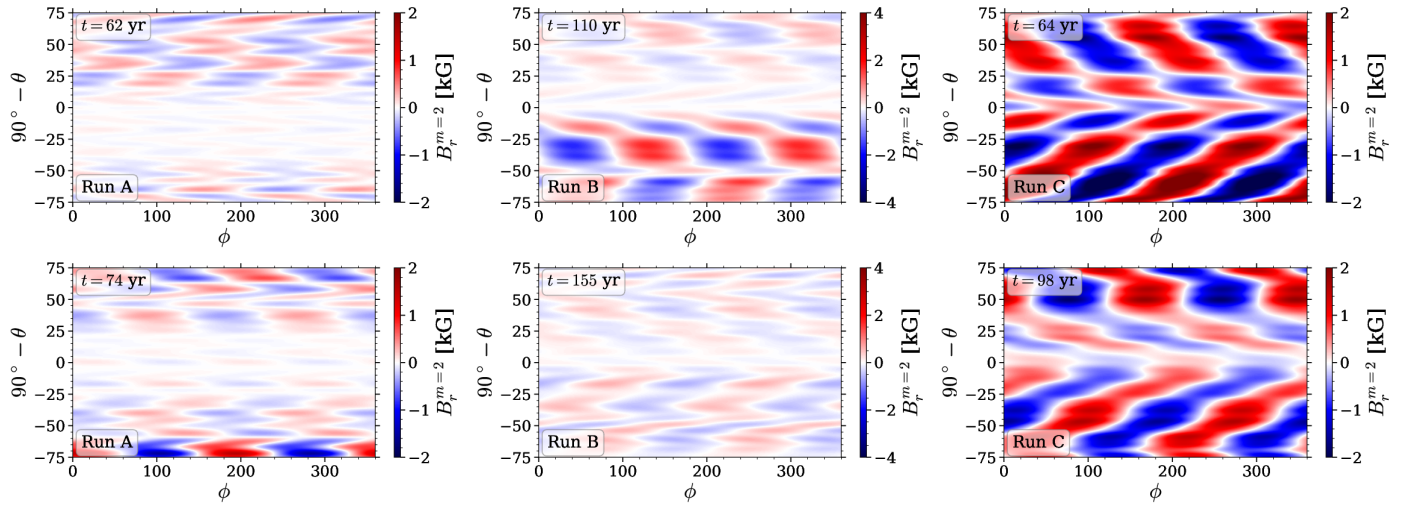


Fig. B.2. Second nonaxisymmetric mode of the radial magnetic field ($B_r^{m=2}$) at $r = 0.98R$ for each run.

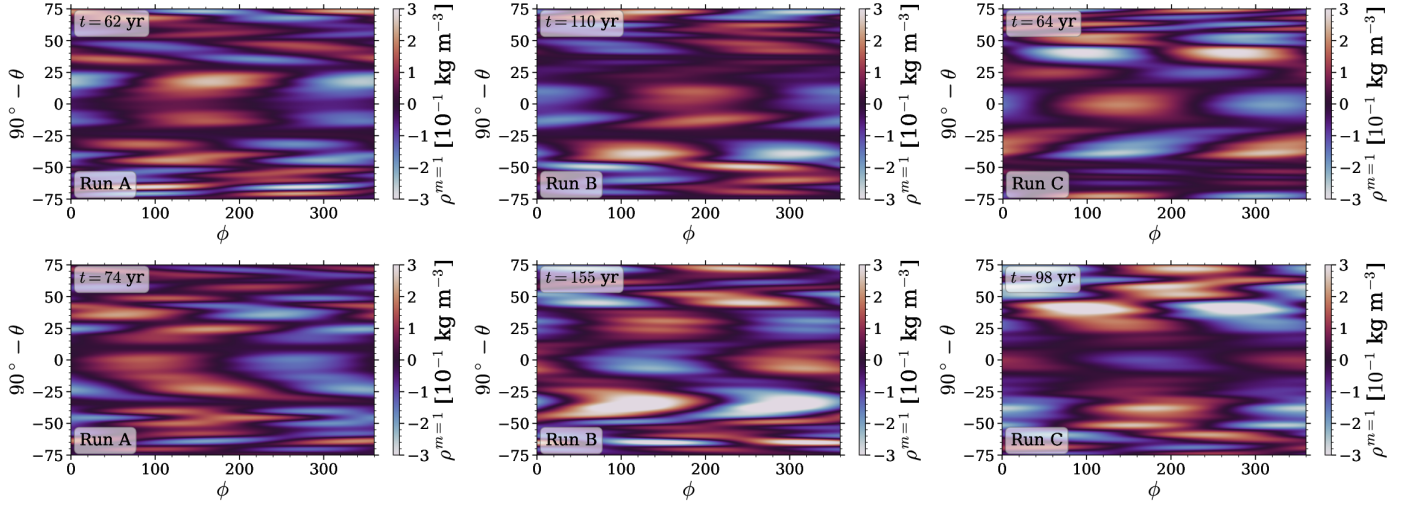


Fig. B.3. First nonaxisymmetric mode of density at $r = 0.98R$ for each Run.

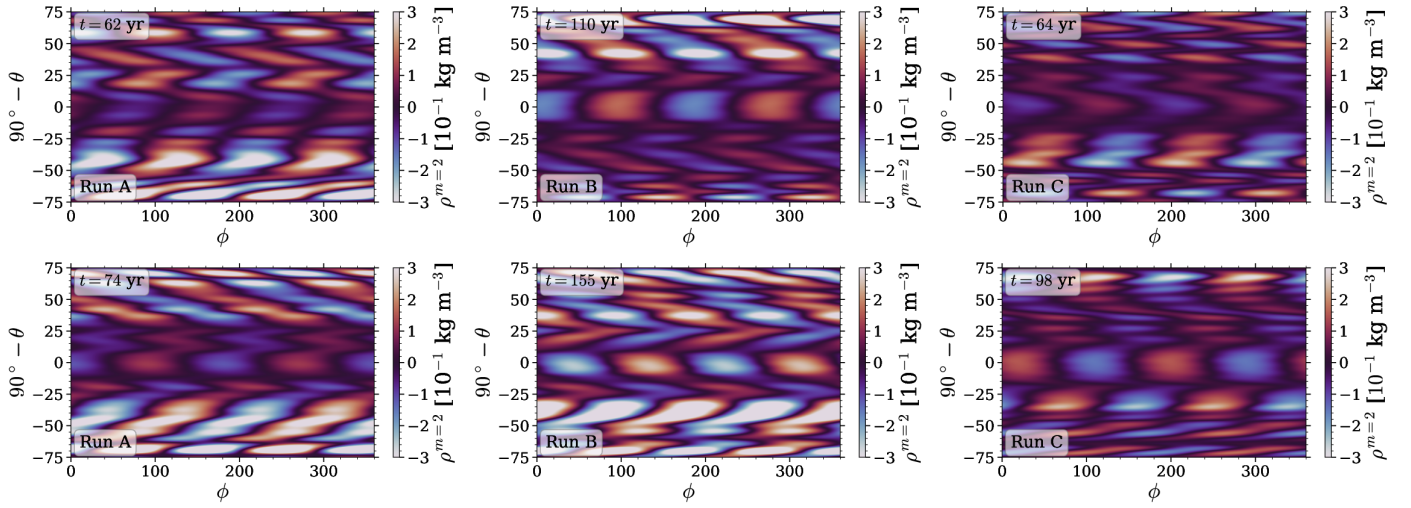


Fig. B.4. Second nonaxisymmetric mode of density at $r = 0.98R$ for each Run.





Chapter 4

Paper II

Contribution

To understand the effects of the centrifugal force, I planned and applied for computing time for the simulations presented below. The data was analyzed by myself and I also prepared the manuscript.

Origin of eclipsing time variations in post-common-envelope binaries: Role of the centrifugal force

Felipe H. Navarrete^{1,2} , Dominik R. G. Schleicher³ , Petri J. Käpylä^{4,2} ,
Carolina A. Ortiz-Rodríguez³ , and Robi Banerjee¹

¹ Hamburger Sternwarte, Universität Hamburg, Gojenbergsweg 112, 21029 Hamburg, Germany
e-mail: felipe.navarrete@hs.uni-hamburg.de

² Nordita, Stockholm University and KTH Royal Institute of Technology, Hannes Alfvéns väg 12, 106 91 Stockholm, Sweden

³ Departamento de Astronomía, Facultad Ciencias Físicas y Matemáticas, Universidad de Concepción, Av. Esteban Iturra s/n Barrio Universitario, Casilla 160-C, Concepción, Chile

⁴ Institut für Astrophysik und Geophysik, Georg-August-Universität Göttingen, Friedrich-Hund-Platz 1, 37077 Göttingen, Germany

Received 1 May 2022 / Accepted 8 September 2022

ABSTRACT

Eclipsing time variations in post-common-envelope binaries were proposed to be due to the time-varying component of the stellar gravitational quadrupole moment. This is suggested to be produced by changes in the stellar structure due to an internal redistribution of angular momentum and the effect of the centrifugal force. We examined this hypothesis and present 3D simulations of compressible magnetohydrodynamics performed with the PENCIL CODE. We modeled the stellar dynamo for a solar-mass star with angular velocities of 20 and 30 times solar. We included and varied the strength of the centrifugal force and compared the results with reference simulations without the centrifugal force and with a simulation in which its effect is enhanced. The centrifugal force causes perturbations in the evolution of the numerical model, so that the outcome in the details becomes different as a result of nonlinear evolution. While the average density profile is unaffected by the centrifugal force, a relative change in the density difference between high latitudes and the equator of $\sim 10^{-4}$ is found. The power spectrum of the convective velocity is found to be more sensitive to the angular velocity than to the strength of the centrifugal force. The quadrupole moment of the stars includes a fluctuating and a time-independent component, which vary with the rotation rate. As very similar behavior is produced in absence of the centrifugal force, we conclude that it is not the main ingredient for producing the time-averaged and fluctuating quadrupole moment of the star. In a real physical system, we thus expect contributions from both components, that is, from the time-dependent gravitational force from the variation in the quadrupole term and from the spin-orbit coupling that is due to the persistent part of the quadrupole.

Key words. magnetohydrodynamics (MHD) – dynamo – methods: numerical – binaries: eclipsing

1. Introduction

Eclipsing time variations (ETVs) have been observed in a wide range of post-common-envelope binaries (PCEBs; Zorotovic & Schreiber 2013; Bours et al. 2016). Traditionally, two explanations have been proposed for the observed variations: One explanation refers to the possible presence of a third body, preferentially with a mass of a few Jupiter masses in the case of NN Ser (Beuermann et al. 2010) and a brown dwarf of $0.035 M_{\odot}$ in V471 Tau (Vaccaro et al. 2015), and on a wide orbit, which could explain the observed ETVs as due to the orbit of the binary system around the common center of mass via the light travel time effect (e.g., Beuermann et al. 2012, 2013). The presence of such planets might be explained either because they survived the common-envelope event (Völschow et al. 2014) or because they formed from the ejecta of common-envelope material (Schleicher & Dreizler 2014). However, the planetary systems were sometimes found to be unstable (Mustill et al. 2013), and at other times, the predicted planets were not detected (Hardy et al. 2015).

An alternative possibility is that the ETVs is caused in the binary system itself, as a result of magnetic activity. This might occur in different forms. An early suggestion by Decamp & Baliunas (1979) considered a rocket effect pro-

duced by anisotropic mass loss, but the hypothesis was finally rejected. Tidal torques are another possibility, but their magnitudes are so low (Zahn & Bouchet 1989; Ogilvie & Lin 2007) that they cannot transfer the necessary angular momentum (Applegate & Patterson 1987). As a different solution, both Matese & Whitmire (1983) and Applegate & Patterson (1987) proposed that the orbital period would be changed if the stellar quadrupole moment changed as a result of magnetic activity.

This was a central step, but the cause for the change in the stellar quadrupole moment remains to be defined and its strength needs to be determined. In the original models (e.g., Matese & Whitmire 1983; Applegate & Patterson 1987), it was assumed that the magnetic field deforms the star by causing a deviation from its hydrostatic equilibrium, requiring thus a very strong magnetic field. Marsh & Pringle (1990) showed, however, that the required periodic deformation was too strong to be sustained by the luminosity of the star. A different scenario thus emerged in which the change of the quadrupole moment is not caused directly by the magnetic field, but is a result of angular momentum redistribution inside the star through the dynamo process, which then leads to stellar distortions as a result of the centrifugal force (Applegate 1992). Within a simplified thin-shell model, considering an inner core and an infinitely thin shell, Applegate (1992) calculated the quadrupole moment of the

shell as

$$Q = \frac{1}{9} M_s R^2 \left(\frac{\Omega^2 R^3}{GM} \right), \quad (1)$$

where M is the mass of the star, $M_s \ll M$ is the mass of the shell, Ω is the angular velocity of the shell, R is the radius from the center of the star to the shell, and G is the gravitational constant. Applegate (1992) calculated the angular momentum to be transferred within the star to produce a period variation ΔP as

$$\Delta J = -\frac{GM^2}{R} \left(\frac{a}{R} \right)^2 \frac{\Delta P}{6\pi}, \quad (2)$$

with a the separation of the binary system. The energy required to transfer the angular momentum is then

$$\Delta E = \Omega_{dr} \Delta J + \frac{(\Delta J)^2}{2I_{\text{eff}}}, \quad (3)$$

where Ω_{dr} refers to the difference of angular velocity between the shell and the core, and I_{eff} is the effective moment of inertia, corresponding to about half of the inertial moment of the shell.

This model was extended by Brinkworth et al. (2006), who considered a finite instead of an infinitely thin shell, showing that the latter increased the energy required to produce the deformation by roughly one order of magnitude. Völschow et al. (2016) subsequently applied this model in a systematic way to the sample of Zorotovic & Schreiber (2013), showing that the energy requirement is sometimes fulfilled and sometimes it is not. A similar conclusion was obtained by Navarrete et al. (2018) through an extension of the analysis. On the other hand, more detailed 1D models solving the evolution equation for the stellar angular momentum indicated that the energetic requirement may actually be reduced (Lanza 2006), and Völschow et al. (2018) concluded that the mechanism is feasible for stars with masses of 0.3–0.36 M_\odot .

Other types of solutions have also been proposed. For instance, Applegate (1989) derived librating and circulating solutions in the presence of a constant quadrupole moment, although they were originally predicted to provide modulations over shorter periods than observed in the PCEBs. Lanza (2020) re-examined this scenario, however, and proposed that a persistent nonaxisymmetric internal magnetic field could produce an appropriate quadrupole moment to explain the observed deviations at a much lower energetic expense than in the scenario in which the quadrupole moment variation is produced via the centrifugal force (e.g., Applegate 1992).

This problem was recently revisited in 3D magnetohydrodynamical (MHD) simulations, and although the centrifugal force was not included, quasi-periodic quadrupole moment variations caused by magnetic activity were found. They were roughly still one order of magnitude lower than required by observations, however (Navarrete et al. 2020). As they were not driven via the centrifugal force, it seems more likely that a change in the internal circulation in the star rather than a redistribution of the angular momentum has caused this result. This was recently confirmed via an extended set of simulations with a more detailed analysis (Navarrete et al. 2022).

As the correct mechanism that gives rise to the ETVs is still not established, it is fundamental to investigate how the centrifugal force influences the change in the quadrupole moment within the stars. For this purpose, we present 3D MHD simulations of a solar-mass star that include and vary the centrifugal force to assess in this way how it affects the stellar structure. Thus, we

aim to verify whether the origin of these variations is based on the centrifugal force as proposed by Applegate (1992), or if other mechanisms must be at play to cause the observed variations. Our numerical approach is presented in Sect. 2, and the results are given in Sect. 3. We finally present our discussion and conclusions in Sect. 4.

2. Model

We present two sets of simulations with rotation rates $20\Omega_\odot$ and $30\Omega_\odot$, where Ω_\odot is the solar rotation rate. These are part of an overall larger set of simulations that has been pursued to analyze dynamos in the context of young stars (Navarrete et al., in prep.). We label the first set simulation group C and the second set group D. Within each set, we varied the centrifugal force amplitude.

The compressible MHD equations were solved on a spherical grid with coordinates (r, θ, ϕ) , where $0.7 \leq r \leq R$ is the radial coordinate, R is the radius of the star, $\pi/12 \leq \theta \leq 11\pi/12$ is the colatitude, and $0 \leq \phi < 2\pi$ is the longitude. The model is the same as in Käpylä et al. (2013) and Navarrete et al. (2020, 2022). The equations were solved in the following form:

$$\frac{\partial \mathbf{A}}{\partial t} = \mathbf{u} \times \mathbf{B} - \eta \mu_0 \mathbf{J}, \quad (4)$$

$$\frac{D \ln \rho}{Dt} = -\nabla \cdot \mathbf{u}, \quad (5)$$

$$\frac{D\mathbf{u}}{Dt} = \mathcal{F}^{\text{grav}} + \mathcal{F}^{\text{Cor}} + \mathcal{F}^{\text{cent}} - \frac{1}{\rho} (\nabla p - \mathbf{J} \times \mathbf{B} - \nabla \cdot 2\nu \rho \mathbf{S}), \quad (6)$$

$$T \frac{Ds}{Dt} = \frac{1}{\rho} \left[\eta \mu_0 \mathbf{J}^2 - \nabla \cdot (\mathbf{F}^{\text{rad}} + \mathbf{F}^{\text{SGS}}) \right] + 2\nu S^2, \quad (7)$$

where \mathbf{A} is the magnetic vector potential, $\mathbf{B} = \nabla \times \mathbf{A}$ is the magnetic field, \mathbf{u} is the velocity field, η is the magnetic diffusivity, μ_0 is the vacuum permittivity, \mathbf{J} is the current density, ρ is the density, p is the pressure, ν is the viscosity, \mathbf{S} is the rate of strain tensor, T is the temperature, and s is the entropy. \mathbf{F}^{rad} and \mathbf{F}^{SGS} are the radiative and the subgrid scale fluxes, respectively (see, e.g., Käpylä et al. 2013). The SGS flux is given by

$$\mathbf{F}^{\text{SGS}} = -\chi_{\text{SGS}} \rho T \nabla s, \quad (8)$$

where $\chi_{\text{SGS}} = \chi_{\text{SGS}}^{\text{m}} = 0.4\nu$ at $0.75 < r/R < 0.98$ and increases smoothly to $12.5\chi_{\text{SGS}}^{\text{m}}$ above $r = 0.98R$. Below $r = 0.75R$, it decreases smoothly and approaches zero. This term is a parameterization of the unresolved turbulent heat transport. The SGS diffusivity is needed because the radiative diffusivity $\chi = K/c_p \rho$, where K is the heat conductivity and c_p is the specific heat at constant pressure, is insufficient to smooth grid-scale fluctuations even with the enhanced luminosity of the current simulations. Furthermore,

$$\mathcal{F}^{\text{grav}} = -(GM/r^2) \hat{\mathbf{r}}, \quad (9)$$

$$\mathcal{F}^{\text{Cor}} = -2\boldsymbol{\Omega}_0 \times \mathbf{u}, \quad (10)$$

$$\mathcal{F}^{\text{cent}} = -c_f \boldsymbol{\Omega}_0 \times (\boldsymbol{\Omega}_0 \times \mathbf{r}) \quad (11)$$

are the gravitational, Coriolis, and centrifugal forces. Here, $\boldsymbol{\Omega}_0$ is the rotation rate of the modeled star. The parameter c_f was introduced by Käpylä et al. (2020) and controls the strength of the centrifugal force. $c_f = 1$ corresponds to the unaltered centrifugal force amplitude, and $c_f = 0$ implies no centrifugal force. It is defined as

$$c_f = \frac{|\mathcal{F}^{\text{cent}}|}{|\mathcal{F}_0^{\text{cent}}|}, \quad (12)$$

with $|\mathcal{F}_0^{\text{cent}}|$ being the physically consistent magnitude of the centrifugal force. The need to control the centrifugal force arises due to the enhanced luminosity and rotation rate in simulations of stellar (magneto-) convection. This approach is necessary to avoid a too large gap between acoustic, convective, and thermal relaxation timescales in simulations that solve the compressible MHD equations (e.g., Brandenburg et al. 2005; Käpylä et al. 2013). Using the realistic stellar luminosity would have the consequence that flow velocities would be much lower than the sound speed. The time step would then become prohibitively short and the thermal relaxation (Kelvin-Helmholtz) time prohibitively long (see Käpylä et al. 2020, for the effects of varying luminosity on the flow properties). The enhancement of the luminosity is described by

$$\mathcal{L}_r = \frac{\mathcal{L}_{\text{sim}}}{\mathcal{L}_*}, \quad (13)$$

where \mathcal{L}_{sim} is the luminosity in our model and \mathcal{L}_* is the luminosity of the target, the physical star. We have $\mathcal{L}_r = 8.07 \times 10^5$ for the setup adopted here for a solar-like target star (Navarrete et al. 2020). The angular velocity has to be enhanced correspondingly to produce a realistic Coriolis number. For the centrifugal force, on the other hand, the strength should be limited so that the impact on the structure of the star is not overestimated. For numerical stability and as outlined by Käpylä et al. (2020), each run was initialized with $c_f = 0$, and it was increased in small incremental steps after the saturated regime was reached. In this way, the effect of the centrifugal force can be explored in the simulation.

To quantify the strength of the centrifugal force, we computed the ratio of gravitational to centrifugal forces in the simulations presented here as well as for a real Sun-like star with the same rotation rate. The ratio of the two is defined as

$$\mathcal{F} = \frac{(|\mathcal{F}^{\text{cent}}|/|\mathcal{F}^{\text{grav}}|)_{\text{sim}}}{(|\mathcal{F}^{\text{cent}}|/|\mathcal{F}^{\text{grav}}|)_*}, \quad (14)$$

where the subscript asterisk denotes the real star and *sim* the simulations. If this ratio is equal to unity, the relative strength of the centrifugal force with respect to gravity is the same in the simulation as in the real star. Particularly for rapidly rotating stars, it is in principle harder to model a case with $\mathcal{F} = 1$, and we typically remain somewhat below this ratio, but we also present a case with $\mathcal{F} > 1$ for comparison.

The details of the model are further described in Navarrete et al. (2020, 2022) and in Käpylä et al. (2013), and we refer to these papers to avoid repetition. We nonetheless recall that the model assumes an outer spherical boundary at the stellar radius that is assumed to be impenetrable and stress-free. At the lower boundary at 70% of the stellar radius, the magnetic field is assumed to obey a perfect conductor boundary condition, while at the top boundary, the field is assumed to be radial. The temperature gradient is fixed at the bottom, while a blackbody condition is applied at the surface. The setup includes colatitudinal boundaries at 15° and 165° , which are assumed to be stress-free and perfectly conducting. Density and entropy are assumed to have zero first derivatives on colatitudinal boundaries. The gravitational potential is spherically symmetric and independent of time, and self-gravity is not taken into account. The equations are solved with the PENCIL CODE¹, a high-order finite-difference code for compressible MHD equations (Pencil Code Collaboration 2021).

¹ <https://github.com/pencil-code/pencil-code>

We define the Coriolis, Taylor, Reynolds, magnetic Reynolds, Prandtl, magnetic Prandtl, SGS Prandtl, and Péclet numbers as

$$\text{Co} = \frac{2\Omega_0}{u_{\text{rms}}k_1}, \quad \text{Ta} = \left[\frac{2\Omega_0(0.3R)^2}{\nu} \right]^2, \quad \text{Re} = \frac{u_{\text{rms}}}{\nu k_1}, \quad (15)$$

$$\text{Re}_M = \frac{u_{\text{rms}}}{\eta k_1}, \quad \text{Pr} = \frac{\nu}{\chi_m}, \quad \text{Pr}_M = \frac{\nu}{\eta}, \quad \text{Pr}_{\text{SGS}} = \frac{\nu}{\chi_{\text{SGS}}^m}, \quad (16)$$

$$\text{Pe} = \frac{u_{\text{rms}}}{\chi_{\text{SGS}}^m k_1}, \quad (17)$$

where u_{rms} is the root-mean-square velocity, $k_1 = 2\pi/0.3R$ is an estimate of the wavenumber of the largest convective eddies, and $\chi_{\text{SGS}}^m = 0.4\nu$ is the subgrid-scale entropy diffusion in the middle of the convective region. Each run is characterized by $\text{Pr} = 60$, $\text{Pr}_M = 1$, and $\text{Pr}_{\text{SGS}} = 2.5$. The other quantities are shown in Table 1. Throughout this paper, overbars denote averages over longitude.

3. Results

We present the results of two sets of three simulations each. Set C is characterized by a rotation rate of $20\Omega_\odot$ and set D by $30\Omega_\odot$. Runs C1 and D1 correspond to the parent runs without centrifugal force from which C2 and C3, and D2 and D3 were forked, respectively. The last four runs were initialized with the centrifugal force. For runs C2 and C3, we considered $\mathcal{F} = 0.875$, but they were initialized from C1 at different times. This was done to test whether the initial magnetic state of the parent run alters the solution of the forked run. Runs D2 and D3 have $\mathcal{F} = 0.875$ and 8.75 , respectively. This last run is considered as an extreme case where we exaggerated the effect of the centrifugal force to show the corresponding implications. Each simulation had a resolution of $144 \times 288 \times 576$ grid points in (r, θ, ϕ) .

3.1. Dynamical state in the simulations

In our simulations, the azimuthally averaged density profile at the equatorial plane of the star is basically unaffected by the centrifugal force; the only change we see occurs at high latitudes. We focus here on relative density differences between the region 60° above the equator and the density profile at the equator, which we define via

$$\bar{\rho}_{\text{diff}} = \frac{\bar{\rho}(90^\circ - \theta = 60^\circ) - \bar{\rho}(90^\circ - \theta = 0^\circ)}{\langle \bar{\rho} \rangle_{r\theta}}, \quad (18)$$

where $\langle \bar{\rho} \rangle_{r\theta}$ is the volume-averaged density. In the context of the enhanced luminosity method, we recall that density differences scale as (Brandenburg et al. 2005; Käpylä et al. 2013; Navarrete et al. 2020)

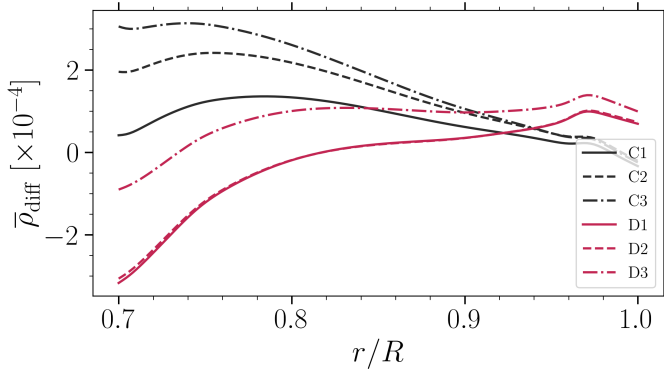
$$\bar{\rho}_{\text{diff}} \propto \mathcal{L}_r^{2/3}. \quad (19)$$

This implies that we should multiply with a factor $\mathcal{L}_r^{-2/3}$ to obtain the expected density difference in a physical star. We calculated these density differences and averaged them over the last 80 yr of the simulation. They are shown in Fig. 1 as a function of radius. These differences are more relevant in the interior of the star, at 70–80% of the stellar radius, where they have a typical magnitude of about 10^{-4} . These density variations show clear trends with the centrifugal force, which tends to increase the density difference between higher latitudes and equator toward positive values. There are marked differences

Table 1. Summary of the dimensionless parameters that characterize the simulations.

Run	Ω/Ω_\odot	c_f	Co	Ta	Re	Re_M	Pe	\mathcal{F}	$\langle \Delta_\Omega^{(r)} \rangle_t$	$\langle \Delta_\Omega^{(60^\circ)} \rangle_t$	$\Delta_{\Omega,\text{rms}}^{(r)}$	$\Delta_{\Omega,\text{rms}}^{(60^\circ)}$
C1	20	0	57.2	2.53(9)	22.1	22.1	55.3	0	9.16(-4)	3.42(-3)	4.26(-4)	5.02(-4)
C2	20	1.0(-4)	55.6	2.53(9)	22.8	22.8	57.0	8.75(-1)	9.27(-4)	3.60(-3)	4.62(-4)	5.30(-4)
C3	20	1.0(-4)	56.7	2.53(9)	22.3	22.3	55.8	8.75(-1)	8.40(-4)	3.66(-3)	6.23(-4)	6.28(-4)
D1	30	0	137.9	5.72(9)	13.8	13.8	34.6	0	-2.51(-4)	4.51(-4)	8.05(-5)	1.23(-4)
D2	30	1.0(-4)	137.8	5.72(9)	13.8	13.8	34.8	8.75(-1)	-2.42(-4)	4.75(-4)	1.15(-4)	1.54(-4)
D3	30	1.0(-3)	130.1	5.72(9)	14.6	14.6	36.6	8.75	-6.34(-5)	8.70(-4)	1.52(-4)	2.39(-4)

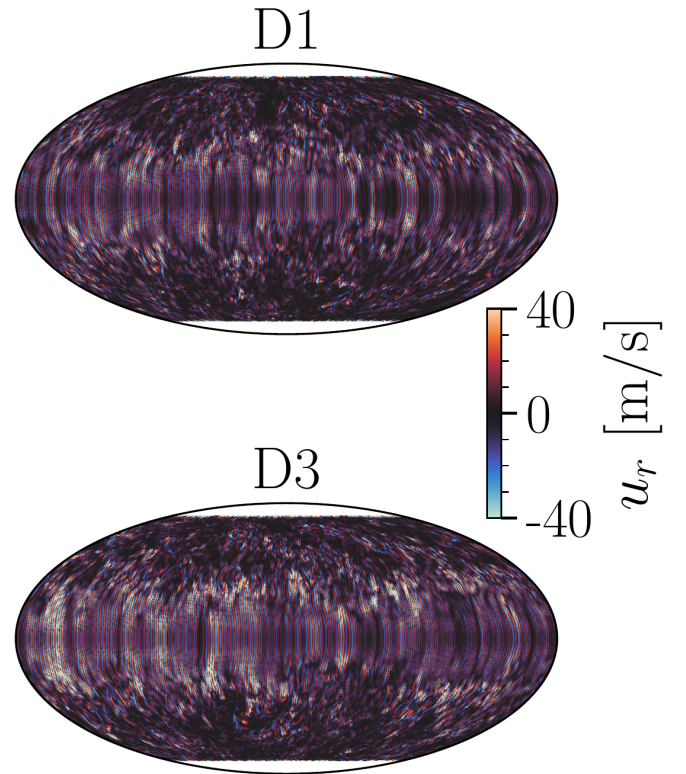
Notes. Co is the Coriolis number, Ta is the Taylor number, Re and Re_M are the fluid and magnetic Reynolds numbers, and Pe is the Péclet number. For each run, $\text{Pr} = 60$, $\text{Pr}_M = 1$, and $\text{Pr}_{\text{SGS}} = 2.5$. $\Delta_\Omega^{(r),(60^\circ)}$ denote the radial and latitudinal differential rotation and are defined in Eqs. (21) and (22), respectively. $\langle \dots \rangle_t$ denotes averages over time, and the prime denotes fluctuating quantities.


Fig. 1. Density difference between regions at 60° above the equator and the equator.

between runs C1 and C2, but not between runs D1 and D2. A possible explanation for this might be the different dynamo solutions. In general, runs in set C show dynamos that tend to alternate between the two hemispheres. This produces an asymmetry on the density field with respect to the equator. In this case, $\bar{\rho}_{\text{diff}}$ increases when the magnetic field is more concentrated in one hemisphere. This is the case for runs C1 and C2. The difference comes from the location of the magnetic field structure, which reduces the local density. This is not the case for runs D1 and D2, however, and so the density profiles are the same. A similar explanation can be given for run D3.

Snapshots of the final state of the radial (convective) velocity near the surface of the star are given in Fig. 2 for simulations D1 and D3, which are also representative of the other runs within our set of simulations. The series of runs C and D correspond to fast rotators, and the convective cells are therefore very small toward medium to high latitudes, whereas they become elongated near the equator. This is a common phenomenon obtained in simulations of stellar convection (see, e.g., Viviani et al. 2018) and is consistent with the Taylor-Proudman balance. The result for D3 is very similar as for D1, but it is not identical. While both runs were evolved until the same time, an identical result is not expected because the dynamics are nonlinear and because the centrifugal force causes perturbations within the star. On the other hand, and even though in principle the strength of the centrifugal force is quite significant in run D3, the impact on the flow pattern appears to be relatively minor.

Similar projections, now for the radial component of the magnetic field, are presented in Fig. 3. In run D1, clear non-axisymmetric structures are present that extend throughout each hemisphere. Nonaxisymmetric structures seem to be somewhat


Fig. 2. Mollweide projections of radial velocity near the surface for runs D1 and D3.

smaller in run D3, that is, an $m = 2$ mode is also present. The amplitude of B_r remains very similar.

We decomposed the radial velocity field at the surface of selected runs into spherical harmonics and calculated the normalized convective power spectra as

$$P_{\text{kin}} = \frac{E_{\text{kin},l}}{\sum_l E_{\text{kin},l}}, \quad (20)$$

where $E_{\text{kin},l}$ is the kinetic energy of the l th degree. This is shown in Fig. 4, where we plot P as a function of l up to $l_{\text{max}} = 288$. This is the maximum resolution we can achieve because we used 576 grid points along the ϕ direction. The convective power peak is shifted toward higher l for higher rotation rates, but the centrifugal force has no significant influence on it, even in the extreme case of run D3. We note that the contribution of the polar caps, which are not part of the computational domain, are not included in the spherical harmonic decomposition or in the power spectra.

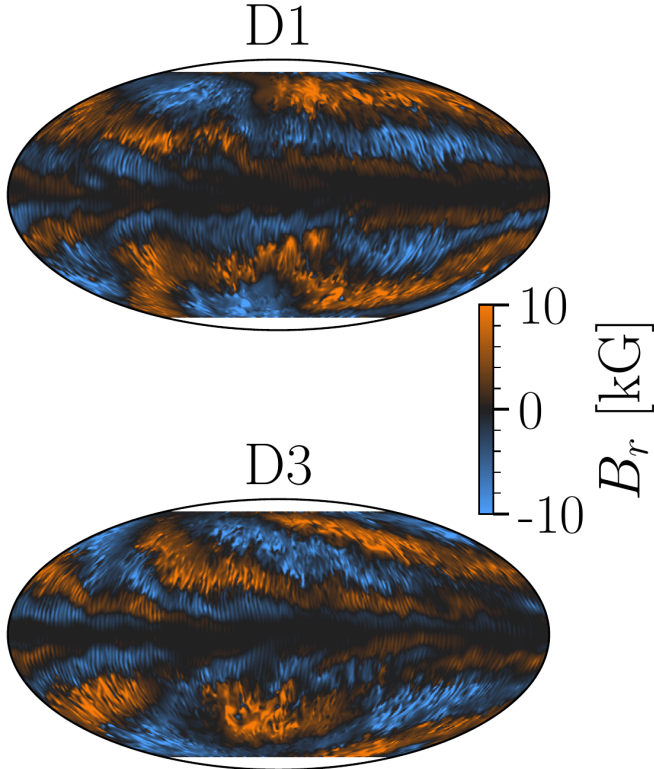


Fig. 3. Mollweide projections of radial magnetic field near the surface for runs D1 and D3.

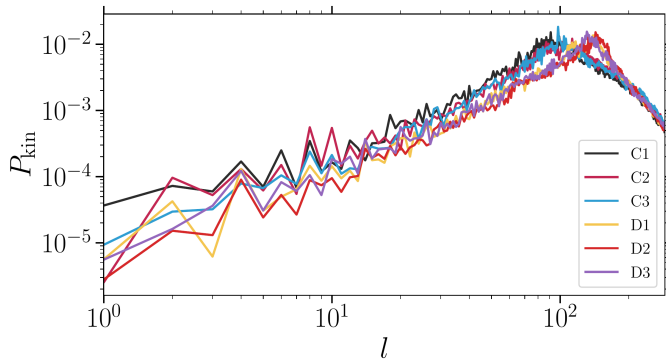


Fig. 4. Normalized convective power spectra for runs C1, C2, C3, D1, D2, and D3.

In Fig. 5 we show the time-averaged and azimuthally averaged angular velocity normalized with the angular velocity of the rotating frame for simulations with different rotation rates and with and without the centrifugal force. In set D, where the angular velocity is higher in general, we find that stellar differential rotation is reduced compared with set C, which is expected for more rapidly rotating runs (e.g., Kitchatinov & Rüdiger 1995; Viviani et al. 2018). Measures of the radial and latitudinal differential rotation are shown in Table 1. They are defined as

$$\Delta_{\Omega}^{(r)} = \frac{\Omega_{\text{eq}} - \Omega_{\text{bot}}}{\Omega_{\text{eq}}}, \quad (21)$$

$$\Delta_{\Omega}^{(60^\circ)} = \frac{\Omega_{\text{eq}} - \Omega_{60^\circ}}{\Omega_{\text{eq}}}, \quad (22)$$

respectively. Here, Ω_{eq} , Ω_{bot} , and Ω_{60° are the angular velocities at the equator near the surface, at the equator near the bot-

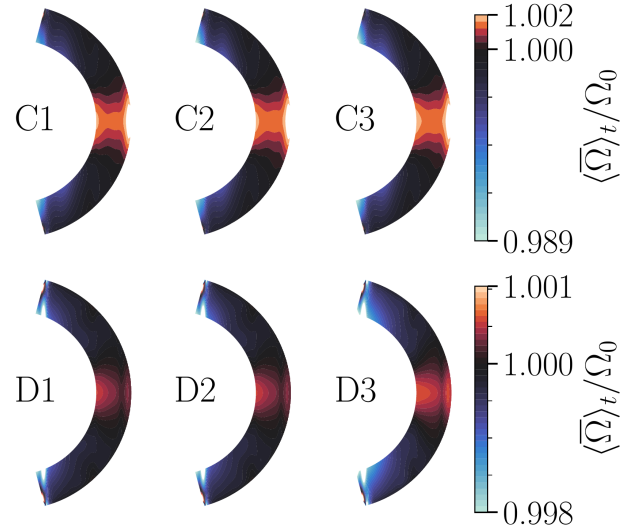


Fig. 5. Mean rotation rate averaged over the last 80 yr of the simulation and normalized to the rotation rate of the star. $\langle \dots \rangle_t$ denotes the average over time.

tom of the convective zone, and near the surface at a latitude of 60° , respectively. The time-averaged radial differential rotation remains practically the same within each set. The time-averaged radial and latitudinal differential rotation only changes appreciably in run D3 by a factor of four and two, respectively, where we enhanced the centrifugal force. We fail to find strong evidence for a direct effect of the centrifugal force from the time averages, however. We also show the rms values of the fluctuations (instantaneous minus average) of $\Delta_{\Omega}^{(r)}$ and $\Delta_{\Omega}^{(60^\circ)}$ in the last two columns of Table 1. In general, there is a tendency of increased fluctuations when the centrifugal force is included and when its amplitude is larger.

Observations of the rapidly rotating K2 dwarf V471 Tau, which is a PCEB rotating at about 50 times faster than the Sun, show that it has a solar-like differential rotation (Zaire et al. 2022). The surface differential rotation is about $\Delta_{\Omega}^{(60^\circ)} = 3.7 \times 10^{-3}$, as measured from the shearing of brightness inhomogeneities (Stokes I), and $\Delta_{\Omega}^{(60^\circ)} = 2.6 \times 10^{-3}$ from magnetic structures (Stokes V). The sign of the differential rotation agrees with our simulations, and the amplitude here is about ten times smaller. We note, however, that in some cases, the instantaneous value of $\Delta_{\Omega}^{(60^\circ)}$ can be as high as 10^{-3} .

3.2. Gravitational quadrupole moment

We analyzed the xx -component of the gravitational quadrupole moment for runs C1, C2, and C3 and for runs D1, D2, and D3. It is defined as

$$Q_{ij} = I_{ij} - \frac{1}{3} \delta_{ij} \text{Tr} I, \quad (23)$$

where

$$I_{ij} = \int \rho(\mathbf{x}) x_i x_j dV \quad (24)$$

is the inertia tensor, with ρ being the density, and x_i , x_j are Cartesian coordinates. The time evolution of Q_{xx} for all runs is shown in Fig. 6. Their yy - and zz -components evolve very similarly, as demonstrated in Navarrete et al. (2020). The average quadrupole

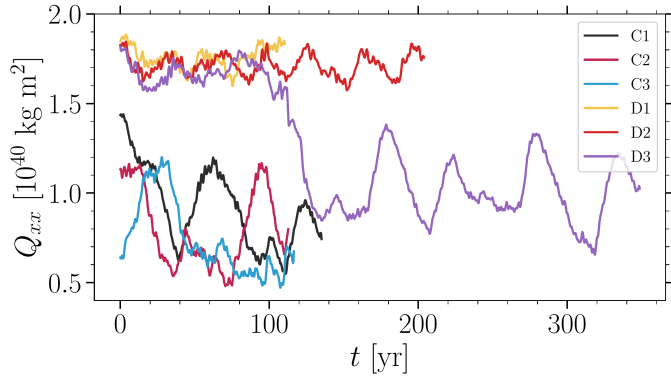


Fig. 6. Q_{xx} component of the gravitational quadrupole moment as a function of time for all runs.

Table 2. Summary of the rms value and standard deviation of the quadrupole moment obtained in the simulations.

Run	rms [kg m ²]	σ [kg m ²]
C1	9.44(39)	2.19(39)
C2	8.25(39)	2.14(39)
C3	7.70(39)	2.08(39)
D1	1.76(40)	6.38(38)
D2	1.71(40)	5.94(38)
D3	1.02(40)	1.66(39)

Notes. Parentheses indicate powers of ten.

moment and its standard deviation are summarized in Table 2 for each simulation.

For series C with the somewhat lower rotation rate, the average value of the quadrupole moment appears to be slightly lower ($\sim 7\text{--}9 \times 10^{39}$ kg m²) than in series D ($\sim 1\text{--}2 \times 10^{40}$ kg m²), while the standard deviation appears to be larger for series C ($\sim 2 \times 10^{39}$ kg m²) than for series D ($\sim 6\text{--}10 \times 10^{38}$ kg m²). Within the range of uncertainty, the mean value and the variation appear to be similar within the set of simulations C1, C2, and C3, as well as within the set of simulations D1, D2, and D3. This is to say that the centrifugal force does not appear to affect the mean value of the quadrupole moment very strongly. The standard deviation appears to be almost unaffected by the centrifugal force within set C. Some more coherent variations are visible in run D2 and particularly in run D3, where the centrifugal force is the strongest of all runs. We note further that the drop of the mean quadrupole moment value in run D3 around $t = 100$ yr coincides with a decrease in the mean radial magnetic field around the same time, which is shown in Fig. 7. The magnetic field structure and its time evolution is clearly different in all simulations, and we also find differences in simulations with and without the centrifugal force. It is difficult to assess, however, whether the origin of this difference is essentially related to a possible bimodality of the solutions or if the centrifugal force specifically introduces a different type of behavior. Overall, the results thus indicate that the stellar quadrupole moment is not very sensitive to the centrifugal force.

4. Discussion and conclusions

We presented a series of numerical simulations with which we investigated stellar dynamos of solar-mass stars with angular velocities of 20 and 30 times the solar rotation. The simula-

tions were performed using the enhanced luminosity method (Brandenburg et al. 2005; Käpylä et al. 2013; Navarrete et al. 2020) to avoid prohibitively large gaps in the relevant timescales. This entails the use of correspondingly enhanced rotation rates to ensure a realistic Coriolis number in the simulations, which is required to reach realistic magnitudes of the drivers of dynamo action, such as the α and Ω effects. We included and varied the strength of the centrifugal force in these simulations, including cases without the centrifugal force or where the strength of the centrifugal force was enhanced by an order of magnitude.

The centrifugal force in general causes perturbations during the nonlinear evolution, so that the models evolve differently in the details, although it is hard to identify clear systematic effects. We note in particular that the averaged radial density profile of the stars remains almost unchanged, while the density difference between the equator and high latitudes (60°) changes by a relative amount of 10^{-4} . We see some difference between the distribution of axisymmetric and nonaxisymmetric modes of the dynamo, and the convective power spectra are affected by the strength of the angular velocity, but not so much by the centrifugal force. Except for the behavior of the density difference (Fig. 1), we found no clear systematic effects that were due to the centrifugal force.

We similarly find that the mean and standard deviation of the quadrupole moment depend more strongly on the angular velocity, while the influence of the centrifugal force is weak or almost nonexistent, even in the simulation in which the centrifugal force term is enhanced by an order of magnitude. This is highly relevant because in the original models proposed by Applegate (1992), the centrifugal force term was supposed to give rise to the variation in stellar quadrupole moment, while here we find similar variations regardless of the presence of the centrifugal force. This suggests that the centrifugal force plays only a minor role in causing this variation, as the overall flow patterns within the star are driven by more complex dynamics resulting from the nonlinear evolution of the system. Adopting the parameters of V471 Tau (Völschow et al. 2016) and inserting the quadrupole variations that we find here into the framework of Applegate (1992; see Navarrete et al. 2022), that is,

$$\frac{\Delta P}{P} = -9 \frac{\Delta Q_{xx}}{Ma^2}, \quad (25)$$

where $\Delta P/P$ is the variation of the period of the binary, ΔQ_{xx} is the variation of the quadrupole moment, M is the stellar mass, and a is the binary separation, we obtain period variations of the order of $10^{-8}\dots 10^{-9}$, whereas the amplitude of the period variation of close binaries is around $10^{-6}\dots 10^{-7}$ (see, e.g., Völschow et al. 2018), and about 8.5×10^{-7} for V471 Tau (Zaire et al. 2022). While the original model was useful to motivate the possible origin of the fluctuations via magnetic activity, it appears to have difficulties overall in explaining the observed magnitude of the variations, and the centrifugal force is unlikely to be the main driver of the variations.

As in our previous studies, we chose to apply our results to V471 Tau alone because of the similarities between the extension of the convective zones of our model and the real K2 dwarf. We can roughly rescale the gravitational quadrupole moment variations obtained here to a target star of mass \tilde{M} and radius \tilde{R} by assuming that the quadrupole moment scales with the stellar inertial moment, that is,

$$\Delta \tilde{Q}_{xx} = \frac{\tilde{M}\tilde{R}^2}{MR^2} \Delta Q_{xx}, \quad (26)$$

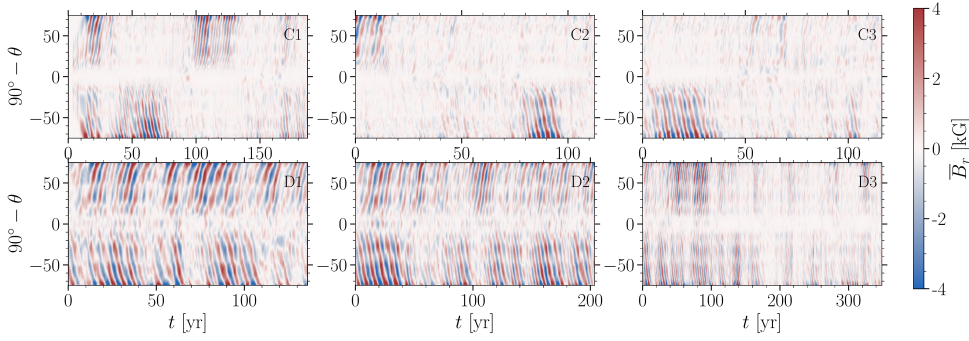


Fig. 7. Mean (azimuthally averaged) radial magnetic field near the surface for all runs.

where M and R are the mass and radius of our simulated star. Choosing the parameters of NN Ser of $\tilde{M} = 0.111M_{\odot}$, $\tilde{R} = 0.149R_{\odot}$, and $a = 0.934R_{\odot}$ (Völschow et al. 2016) yields

$$\frac{\Delta P}{P} = 2.34 \times 10^{-9}, \quad (27)$$

which is a few hundred times lower than the value estimated from observations (Völschow et al. 2016). This number should be taken with extreme caution, however. A potential error source is the missing effect of rotation in Eq. (26). The value of $\Delta \tilde{Q}_{xx}$ is a rather crude estimate and results from self-consistent simulations that will be presented elsewhere.

As in previous work (e.g., Navarrete et al. 2020, 2022), our simulations confirm that MHD simulations of stellar dynamos naturally produce an evolution of the stellar quadrupole moment, including one varying and one approximately constant component. The time-varying component may be somewhat too small to explain the observed ETVs. As suggested in models by Applegate (1989) and Lanza (2020), a roughly constant component might produce the variations caused by spin-orbit coupling via libration or circulation (see also the discussion in Navarrete et al. 2022). As our simulations indeed show a mean and a fluctuating part of the quadrupole moment, the observed real variation may well consist of a superposition of the two components, where the relative strength may depend on the specific system and its parameters. As has been demonstrated by Navarrete et al. (2020), the presence of magnetic fields is crucial because purely hydrodynamic simulations only produce short-term variations on the sound-crossing timescale of the star, but no longer-term variations on timescales of years or decades.

From the results obtained here, we thus conclude that neither the thin-shell model by Applegate (1992) nor the finite-shell model by Brinkworth et al. (2006) correctly describes the origin of the quadrupole moment variation because they both assume it to originate in the centrifugal force and in an internal redistribution of the angular velocity, while in our simulations, a change in centrifugal force term does not lead to any appreciable change in the mean or fluctuating component of the quadrupole. The physics causing these variations thus requires modeling the stellar dynamo with compressible MHD in three dimensions.

Another possibility is given by hybrid solutions in which ETVs receive contributions of magnetic origin and from planets. Mai & Mutel (2022) considered such a scenario for three PCEBs as neither planets nor the Applegate mechanism can fully account for ETVs. We conclude by encouraging studies of the detection of circumbinary planets around PCEBs as well as Zeeman-Doppler imaging of their main-sequence components. The combination of these subjects will help us constrain the

planetary orbits and masses, and to understand to which extent we can use ETVs to study stellar magnetic fields.

Acknowledgements. We thank the referee for a detailed review and helpful comments that improved the manuscript. F.H.N. acknowledges financial support from the DAAD (Deutscher Akademischer Austauschdienst; code 91723643) for his doctoral studies. D.R.G.S. gratefully acknowledges support by the ANID BASAL projects ACE210002 and FB210003, as well as via the Millennium Nucleus NCN19-058 (TITANs). D.R.G.S. and C.A.O.R. thank for funding via Fondecyt Regular (project code 1201280). P.J.K. acknowledges financial support by the Deutsche Forschungsgemeinschaft Heisenberg programme (grant No. KA 4825/4-1).

References

- Applegate, J. H. 1989, *ApJ*, **337**, 865
 Applegate, J. H. 1992, *ApJ*, **385**, 621
 Applegate, J. H., & Patterson, J. 1987, *ApJ*, **322**, L99
 Beuermann, K., Hessman, F. V., Dreizler, S., et al. 2010, *A&A*, **521**, L60
 Beuermann, K., Breitenstein, P., Debski, B., et al. 2012, *A&A*, **540**, A8
 Beuermann, K., Dreizler, S., & Hessman, F. V. 2013, *A&A*, **555**, A133
 Bours, M. C. P., Marsh, T. R., Parsons, S. G., et al. 2016, *MNRAS*, **460**, 3873
 Brandenburg, A., Chan, K. L., Nordlund, Å., & Stein, R. F. 2005, *Astron. Nachr.*, **326**, 681
 Brinkworth, C. S., Marsh, T. R., Dhillon, V. S., & Knigge, C. 2006, *MNRAS*, **365**, 287
 Decampli, W. M., & Baliunas, S. L. 1979, *ApJ*, **230**, 815
 Hardy, A., Schreiber, M. R., Parsons, S. G., et al. 2015, *ApJ*, **800**, L24
 Käpylä, P. J., Mantere, M. J., Cole, E., Warnecke, J., & Brandenburg, A. 2013, *ApJ*, **778**, 41
 Käpylä, P. J., Gent, F. A., Olsper, N., Käpylä, M. J., & Brandenburg, A. 2020, *Geophys. Astrophys. Fluid Dyn.*, **114**, 8
 Kitchatinov, L. L., & Rüdiger, G. 1995, *A&A*, **299**, 446
 Lanza, A. F. 2006, *MNRAS*, **369**, 1773
 Lanza, A. F. 2020, *MNRAS*, **491**, 1820
 Mai, X., & Mutel, R. L. 2022, *MNRAS*, **513**, 2478
 Marsh, T. R., & Pringle, J. E. 1990, *ApJ*, **365**, 677
 Matese, J. J., & Whitmire, D. P. 1983, *A&A*, **117**, L7
 Mustill, A. J., Marshall, J. P., Villaver, E., et al. 2013, *MNRAS*, **436**, 2515
 Navarrete, F. H., Schleicher, D. R. G., Zamponi Fuentelba, J., & Völschow, M. 2018, *A&A*, **615**, A81
 Navarrete, F. H., Schleicher, D. R. G., Käpylä, P. J., et al. 2020, *MNRAS*, **491**, 1043
 Navarrete, F. H., Käpylä, P. J., Schleicher, D. R. G., Ortiz, C. A., & Banerjee, R. 2022, *A&A*, **663**, A90
 Ogilvie, G. I., & Lin, D. N. C. 2007, *ApJ*, **661**, 1180
 Pencil Code Collaboration (Brandenburg, A., et al.) 2021, *J. Open Source Software*, **6**, 2807
 Schleicher, D. R. G., & Dreizler, S. 2014, *A&A*, **563**, A61
 Vaccaro, T. R., Wilson, R. E., Van Hamme, W., & Terrell, D. 2015, *ApJ*, **810**, 157
 Viviani, M., Warnecke, J., Käpylä, M. J., et al. 2018, *A&A*, **616**, A160
 Völschow, M., Banerjee, R., & Hessman, F. V. 2014, *A&A*, **562**, A19
 Völschow, M., Schleicher, D. R. G., Perdelwitz, V., & Banerjee, R. 2016, *A&A*, **587**, A34
 Völschow, M., Schleicher, D. R. G., Banerjee, R., & Schmitt, J. H. M. M. 2018, *A&A*, **620**, A42
 Zahn, J. P., & Bouchet, L. 1989, *A&A*, **223**, 112
 Zaire, B., Donati, J. F., & Klein, B. 2022, *MNRAS*, **513**, 2893
 Zorotovic, M., & Schreiber, M. R. 2013, *A&A*, **549**, A95

Chapter 5

Paper III

Contribution

Similarly to the previous two papers, the simulations were run by me in the context of my computing proposal. The data was analyzed by me and I prepared the paper. This was accepted in *Astronomy & Astrophysics* and its status is in press. A preprint can be found on <https://arxiv.org/abs/2305.01312>.

Effects of the centrifugal force in stellar dynamo simulations

Felipe H. Navarrete^{1,*}, Petri J. Käpylä^{2,3}, Dominik R.G. Schleicher⁴, and Robi Banerjee¹

¹ Hamburger Sternwarte, Universität Hamburg, Gojenbergsweg 112, 21029 Hamburg, Germany
e-mail: felipe.navarrete@hs.uni-hamburg.de

² Leibniz-Institut für Sonnenphysik (KIS), Schöneckstr. 6, 79104 Freiburg, Germany

³ Institut für Astrophysik und Geophysik, Georg-August-Universität Göttingen, Friedrich-Hund-Platz 1, 37077, Göttingen, Germany

⁴ Departamento de Astronomía, Facultad de Ciencias Físicas y Matemáticas, Universidad de Concepción, Av. Esteban Iturra s/n Barrio Universitario, Casilla 160-C, Chile

Received –; accepted –

ABSTRACT

Context. The centrifugal force is often omitted from simulations of stellar convection either for numerical reasons or because it is assumed to be weak compared to the gravitational force. However, the centrifugal force might be an important factor in rapidly rotating stars, such as solar analogs, due to its Ω^2 scaling, where Ω is the rotation rate of the star.

Aims. We study the effects of the centrifugal force in a set of 21 semi-global stellar dynamo simulations with varying rotation rates. Included in the set are three control runs aimed at distinguishing the effects of the centrifugal force from the nonlinear evolution of the solutions.

Methods. We solved the 3D magnetohydrodynamic equations with the PENCIL CODE in a solar-like convective zone in a spherical wedge setup with a 2π azimuthal extent. The rotation rate and the amplitude of the centrifugal force were varied. We decomposed the magnetic field into spherical harmonics and studied the migration of azimuthal dynamo waves (ADWs), the energy of different large-scale magnetic modes, and differential rotation.

Results. In the regime with the lowest rotation rates, $\Omega = 5 - 10\Omega_\odot$, where Ω_\odot is the rotation rate of the Sun, we see no marked changes in either the differential rotation or the magnetic field properties. For intermediate rotation, $\Omega = 20 - 25\Omega_\odot$, we identify an increase in the differential rotation as a function of centrifugal force. The axisymmetric magnetic energy tends to decrease with centrifugal force, while the non-axisymmetric one increases. The ADWs are also affected, especially in the propagation direction. In the most rapidly rotating set with $\Omega = 30\Omega_\odot$, these changes are more pronounced, and in one case the propagation direction of the ADW changes from prograde to retrograde. The control runs suggest that the results are a consequence of the centrifugal force and not due to the details of the initial conditions or the history of the run.

Conclusions. We find that the differential rotation and properties of the ADWs only change as a function of the centrifugal force when rotation is rapid enough.

Key words. Turbulence – Convection – Dynamo – Stars: magnetic field

1. Introduction

Simulations of stellar convection, usually aimed at explaining solar phenomena, often omit the centrifugal force. This is due to the assumption that its amplitude is small due to the relatively slow rotation of the Sun. Earlier in its history, however, the Sun must have been rotating much more rapidly because, in general, stars are born with larger angular momenta that are slowly reduced via magnetic braking (Skumanich 1972; Matt et al. 2012). Therefore, the influence of the centrifugal force is expected to be more important at earlier stages because its amplitude increases as the square of the rotation rate. To study these phases of rapid rotation in the solar context, such as magnetic field evolution, one has to study young solar analogs at earlier phases that are rotating much faster than the Sun (e.g., Lehtinen et al. 2016). This allows us to study the evolution of the Sun up to the present, given that outflows that are produced by magnetic braking do not significantly affect the structure of the star, only the rotation rate.

Observations by Lehtinen et al. (2016) of magnetic fields of solar analogs reveal that they are active and show a character-

istic split between the axisymmetric and non-axisymmetric spot distributions. These authors also estimate that, among solar-like stars with non-axisymmetric spot distribution, the active longitude periods are shorter than the rotation period of the star. One plausible explanation is the presence of azimuthal dynamo waves (ADWs). These waves propagate in the rotating frame of reference of the star either in prograde or retrograde fashion with a uniform frequency irrespective of the underlying fluid motions. Such solutions were first discovered in linear mean-field dynamo models (e.g., Krause & Rädler 1980). To explain their observations, Lehtinen et al. (2016) argue that the propagation of the ADWs must be prograde.

V530 Per is an extreme case of a rapidly rotating Sun-like star with an estimated rotation period of 0.32 days (Cang et al. 2020), which corresponds to about $75\Omega_\odot$, where Ω_\odot is the rotation rate of the Sun. This makes the gravitational force at its surface only 9.5 times larger than the centrifugal force. In comparison, in the Sun this ratio is 5.3×10^4 . There are also clear differences between the magnetic field of V530 Per and the Sun. For example, Cang et al. (2020) also find that the magnetic field distribution of V530 Per is asymmetric with respect to the equator. It is characterized by a stronger magnetic field near the north

* e-mail: felipe.navarrete@hs.uni-hamburg.de

pole, with a peak field strength of 1 kG. It is as yet unclear why similar stars have different field strengths and symmetries, but there are indications that rotation may play an important role in the magnetic activity of Sun-like stars (Lehtinen et al. 2016) as well as low-mass stars (e.g., Reiners et al. 2022).

Such rapid rotation is commonly found in close binaries if tidal locking is assumed. For example, V471 Tau is a post-common-envelope binary in which the secondary is a main-sequence solar-like star with a mass of $0.93M_{\odot}$, a radius of $0.96R_{\odot}$, and a binary period of about 0.5 days (e.g., Völschow et al. 2016). If tidal locking is assumed, this gives a ratio of gravitation to centrifugal forces of about 22. Interestingly, Zaire et al. (2022) analyzed the magnetic activity of the K2 star in V471 Tau and find that the magnetic field is also dominated by a concentration on one hemisphere. They also find that the spot coverage and brightness map, derived from Zeeman-Doppler imaging, do not follow the magnetic activity cycle inferred from H α variability. This suggests that it might be inappropriate to use spot coverage to study magnetic cycles in rapidly rotating stars (Zaire et al. 2022).

Simulations of stellar dynamos often produce ADWs whose characteristics change with the rotation rate and the physics involved. Cole et al. (2014) studied the propagation properties of ADWs in a set of three runs with moderate rotation rates of up to 6.7 times the solar value with 3D magnetohydrodynamic simulations. They find that the waves have a rotation rate that is slower than that of the gas, that is, they are retrograde. The magnetic structure in the ADW propagates like a rigid body, and therefore such motion cannot be explained by advection by the fluid in a differentially rotating convection zone. This result was later confirmed by Viviani et al. (2018) with a larger set of runs. Most of their runs show retrograde ADWs independently of the rotation rate, but in some cases standing or prograde waves appeared. Recently, Viviani & Käpylä (2021) presented a set of four runs with moderate rotation rates where the usual prescribed radial dependence of the radiative heat conductivity was replaced by the more realistic Kramers opacity law (Brandenburg et al. 2000; Käpylä et al. 2017). This suggests that using this heat conductivity might affect the direction of the propagation of ADWs indirectly by affecting the flow through the pressure gradient and/or dissipation. However, it might come with the cost of pushing the transition point of differential rotation profiles of simulations from anti-solar profiles to solar-like profiles to even larger Coriolis numbers (Viviani & Käpylä 2021).

Navarrete et al. (2022b) explored the effect of the centrifugal force in the context of changes in the internal structure of the stars, with the aim to check whether the resulting changes are sufficient to explain the observed eclipsing time variations in post-common-envelope binaries, as proposed in the Applegate scenario (Applegate 1992). In this paper we study the effects of centrifugal force in semi-global dynamo simulations further. We focus on differential rotation, magnetic energy, and ADW propagation. In Sect. 2 we present the model and the implementation of the centrifugal force. Section 3 presents the results, and our conclusions are drawn in Sect. 4.

2. Model

We solved the fully compressible magnetohydrodynamic equations in a spherical grid with coordinates (r, Θ, ϕ) , where $0.7R \leq r \leq R$ is radius and R is the radius of the star, $\pi/12 \leq \Theta \leq 11\pi/12$ is the colatitude, and $0 \leq \phi < 2\pi$ is the longitude. The model is the same as in Käpylä et al. (2013) and Navarrete et al. (2020,

2022a). The equations adopt the following forms:

$$\frac{\partial \mathbf{A}}{\partial t} = \mathbf{u} \times \mathbf{B} - \eta \mu_0 \mathbf{J}, \quad (1)$$

$$\frac{D \ln \rho}{Dt} = -\nabla \cdot \mathbf{u}, \quad (2)$$

$$\frac{D\mathbf{u}}{Dt} = \mathcal{F}^{\text{grav}} + \mathcal{F}^{\text{Cor}} + \mathcal{F}^{\text{cent}} - \frac{1}{\rho}(\nabla p - \mathbf{J} \times \mathbf{B} - \nabla \cdot 2\nu\rho\mathbf{S}), \quad (3)$$

$$T \frac{Ds}{Dt} = \frac{1}{\rho} \left[\eta \mu_0 \mathbf{J}^2 - \nabla \cdot (\mathbf{F}^{\text{rad}} + \mathbf{F}^{\text{SGS}}) \right] + 2\nu \mathbf{S}^2, \quad (4)$$

where \mathbf{A} is the magnetic vector potential, $\mathbf{B} = \nabla \times \mathbf{A}$ is the magnetic field, \mathbf{u} is the velocity field, η is the magnetic diffusivity, μ_0 is the vacuum permeability, t is the time, $\mathbf{J} = \nabla \times \mathbf{B}/\mu_0$ is the electric current density, ρ is the mass density, p is the pressure, ν is the viscosity,

$$S_{ij} = \frac{1}{2}(u_{i;j} - u_{j;i}) - \frac{1}{3}\delta_{ij}\nabla \cdot \mathbf{u} \quad (5)$$

is the rate-of-strain tensor, where semicolons denote covariant differentiation, T is the temperature, and s is the specific entropy. Furthermore, $\mathbf{F}^{\text{rad}} = -K\nabla T$ is the radiative flux, which we modeled with the diffusion approximation, where $K = K(r)$ has a fixed spatial profile (see Sect. 2.1 in Käpylä et al. 2014). We also investigated the effects of Kramers opacity in some runs (see Sect. 3.3). We did this by replacing the radiative heat conductivity, K , in the radiative flux term $\mathbf{F}^{\text{rad}} = -K\nabla T$ with

$$K = K_0 \left(\frac{\rho}{\rho_0} \right)^{-(a+1)} \left(\frac{T}{T_0} \right)^{3-b}, \quad (6)$$

where $a = 1$ and $b = -7/2$ correspond to the Kramers opacity law (Brandenburg et al. 2000). Here, K_0 is a constant that depends on natural constants and, in simulations, on the luminosity of the model (Viviani & Käpylä 2021). The $\mathbf{F}^{\text{SGS}} = -\chi_{\text{SGS}}\rho T\nabla s$ is a sub-grid scale flux that we implemented to smooth grid-scale fluctuations that would otherwise make the system unstable. Here, χ_{SGS} is the sub-grid scale entropy diffusivity, and it varies smoothly from 0 at $r/R = 0.7$ to 0.4ν at $r/R = 0.72$; it then smoothly increases by a factor of 12.5 at $r/R = 0.98$, above which it is constant. The first three terms on the right-hand side of Eq. (4),

$$\mathcal{F}^{\text{grav}} = -(GM/r^2)\hat{\mathbf{r}}, \quad (7)$$

$$\mathcal{F}^{\text{Cor}} = -2\boldsymbol{\Omega}_0 \times \mathbf{u}, \quad (8)$$

$$\mathcal{F}^{\text{cent}} = -c_f \boldsymbol{\Omega}_0 \times (\boldsymbol{\Omega}_0 \times \mathbf{r}), \quad (9)$$

are the gravitational, Coriolis, and centrifugal forces.

2.1. Boundary and initial conditions

The magnetic field follows a perfect conductor condition at the bottom of the convective zone and is radial at the surface. The temperature gradient was kept fixed at the bottom, whereas at the top we applied a black-body condition. For the entropy and density, we assumed a vanishing first derivative at both latitudinal boundaries. The latitudinal boundaries are stress-free and perfectly conducting. The initial state is isentropic. Perturbations were introduced by initializing the magnetic and velocity fields with low-amplitude Gaussian white noise.

2.2. Centrifugal force

The parameter c_f in Eq. (9) was introduced by Käpylä et al. (2020) and controls the strength of the centrifugal force. A c_f value of 1 corresponds to the unaltered centrifugal force amplitude, and $c_f = 0$ implies no centrifugal force. It is defined as

$$c_f = \frac{|\mathcal{F}_0^{\text{cent}}|}{|\mathcal{F}_0^{\text{cent}}|}, \quad (10)$$

with $|\mathcal{F}_0^{\text{cent}}|$ being the unaltered magnitude of the centrifugal force. The necessity of controlling the centrifugal force is due to the enhanced luminosity and rotation rate in simulations of compressible stellar (magneto-)convection. Similarly to Käpylä et al. (2020), each run was initialized with $c_f = 0$ and was increased in small incremental steps after the saturated regime is reached.

To get a sense of how strong the centrifugal force is in our simulations, we computed the ratio of centrifugal to gravitational forces in the simulations as well as in a real Sun-like star with the same rotation rate. We defined the ratio between the two as

$$\mathcal{F} = \frac{(|\mathcal{F}^{\text{cent}}|/|\mathcal{F}^{\text{grav}}|)_{\text{sim}}}{(|\mathcal{F}^{\text{cent}}|/|\mathcal{F}^{\text{grav}}|)_{\star}}, \quad (11)$$

where the subscripts \star denote the real star and “sim” the simulations. These values are shown in the last column of Table 1. By using a value as low as $c_f = 10^{-4}$, our simulations are influenced by the centrifugal force just below the value that the equivalent star with the same rotation rate and radius would have, and the simulations that have the strongest centrifugal force have $\mathcal{F} = 87$.

3. Results

We ran a total of 21 simulations separated into five sets: C, D, E, F, and G. Each set is characterized by a fixed rotation rate of 5, 10, 20, 25, and 30 times the solar rotation rate, respectively. We varied the value of the centrifugal force within each set.

3.1. Differential rotation

We began by exploring changes in the differential rotation of the simulations by defining

$$\Delta_{\Omega}^{(60^\circ)} = \frac{\overline{\Omega}(0^\circ, s) - \overline{\Omega}(60^\circ, s)}{\overline{\Omega}(0, s)} \quad (12)$$

and

$$\Delta_{\Omega}^{(r)} = \frac{\overline{\Omega}(0^\circ, s) - \overline{\Omega}(0^\circ, b)}{\overline{\Omega}(0^\circ, s)} \quad (13)$$

as measures of latitudinal and radial differential rotation. Here, s and b indicate that the values are taken near the surface ($r = 0.98R$) and the bottom ($r = 0.72R$), respectively, and $\overline{\Omega} = \Omega_0 + \overline{u}_\phi/(r \sin \theta)$, where the overbars denote azimuthal averaging, namely

$$\overline{u}_\phi = \frac{1}{2\pi} \int_0^{2\pi} u_\phi(r, \theta, \phi, t) d\phi. \quad (14)$$

In what follows, additional time-averaging is denoted by $\langle \cdot \rangle_t$. Time averages of $\Delta_{\Omega}^{(60^\circ)}$ and $\Delta_{\Omega}^{(r)}$ are listed in columns 8 and 9 of Table 1.

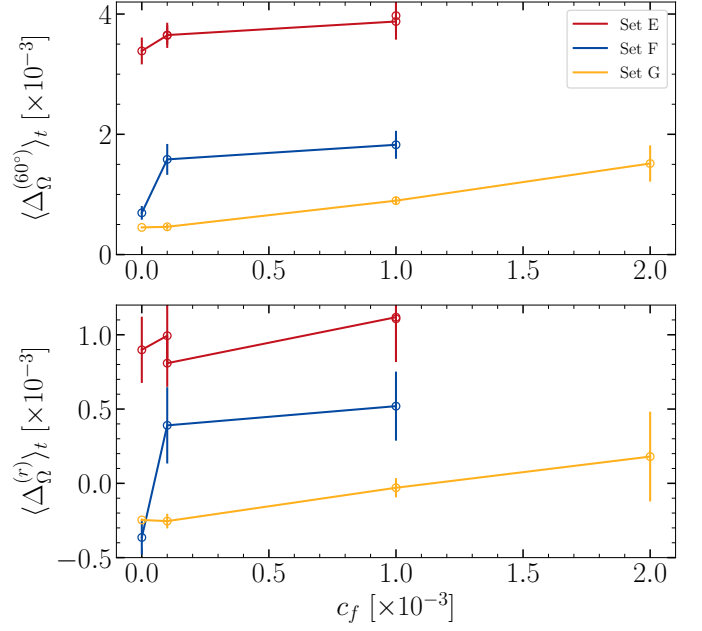


Fig. 1. Time-averaged differential rotation for sets E, F, and G in red, blue, and yellow, respectively. The top and bottom panels show $\Delta_{\Omega}^{(60^\circ)}$ and $\Delta_{\Omega}^{(r)}$ according to Eqs. (12) and (13), respectively.

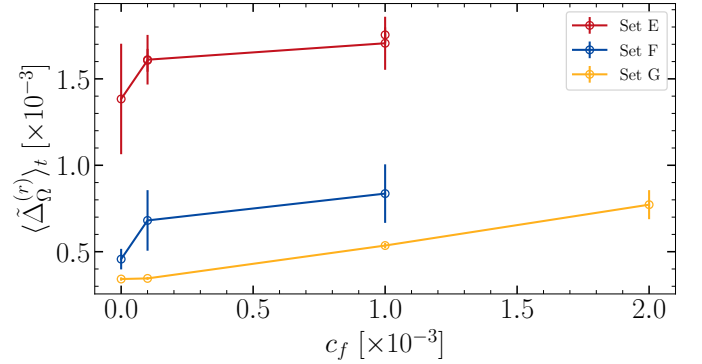


Fig. 2. Time-averaged radial differential rotation as defined in Eq. (15).

In the slowly rotating runs, sets C and D, there are changes in both radial and latitudinal differential rotation, but they are very small. Comparing the runs without the centrifugal force with those with the largest value of c_f , the biggest change in $\Delta_{\Omega}^{(r)}$, of about 20%, is in set D. However, larger deviations are found in sets E, F, and G. They are also shown in Fig. 1 with the corresponding error bars, which were estimated by computing the average of three equally long parts of the time series and taking the largest deviation from the total as the error. In set E we see that the differential rotation of the runs that were initialized with the same c_f but at a different time, namely E2 with E3 and E4 with E5, have very similar values. This shows that the averaged differential rotation does not significantly depend on the initial conditions when the centrifugal force is added. Within this set, the maximum deviation of $\Delta_{\Omega}^{(r)}$ is about 23% between runs E1 and E5. In contrast, $\Delta_{\Omega}^{(60^\circ)}$ is reduced by about 17%.

Recently, Käpylä (2023) noted that the details of the radial profile of $\overline{\Omega}$ can introduce spurious effects into the measure of differential rotation as defined in Eq. (13). Following their approach, we defined the mean rotational profile at the equator as

Table 1. Summary of the simulation parameters.

Run	Ω/Ω_\odot	c_f	Co	Ta	Re	Rm	$\langle\Delta_\Omega^{(60^\circ)}\rangle_t$	$\langle\Delta_\Omega^{(r)}\rangle_t$	\mathcal{F}
C1	5	0	7.3	1.6×10^8	3.0×10^3	3.0×10^3	4.2×10^{-2}	2.5×10^{-2}	0
C2	5	10^{-4}	7.3	1.6×10^8	3.0×10^3	3.0×10^3	4.3×10^{-2}	2.5×10^{-2}	0.87
C3	5	10^{-3}	7.3	1.6×10^8	3.0×10^3	3.0×10^3	4.4×10^{-2}	2.6×10^{-2}	8.7
C4	5	10^{-2}	6.8	1.6×10^8	3.2×10^3	3.2×10^3	4.8×10^{-2}	2.8×10^{-2}	87
D1	10	0	20	6.3×10^8	2.2×10^3	2.2×10^3	1.3×10^{-2}	5.6×10^{-3}	0
D2	10	10^{-4}	20	6.3×10^8	2.2×10^3	2.2×10^3	1.4×10^{-2}	6.1×10^{-3}	0.87
D3	10	10^{-3}	20	6.3×10^8	2.2×10^3	2.2×10^3	1.4×10^{-2}	6.2×10^{-3}	8.7
D4	10	10^{-2}	20	6.3×10^8	2.2×10^3	2.2×10^3	1.5×10^{-2}	7.0×10^{-3}	87
E1	20	0	57	2.5×10^9	1.6×10^3	1.6×10^3	3.4×10^{-3}	9.0×10^{-4}	0
E2	20	10^{-4}	56	2.5×10^9	1.6×10^3	1.6×10^3	3.7×10^{-3}	9.9×10^{-4}	0.87
E3	20	10^{-4}	54	2.5×10^9	1.6×10^3	1.6×10^3	3.7×10^{-3}	8.1×10^{-4}	0.87
E4	20	10^{-3}	53	2.5×10^9	1.7×10^3	1.7×10^3	3.9×10^{-3}	1.1×10^{-3}	8.7
E5	20	10^{-3}	53	2.5×10^9	1.7×10^3	1.7×10^3	4.0×10^{-3}	1.1×10^{-3}	8.7
F1	25	0	100	4.0×10^9	1.1×10^3	1.1×10^3	6.9×10^{-4}	-3.6×10^{-4}	0
F2	25	10^{-4}	93	4.0×10^9	1.2×10^3	1.2×10^3	1.6×10^{-3}	3.9×10^{-4}	0.87
F3	25	10^{-3}	94	4.0×10^9	1.2×10^3	1.2×10^3	1.8×10^{-3}	5.2×10^{-4}	8.7
G1	30	0	140	5.7×10^9	9.7×10^2	9.7×10^2	4.5×10^{-4}	-2.5×10^{-4}	0
G2	30	10^{-4}	140	5.7×10^9	9.7×10^2	9.7×10^2	4.6×10^{-4}	-2.5×10^{-4}	0.87
G3	30	10^{-3}	130	5.7×10^9	1.0×10^3	1.0×10^3	9.0×10^{-4}	-3.0×10^{-5}	8.7
G4	30	2×10^{-3}	110	5.7×10^9	1.2×10^3	1.2×10^3	1.5×10^{-3}	1.8×10^{-4}	17
G5	30	0	140	5.7×10^9	9.6×10^2	9.6×10^2	4.5×10^{-4}	-2.2×10^{-4}	0

Notes. For each run, $\text{Pr} = 60$, $\text{Pr}_M = 1$, and $\text{Pr}_{\text{SGS}} = 2.5$.

$$\tilde{\Delta}_\Omega^{(r)} = \frac{\int_{r_{\text{in}}}^{r_{\text{out}}} r^2 [\overline{\Omega}(\theta_{\text{eq}}, r) - 1] dr}{\int_{r_{\text{in}}}^{r_{\text{out}}} r^2 dr}, \quad (15)$$

where $r_{\text{in}} = 0.72R$ and $r_{\text{out}} = 0.98R$. In Fig. 2 we plot this quantity as a function of c_f . The differential rotation is solar-like ($\tilde{\Delta}_\Omega^{(r)} > 0$), as already seen in the top panel of Fig. 1. This shows that, if there are transients of anti-solar differential rotation in our simulations, they are not very long and a similar scaling is seen with both definitions.

As the rotation velocity increases more, the amplitude of the latitudinal differential rotation decreases further in run F1. This is a common feature of convection in rotating spherical shells (see, e.g., Brown et al. 2008; Gastine et al. 2014; Viviani et al. 2018), which is also found in Cartesian coordinates with the star-in-a-box setup (Käpylä 2021). In runs F2 and F3, $\langle\Delta_\Omega^{(60^\circ)}\rangle_t$ is larger by a factor of about 2.3 and 2.6. Run F1 has bottom layers that rotate slightly faster than the surface layers, as indicated by the negative sign of $\langle\Delta_\Omega^{(r)}\rangle_t$. The addition of the centrifugal force changes this pattern back to a solar-like one, where the surface layers rotate faster, although the overall differential rotation remains weak.

We do not see major differences between runs G1 and G2, and in G3 the latitudinal (radial) differential rotation increases (decreases) by a factor of about 2 (10). Each of these runs has $\langle\Delta_\Omega^{(60^\circ)}\rangle_t > 0$ and $\langle\Delta_\Omega^{(r)}\rangle_t < 0$. In run G4, $\langle\Delta_\Omega^{(60^\circ)}\rangle_t$ is comparable to that in F2, and, similarly, the radial differential rotation is shifted back to a solar-like pattern. However, the amplitudes are all very small and close to rigid rotation. In the control simulation (G5) we took a snapshot from run G3 and switched off the centrifugal force; we obtained a solution that is nearly the same as in run G1. This hints at the possibility that the effects we are seeing are due to a systematic effect of the centrifugal force rather than a chaotic behavior due to the change in the initial conditions.

Overall, we find that changes in the differential rotation due to the centrifugal force are only noticeable in the rapidly and very rapidly rotating sets E, F, and G. We conclude that the changes in both $\langle\Delta_\Omega^{(60^\circ)}\rangle_t$ and $\langle\Delta_\Omega^{(r)}\rangle_t$ are due to the centrifugal force and are likely insensitive to the details of the initial conditions taken from the parent runs. In a real star, the centrifugal force would also change the geometry of the star. However, we cannot assess the extent of this change because the fixed grid in our model does not allow the geometry to change.

3.2. Magnetic energy

The magnetic energy of the first three azimuthal modes near the surface are listed in Table 2 and shown as a function of the centrifugal force amplitude in Fig. 3. It is defined as

$$E_{\text{mag}}^{m=i} = \frac{1}{2\mu_0} \left\langle \sum_{l \geq m} B_{l,m=i}^2 \right\rangle_{\theta\phi t}, \quad (16)$$

where $B_{l,m=i}$ are obtained from the spherical harmonic decomposition. At slow rotation, sets C and D do not show significant changes in the energy as the centrifugal force increases. At the same time, we also see that in set C the axisymmetric mode dominates the runs. This contrasts with the previous study of Viviani et al. (2018), who find that, at rotation rates larger than $\Omega/\Omega_\odot \sim 1.8$, the $m = 1$ mode dominates the runs, and after $\Omega/\Omega_\odot \sim 20$ the dominance falls back to $m = 0$. However, at higher grid resolutions, they find that this trend is suppressed and so the $m = 1$ mode dominated again. In the current simulations, we find that this trend only starts to show up in set D. In all cases, the $m = 2$ mode is always subdominant by a factor of roughly 10.

Similarly to the differential rotation, the effects of the centrifugal force are more noticeable in sets E, F, and G. In this rapidly rotating regime, the axisymmetric mode is always sub-

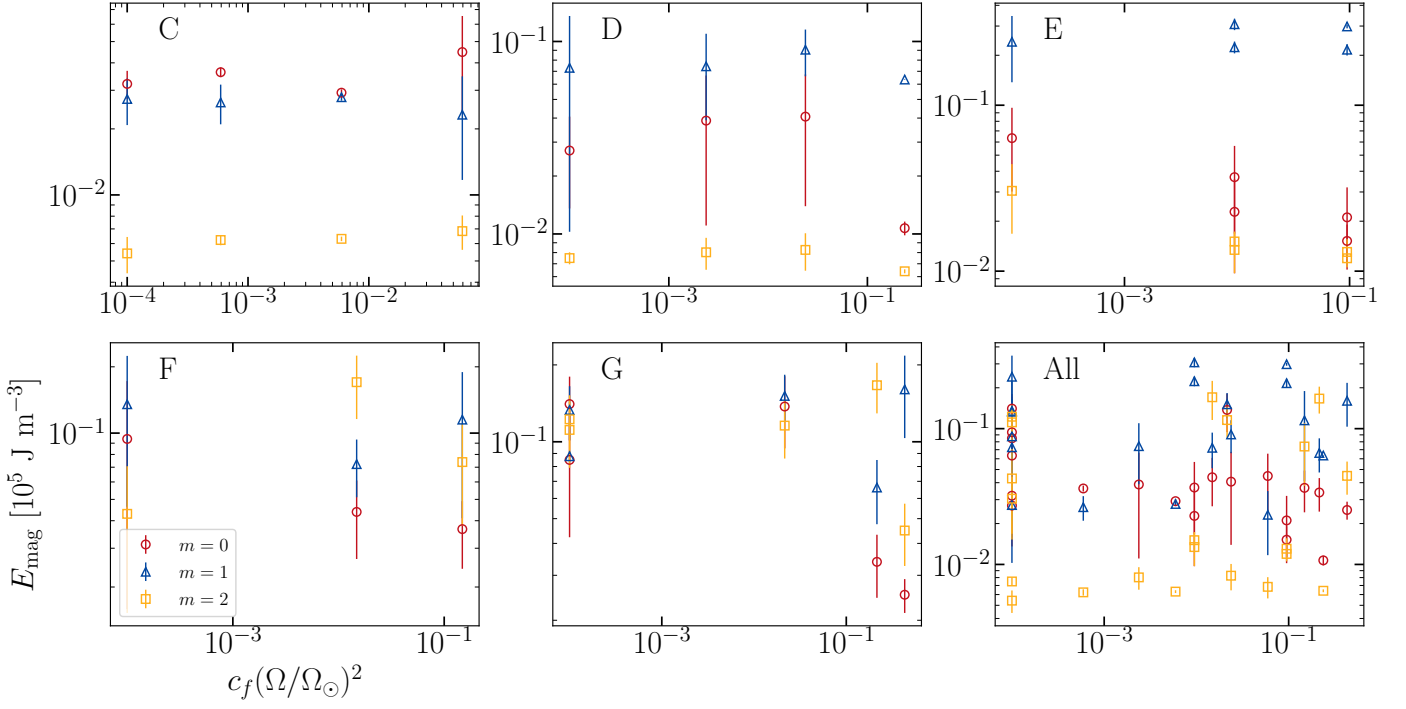


Fig. 3. Magnetic energy of the three lowest azimuthal modes (m) as a function of the centrifugal force amplitude. Runs with $c_f = 0$ are given a fiducial value of $c_f(\Omega/\Omega_\odot)^2 = 10^{-4}$.

Table 2. Magnetic energy density from the spherical harmonic decomposition for each run in units of 10^5 J m^{-3} .

Run	$E_{\text{mag}}^{m=0}$	$E_{\text{mag}}^{m=1}$	$E_{\text{mag}}^{m=2}$
C1	$3.2 \times 10^{-2} \pm 4.7 \times 10^{-3}$	$2.7 \times 10^{-2} \pm 6.6 \times 10^{-3}$	$5.4 \times 10^{-3} \pm 1.0 \times 10^{-3}$
C2	$3.6 \times 10^{-2} \pm 1.8 \times 10^{-3}$	$2.6 \times 10^{-2} \pm 5.4 \times 10^{-3}$	$6.2 \times 10^{-3} \pm 3.3 \times 10^{-4}$
C3	$2.9 \times 10^{-2} \pm 1.0 \times 10^{-3}$	$2.8 \times 10^{-2} \pm 1.0 \times 10^{-3}$	$6.3 \times 10^{-3} \pm 1.5 \times 10^{-4}$
C4	$4.5 \times 10^{-2} \pm 2.1 \times 10^{-2}$	$2.3 \times 10^{-2} \pm 1.1 \times 10^{-2}$	$6.8 \times 10^{-3} \pm 1.2 \times 10^{-3}$
D1	$2.7 \times 10^{-2} \pm 1.4 \times 10^{-2}$	$7.3 \times 10^{-2} \pm 6.3 \times 10^{-2}$	$7.5 \times 10^{-3} \pm 5.4 \times 10^{-4}$
D2	$3.9 \times 10^{-2} \pm 2.8 \times 10^{-2}$	$7.4 \times 10^{-2} \pm 3.5 \times 10^{-2}$	$8.0 \times 10^{-3} \pm 1.5 \times 10^{-3}$
D3	$4.1 \times 10^{-2} \pm 2.7 \times 10^{-2}$	$9.1 \times 10^{-2} \pm 2.5 \times 10^{-2}$	$8.3 \times 10^{-3} \pm 1.8 \times 10^{-3}$
D4	$1.1 \times 10^{-2} \pm 8.8 \times 10^{-4}$	$6.3 \times 10^{-2} \pm 2.0 \times 10^{-4}$	$6.4 \times 10^{-3} \pm 1.5 \times 10^{-4}$
E1	$6.3 \times 10^{-2} \pm 3.3 \times 10^{-2}$	$2.4 \times 10^{-1} \pm 1.0 \times 10^{-1}$	$3.0 \times 10^{-2} \pm 1.4 \times 10^{-2}$
E2	$2.3 \times 10^{-2} \pm 1.3 \times 10^{-2}$	$2.2 \times 10^{-1} \pm 1.8 \times 10^{-2}$	$1.3 \times 10^{-2} \pm 3.7 \times 10^{-3}$
E3	$3.7 \times 10^{-2} \pm 2.0 \times 10^{-2}$	$3.1 \times 10^{-1} \pm 2.4 \times 10^{-2}$	$1.5 \times 10^{-2} \pm 2.2 \times 10^{-3}$
E4	$2.1 \times 10^{-2} \pm 1.1 \times 10^{-2}$	$2.2 \times 10^{-1} \pm 1.7 \times 10^{-2}$	$1.3 \times 10^{-2} \pm 2.5 \times 10^{-3}$
E5	$1.5 \times 10^{-2} \pm 3.9 \times 10^{-3}$	$3.0 \times 10^{-1} \pm 7.9 \times 10^{-3}$	$1.2 \times 10^{-2} \pm 4.0 \times 10^{-5}$
F1	$9.4 \times 10^{-2} \pm 7.8 \times 10^{-2}$	$1.4 \times 10^{-1} \pm 8.9 \times 10^{-2}$	$4.3 \times 10^{-2} \pm 2.8 \times 10^{-2}$
F2	$4.4 \times 10^{-2} \pm 1.7 \times 10^{-2}$	$7.2 \times 10^{-2} \pm 2.1 \times 10^{-2}$	$1.7 \times 10^{-1} \pm 5.4 \times 10^{-2}$
F3	$3.7 \times 10^{-2} \pm 1.2 \times 10^{-2}$	$1.2 \times 10^{-1} \pm 7.4 \times 10^{-2}$	$7.4 \times 10^{-2} \pm 3.6 \times 10^{-2}$
G1	$1.4 \times 10^{-1} \pm 3.9 \times 10^{-2}$	$1.3 \times 10^{-1} \pm 3.2 \times 10^{-2}$	$1.2 \times 10^{-1} \pm 3.0 \times 10^{-2}$
G2	$1.4 \times 10^{-1} \pm 4.3 \times 10^{-2}$	$1.5 \times 10^{-1} \pm 3.2 \times 10^{-2}$	$1.2 \times 10^{-1} \pm 3.0 \times 10^{-2}$
G3	$3.4 \times 10^{-2} \pm 9.4 \times 10^{-3}$	$6.6 \times 10^{-2} \pm 1.9 \times 10^{-2}$	$1.7 \times 10^{-1} \pm 3.7 \times 10^{-2}$
G4	$2.5 \times 10^{-2} \pm 3.8 \times 10^{-3}$	$1.6 \times 10^{-1} \pm 5.7 \times 10^{-2}$	$4.5 \times 10^{-2} \pm 1.2 \times 10^{-2}$
G5	$8.5 \times 10^{-2} \pm 4.3 \times 10^{-2}$	$8.8 \times 10^{-2} \pm 4.6 \times 10^{-3}$	$1.1 \times 10^{-1} \pm 3.2 \times 10^{-2}$

dominant. In set E, the $m = 1$ mode always has the highest energy, and as the amplitude of the centrifugal force increases, $E_{\text{mag}}^{m=0}$ decreases and so does $E_{\text{mag}}^{m=2}$. We do not see noticeable differences between runs E2 and E3, which have the same centrifugal force but were initialized at different times. This is also the case for runs E4 and E5, meaning no hysteresis is observed and the results are independent of the history of the run. In set F, we see that the energy in the $m = 0$ mode decreases, and in run F2

the $m = 2$ mode carries most of the energy. However, when the centrifugal force is increased further, the $m = 1$ mode becomes dominant once again.

In run G1 there is no clearly dominating mode, and the energy in the $m = 0$ mode is only roughly 5% larger than in $m = 1$. As the centrifugal force is first added in run G2, the energy of the $m = 0$ mode increases by about 10%. However, similarly to run F2, run G3 has most of the magnetic energy in the $m = 2$ mode,

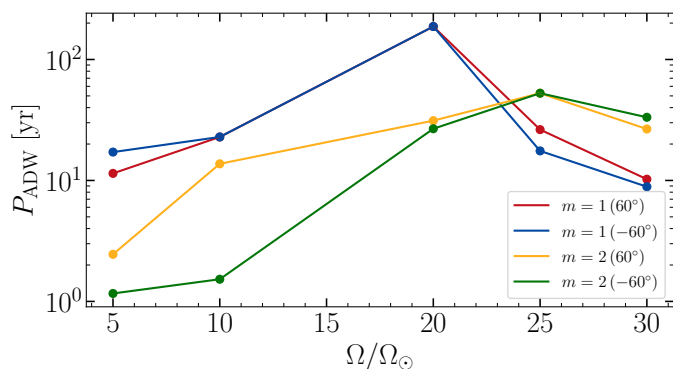


Fig. 4. Period of the ADWs as a function of the normalized rotation rate for runs without the centrifugal force.

which is about 66% higher than $E_{\text{mag}}^{m=0}$ and $E_{\text{mag}}^{m=1}$ combined. Increasing the centrifugal force further, we see that the dominant mode is $m = 1$, same as in the case of run F3. When the centrifugal force is switched off, the distribution of the energy goes back to levels nearer to run G1 with $c_f = 0$.

3.3. Azimuthal dynamo waves

We began by estimating the period of the ADWs by building a periodogram and identifying the signal with the greatest power as the main cycle. We then investigated whether there are tendencies between the period of the ADW and the rotation rate in runs without the centrifugal force. This is shown in Fig. 4. From $\Omega = 5\Omega_\odot$ to $\Omega = 20\Omega_\odot$, the period of the ADWs of the $m = 1$ and $m = 2$ modes seems to increase with rotation. For more rapid rotation, the period of the $m = 1$ ADW decreases, whereas for the $m = 2$ mode this tendency appears for $\Omega \geq 25\Omega_\odot$. For the two most rapidly rotating cases, the period of the $m = 2$ ADW exceeds that of the $m = 1$ mode.

To explore the migration pattern of the ADW, we show in Fig. 5 the $m = 1$ mode of the radial magnetic field near the surface at a latitude of 60° for runs C1, C3, D1, D3, E1, and E5, as well as the $m = 2$ mode for runs F1, F2, G1, and G3. Overplotted is the advection path due to differential rotation. In Table 3 we list the periods of the ADWs at $\theta = 60^\circ$ and the direction of the propagation.

In runs C1 and C3 we obtain a retrograde migration with no evidence of changes due to the centrifugal force. Both migration patterns appear to be constant in time with no interruptions. Similarly, the ADWs in runs D1 and D3 have a retrograde migration pattern but are characterized by a longer period. Run E1 has an interesting non-axisymmetric dynamo solution that shows periods of prograde and standing ADWs for the $m = 1$ mode. The migration of the ADW is changed by the centrifugal force, as evidenced by the panel for run E5. This run has a retrograde migration, similarly to sets C and D, and shows no similarity to run E1. As shown in Sect. 3.1, the change in the latitudinal differential rotation between runs E1 and E5 is about 17%. However, the ADWs propagate almost like rigid structures, so differential rotation cannot directly be used to explain their behavior. The precise origin of ADWs is unclear even in the case where the centrifugal force is absent, but quantities relevant for large-scale dynamos, such as differential rotation, kinetic helicity, and other turbulent quantities, along with their spatio-temporal profiles, likely play roles. However, the changes we observe when the centrifugal force is included suggest that subtle changes in the velocity field are enough to significantly alter the behavior of ADWs.

Table 3. Properties of the ADWs.

Run	P_{ADW} [yr]	Propagation
C1	11.44 $_{m_1}^*$	R
C2	9.64 $_{m_1}^*$	R
C3	8.48 $_{m_1}$	R
C4	8.80 $_{m_1}$	R
D1	22.88 $_{m_1}$	R
D2	22.45 $_{m_1}$	R
D3	19.73 $_{m_1}$	R
D4	21.60 $_{m_1}$	R
E1	>187.30 $_{m_1}$	S,P
E2	-	S
E3	>116.40 $_{m_1}$	R,P
E4	>64.07 $_{m_1}$	R
E5	>73.48 $_{m_1}$	R
F1	>52.64 $_{m_2}^\dagger$	R,P
F2	>35.84 $_{m_2}$	R
F3	>15.04 $_{m_2}$	R
G1	26.62 $_{m_2}^{*,\dagger}$	P
G2	40.74 $_{m_2}^{*,\dagger}$	P
G3	69.68 $_{m_2}$	R
G4	31.65 $_{m_2}^*$	R
G5	65.60 $_{m_2}^*$	P

Notes. Data were taken at latitude $\theta = 60^\circ$ for each run. The “greater than” symbol indicates that the period of the ADW is not covered in the simulated time. Asterisks denote a difference between the period of the ADW at the opposite latitude, and “ \dagger ” denotes nearly equally strong $m = 1$ and $m = 2$ signals. S, R, and P stand for standing, retrograde, and prograde propagation. In the case of Run E1, a wave with a period of about 80 years can also be identified.

In run F1 the wave is standing or very slowly migrating in a retrograde direction. The migration period seems to decrease as the centrifugal force is added in the lower panel of Fig. 6, where the wave travels about 120° in azimuth. Also evident here is the increase in the magnitude of the $m = 2$ mode at the southern hemisphere. It also seems that this part contributes the most to the change in magnetic energy seen in Fig. 3. It is only toward the end of the simulations that the $B_r^{m=2}$ at the northern hemisphere catches up and becomes comparable in strength to the southern hemisphere counterpart, as can be seen by comparing the panels of run F2 in Figs. 5 and 6.

In the rapidly rotating regime, the $m = 2$ mode of run G1 has a periodic wave with a period of about 26 years (see Table 3), with clear prograde propagation. The centrifugal force changes the propagation direction, as can be seen in the last panel of Fig. 5 (run G3), and the period of the ADW is also affected such that now it is about 70 years. In this case, the latitudinal differential rotation is doubled in run G3 as compared to run G1. Although this is the most obvious change between the simulations, it is difficult to explain the change in the ADWs with this alone, as discussed above.

In general, we find a preference for retrograde propagation, as in Viviani et al. (2018). Interestingly, however, run E1 shows a combination of standing and prograde waves and G1 is prograde. A subsequent study by Viviani & Käpylä (2021), where the prescribed heat conductivity was replaced by the Kramers opacity law, showed that there is a tendency of producing prograde-propagating ADWs. We replaced the fixed radial profile $K(r)$ with the corresponding quantity from Kramers opacity (see Eq. 6) and branched run E1 off to a new run, K1.

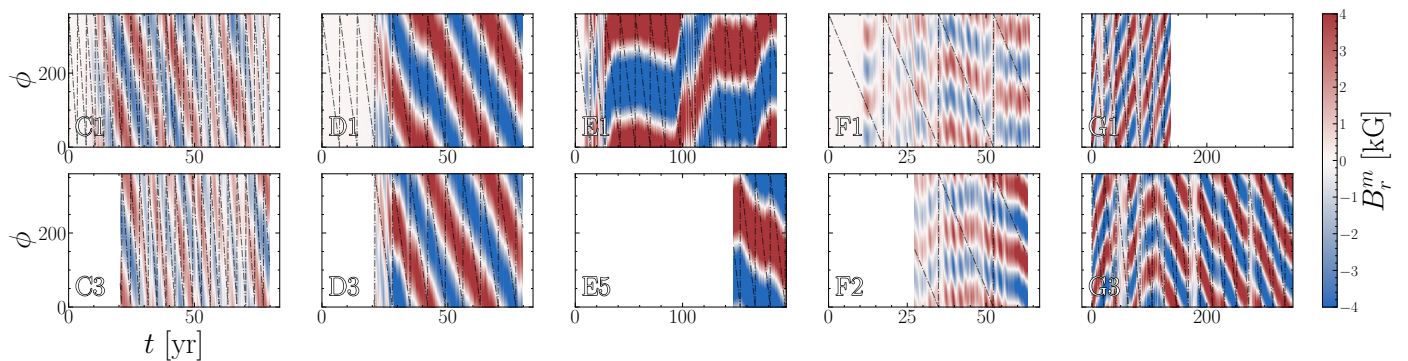


Fig. 5. ADWs for some selected runs at a latitude of $\theta = 60^\circ$. The top panels are the runs without the centrifugal force. The dashed line denotes the path that the ADWs would follow if they were advected by the differential rotation. For each set, we have added null data to make the time axes coincide in order to facilitate comparison.

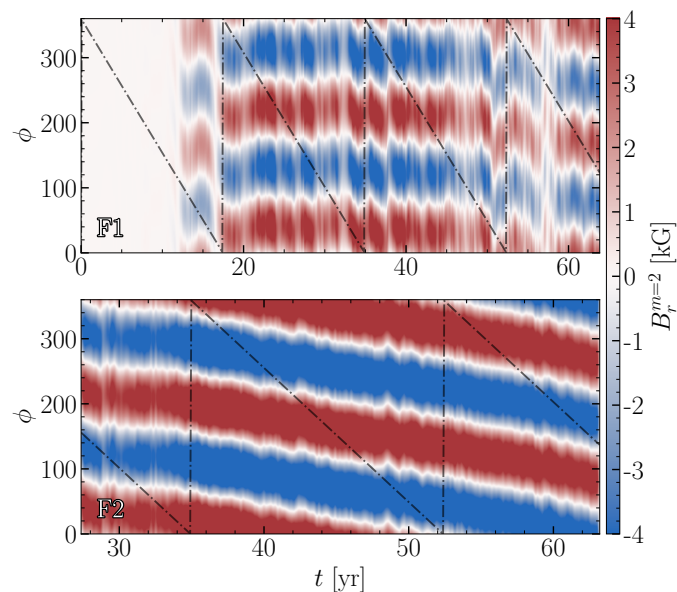


Fig. 6. Same as Fig. 5 but at $\theta = -60^\circ$ for runs F1 (top) and F2 (bottom).

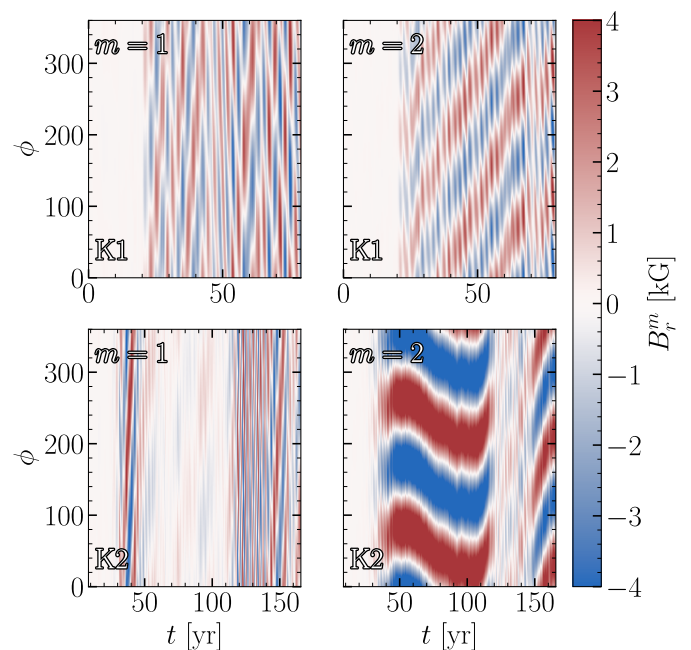


Fig. 7. ADWs for the runs with Kramers opacity without the centrifugal force (top) and with the centrifugal force (bottom).

The centrifugal force was added in run K2 with $c_f = 5 \times 10^{-4}$. Figure 7 shows the reconstructed $m = 1, 2$ modes for these two runs. It is clear that run E1 is different than K1, as the properties of the ADW are not reproduced when the Kramers opacity is used. In the latter case, the ADW is prograde for both $m = 1$ and $m = 2$ modes, which also have comparable energies. This is in accordance to Viviani & Käpylä (2021) in that it seems as if prograde migration is favored when the Kramers opacity is used. When the centrifugal force is added in run K2, the strength of the first non-axisymmetric mode decreases down to around 1 kG, but the direction of the propagation appears to be unaffected. Interestingly, the $m = 2$ mode increases from about 4 kG in run K1 to roughly 6 kG in run K2. The propagation pattern is interesting in that it seems to oscillate around a mean azimuth with an amplitude of 40° between $t = 40$ yr and $t = 110$ yr. After this, the strength of the $m = 2$ ($m = 1$) mode decreases (increases), and at around $t = 150$ yr the $m = 2$ mode reappears without a corresponding decrease in the $m = 1$ mode. In contrast to set E, the combination of Kramers opacity and the centrifugal force produces a dominant $m = 2$ mode, which was only found in the more rapidly rotating runs F2 and G3.

4. Summary and conclusions

In this paper we have studied the effects of the centrifugal force in semi-global dynamo simulations. It is important to assess its effects in the context of young solar analogs, which are used to study the Sun in an astrophysical context.

The amplitude of the centrifugal force is considered in our setup as a free parameter and is thus decoupled from the Coriolis term and the rotation of the star. In this way, its amplitude is artificially reduced by the control parameter c_f . This allows us to avoid an unrealistically large centrifugal force (Käpylä et al. 2013). This approach was applied to a total of 21 simulations divided into five sets, each characterized by a different rotation rate and with different values of c_f within each set. We find that the centrifugal force induces changes in the differential rotation and magnetic field only when rotation is rapid enough.

Both the latitudinal and radial differential rotation tend to increase with increasing centrifugal force. In the two most rapidly rotating runs without the centrifugal force, we obtained an anti-solar radial differential rotation. After including the centrifugal

force, this solutions changed to solar-like differential rotation. Namely, the outer layers of the convection zone went from rotating more slowly to more rapidly relative to the deeper layers. All of our runs have a solar-like latitudinal differential rotation, where high latitudes rotate more slowly than the regions nearer to the equator. This difference increases as the centrifugal force becomes stronger (see Fig. 1).

The magnetic energy, shown in Fig. 3, also shows noticeable effects only when the rotation is rapid enough in sets E, F, and G. All runs are dominated by the $m = 0$ mode in set C and by the $m = 1$ mode in set D, and they show small changes in energy as a function of the centrifugal force amplitude. In the rapidly rotating regime, it is common to find a dominating $m = 1$ mode, and the energy of the $m = 0$ and $m = 2$ modes decreases as c_f increases in set E. This trend is also present in sets F and G, with the difference that there are some cases where the $m = 2$ mode dominates.

By analyzing the ADWs near the surface of our runs, we find that the direction of the propagation changes from prograde to retrograde in some rapidly rotating runs as a function of the centrifugal force. This is most easily seen in runs E5 and G3 in Fig. 5. For run F2, we find that the direction of the propagation of the ADW is not clearly affected, but there are indications that its period might be affected (see Fig. 6).

To confirm the effects of the centrifugal force, we introduced three control runs. First, in order to test the importance of the initial conditions, we started run E3 (E5) with the same value of c_f as E2 (E4) from run E1 but at a different time. There are negligible differences in the differential rotation, as can be seen in columns 8 and 9 of Table 1 and in the overlapping points at constant c_f in Fig. 1. The magnetic energy is only slightly affected, as seen in the third panel of Fig. 3 from the data points at constant $c_f(\Omega/\Omega_\odot)^2$. Secondly, it is important to look at the solution of a run with the centrifugal force when it is turned off again. We did this experiment with run G3, in which the propagation of the ADW was retrograde (see the last panel of Fig. 5). When the centrifugal force was turned off, the propagation changed back to prograde, as it was in the original run, G1. Overall, the control runs show that the changes described above are due to the centrifugal force and not likely the outcome of the nonlinear evolution of the equations.

A previous study by Viviani & Käpylä (2021) shows that the propagation of the ADWs can be affected by the introduction of the Kramers opacity instead of a fixed radial profile of heat conductivity. We combined the Kramers opacity with the centrifugal force in runs K1 and K2 and find that, first, the solution of the ADW is different for the runs without the centrifugal force (K1) and with the centrifugal force (K2) as compared with the corresponding runs with the spatially fixed heat conductivity (set E). Notably, run K2 showed a migration pattern that was not obtained in any of the other runs (see Fig 7). This confirms that the Kramers opacity changes the ADW solution, but it is even more complex when the centrifugal force is included.

Despite our experiments, we were unable to identify the mechanism responsible for changing the behavior of the ADWs. The clearest change due to the centrifugal force is seen in the differential rotation, but its effect must be indirect through the dynamo mechanism because advection by a shear flow is incompatible with the practically rigidly propagating ADWs. The details of the dynamo process in 3D simulations are highly complex (e.g., Warnecke et al. 2021), and current mean-field methods are applicable only in the axisymmetric case. Observations, specifically an analysis of the surface magnetic field and its cycles as a function of rotation, could help us better understand this. Such

a study was performed by Lehtinen et al. (2016), who find that the photometric rotation period and activity period of a group of stars show clear differences. They proposed that this trend could be explained by the presence of prograde ADWs. However, our simulations suggest that when a prograde wave is affected by the centrifugal force, it changes to a retrograde propagation. Such a discrepancy could be better understood by extending the observations and by performing more realistic simulations in a wider parameter regime.

Acknowledgements. We thank the anonymous referee for their comments. FHN acknowledges funding from the Deutscher Akademischer Austauschdienst. FHN and PJK would like to thank the Isaac Newton Institute for Mathematical Sciences, Cambridge, for support and hospitality during the programme “Frontiers in dynamo theory: from the Earth to the stars” where work on this paper was undertaken. This work was supported by EPSRC grant no EP/R014604/1. PJK acknowledges the support from the Deutsche Forschungsgemeinschaft Heisenberg programme (grant No. KA 4825/4-1). PJK was also partially supported by a grant from the Simons Foundation. DRGS thanks for funding via the Alexander von Humboldt Foundation, Bonn, Germany. RB acknowledges support by the Deutsche Forschungsgemeinschaft (DFG, German Research Foundation) under Germany’s Excellence Strategy – EXC 2121 “Quantum Universe” – 390833306. The authors gratefully acknowledge the computing time granted by the Resource Allocation Board and provided on the supercomputer Lise and Emmy at NHR@ZIB and NHR@Göttingen as part of the NHR infrastructure. The calculations for this research were conducted with computing resources under the project hhp00052.

References

- Applegate, J. H. 1992, *ApJ*, 385, 621
 Brandenburg, A., Nordlund, A., & Stein, R. F. 2000, in *Geophysical and Astrophysical Convection*, 85–105
 Brown, B. P., Browning, M. K., Brun, A. S., Miesch, M. S., & Toomre, J. 2008, *ApJ*, 689, 1354
 Cang, T. Q., Petit, P., Donati, J. F., et al. 2020, *A&A*, 643, A39
 Cole, E., Käpylä, P. J., Mantere, M. J., & Brandenburg, A. 2014, *ApJ*, 780, L22
 Gastine, T., Yadav, R. K., Morin, J., Reiners, A., & Wicht, J. 2014, *MNRAS*, 438, L76
 Käpylä, P. J. 2021, *A&A*, 651, A66
 Käpylä, P. J. 2023, *A&A*, 669, A98
 Käpylä, P. J., Gent, F. A., Olsper, N., Käpylä, M. J., & Brandenburg, A. 2020, *Geophysical and Astrophysical Fluid Dynamics*, 114, 8
 Käpylä, P. J., Käpylä, M. J., & Brandenburg, A. 2014, *A&A*, 570, A43
 Käpylä, P. J., Mantere, M. J., Cole, E., Warnecke, J., & Brandenburg, A. 2013, *ApJ*, 778, 41
 Käpylä, P. J., Rheinhardt, M., Brandenburg, A., et al. 2017, *ApJ*, 845, L23
 Krause, F. & Rädler, K.-H. 1980, *Mean-field magnetohydrodynamics and dynamo theory* (Oxford, Pergamon Press, Ltd., 1980. 271 p.)
 Lehtinen, J., Jetsu, L., Hackman, T., Kajatkari, P., & Henry, G. W. 2016, *A&A*, 588, A38
 Matt, S. P., MacGregor, K. B., Pinsonneault, M. H., & Greene, T. P. 2012, *ApJ*, 754, L26
 Navarrete, F. H., Käpylä, P. J., Schleicher, D. R. G., Ortiz, C. A., & Banerjee, R. 2022a, *A&A*, 663, A90
 Navarrete, F. H., Schleicher, D. R. G., Käpylä, P. J., Ortiz-Rodríguez, C. A., & Banerjee, R. 2022b, *A&A*, 667, A164
 Navarrete, F. H., Schleicher, D. R. G., Käpylä, P. J., et al. 2020, *MNRAS*, 491, 1043
 Reiners, A., Shulyak, D., Käpylä, P. J., et al. 2022, *A&A*, 662, A41
 Skumanich, A. 1972, *ApJ*, 171, 565
 Viviani, M. & Käpylä, M. J. 2021, *A&A*, 645, A141
 Viviani, M., Warnecke, J., Käpylä, M. J., et al. 2018, *A&A*, 616, A160
 Völschow, M., Schleicher, D. R. G., Perdelwitz, V., & Banerjee, R. 2016, *A&A*, 587, A34
 Warnecke, J., Rheinhardt, M., Viviani, M., et al. 2021, *ApJ*, 919, L13
 Zaire, B., Donati, J. F., & Klein, B. 2022, *MNRAS*, 513, 2893

Chapter 6

Conclusions and Outlook

From the most simple theoretical grounds to the more detailed MHD simulations presented here, mounting evidence has revealed that the Applegate mechanism cannot adequately explain the observed eclipsing time variations. The required variations of the quadrupole moment are much larger than what we would expect in physical systems.

It was shown in Paper I that the origin of the quadrupole moment fluctuations are related to the different modes of the magnetic dynamo. However, the amplitude is too small to explain the observations. An important point is that these simulations did not include the centrifugal force, which is expected to play a key role in the Applegate mechanism. However, in Paper II it was found that the centrifugal force only plays a minor role in the quadrupole moment fluctuations.

However, an important step forward was taken by Lanza (2020). Lanza's model does no longer rely on the centrifugal force but on relaxing the assumption of tidal locking. By doing this, a persistent non-axisymmetric quadrupole moment of reasonable amplitude was found to be enough to explain the observations. We confirm this in Paper I by computing the non-axisymmetric quadrupole moment in one of our runs where we find that the computed period variations are of the same order of magnitude as the observed one for V471 Tau.

An interesting scenario arises where stellar magnetism can be linked to eclipsing time variations without the shortcomings of the Applegate mechanism. These eclipsing time variations can potentially be attributed to strong non-axisymmetric magnetic fields in the convective zones of magnetically active stars in post-common-envelope binaries. These magnetic fields tend to become stronger when the centrifugal force is included as presented in Paper III.

A few more steps can be taken to further make progress in the study of stellar magnetic fields through eclipsing times:

1. Solve Eq. (31), (32), or (35) of Navarrete et al. (2022) with N-body codes. Here

the idea is to present an independent way of proving the Lanza's mechanism and using the computed quadrupole moment variations of Paper I as a guide for more realistic variations.

2. Observationally prove if post-common-envelope binaries are tidally locked. Observations have shown that some close binaries are unsynchronized and this has been attributed to their past complex and dramatic history. Common envelopes may well fall in this category. Thus, the assumption of

Overall, the Lanza mechanism seems like a promising new way of explaining the connection between magnetic activity and eclipsing time variations. After a proper characterization, we could begin to draw some first conclusions about the internal magnetic fields of the active component in close binaries which show eclipsing time variations.

Bibliography

- Applegate, J. H. (1992). In: *ApJ* 385, pp. 621–629. DOI: 10.1086/170967.
- Applegate, James H. (1989). “Magnetic Activity and the Determination of the Tidal Synchronization Time in Close Binaries”. In: *ApJ* 337, p. 865. DOI: 10.1086/167157.
- Applegate, James H. and Joseph Patterson (1987). “Magnetic Activity, Tides, and Orbital Period Changes in Close Binaries”. In: *ApJL* 322, p. L99. DOI: 10.1086/185044.
- Beavers, W. I., T. J. Herczeg, and A. Lui (1986). “V471 Tauri: A Three-Body Orbit”. In: *ApJ* 300, p. 785. DOI: 10.1086/163855.
- Beuermann, K. et al. (2010). “Two planets orbiting the recently formed post-common envelope binary NN Serpentis”. In: *A&A* 521, L60, p. L60. DOI: 10.1051/0004-6361/201015472. arXiv: 1010.3608 [astro-ph.SR].
- Brandenburg, Axel (2001). “The Inverse Cascade and Nonlinear Alpha-Effect in Simulations of Isotropic Helical Hydromagnetic Turbulence”. In: *ApJ* 550.2, pp. 824–840. DOI: 10.1086/319783. arXiv: astro-ph/0006186 [astro-ph].
- Brandenburg, Axel and Kandaswamy Subramanian (2005). “Astrophysical magnetic fields and nonlinear dynamo theory”. In: *Physics Reports* 417.1-4, pp. 1–209. DOI: 10.1016/j.physrep.2005.06.005. arXiv: astro-ph/0405052 [astro-ph].
- Brinkworth, C. S. et al. (2006). “Detection of a period decrease in NN Ser with ULTRACAM: evidence for strong magnetic braking or an unseen companion”. In: *MNRAS* 365.1, pp. 287–295. DOI: 10.1111/j.1365-2966.2005.09718.x. arXiv: astro-ph/0510331 [astro-ph].
- Browning, Matthew K. et al. (2006). “Dynamo Action in the Solar Convection Zone and Tachocline: Pumping and Organization of Toroidal Fields”. In: *ApJL* 648.2, pp. L157–L160. DOI: 10.1086/507869. arXiv: astro-ph/0609153 [astro-ph].
- Bushby, P. J. et al. (2018). “Large-scale dynamos in rapidly rotating plane layer convection”. In: *A&A* 612, A97, A97. DOI: 10.1051/0004-6361/201732066. arXiv: 1710.03174 [astro-ph.SR].
- Dobler, Wolfgang, Michael Stix, and Axel Brandenburg (2006). “Magnetic Field Generation in Fully Convective Rotating Spheres”. In: *ApJ* 638.1, pp. 336–347. DOI: 10.1086/498634. arXiv: astro-ph/0410645 [astro-ph].

- Guinan, Edward F. and Ignasi Ribas (2001). “The Best Brown Dwarf Yet? A Companion to the Hyades Eclipsing Binary V471 Tauri”. In: *ApJL* 546.1, pp. L43–L47. DOI: 10.1086/318065. arXiv: astro-ph/0010487 [astro-ph].
- Hanasoge, Shravan, Laurent Gizon, and Katepalli R. Sreenivasan (2016). “Seismic Sounding of Convection in the Sun”. In: *Annual Review of Fluid Mechanics* 48.1, pp. 191–217. DOI: 10.1146/annurev-fluid-122414-034534. arXiv: 1503.07961 [astro-ph.SR].
- Hardy, A. et al. (2015). “The First Science Results from Sphere: Disproving the Predicted Brown Dwarf Around V471 Tau”. In: *ApJL* 800.2, L24, p. L24. DOI: 10.1088/2041-8205/800/2/L24. arXiv: 1502.05116 [astro-ph.EP].
- Hotta, H. and K. Kusano (2021). “Solar differential rotation reproduced with high-resolution simulation”. In: *Nature Astronomy* 5, pp. 1100–1102. DOI: 10.1038/s41550-021-01459-0. arXiv: 2109.06280 [astro-ph.SR].
- Jeffers, S. V. et al. (2022). “The crucial role of surface magnetic fields for stellar dynamos: epsilon Eridani, 61 Cygni A, and the Sun”. In: *A&A* 661, A152, A152. DOI: 10.1051/0004-6361/202142202. arXiv: 2201.07530 [astro-ph.SR].
- Jermyn, Adam S. et al. (2022). “An Atlas of Convection in Main-sequence Stars”. In: *ApJS* 262.1, 19, p. 19. DOI: 10.3847/1538-4365/ac7cee. arXiv: 2206.00011 [astro-ph.SR].
- Käpylä, P. J. et al. (2020). “Sensitivity to luminosity, centrifugal force, and boundary conditions in spherical shell convection”. In: *Geophysical and Astrophysical Fluid Dynamics* 114.1-2, pp. 8–34. DOI: 10.1080/03091929.2019.1571586. arXiv: 1807.09309 [astro-ph.SR].
- Käpylä, Petri J. et al. (2013). “Effects of Enhanced Stratification on Equatorward Dynamo Wave Propagation”. In: *ApJ* 778.1, 41, p. 41. DOI: 10.1088/0004-637X/778/1/41. arXiv: 1301.2595 [astro-ph.SR].
- Krause, F. and K. -H. Rädler (1980). *Mean-field magnetohydrodynamics and dynamo theory*.
- Kundra, Emil et al. (2022). “Variability of eclipse timing: the case of V471 Tauri”. In: *MNRAS* 517.4, pp. 5358–5367. DOI: 10.1093/mnras/stac2812. arXiv: 2210.01464 [astro-ph.SR].
- Kupka, Friedrich and Herbert J. Muthsam (2017). “Modelling of stellar convection”. In: *Living Reviews in Computational Astrophysics* 3.1, 1, p. 1. DOI: 10.1007/s41115-017-0001-9.
- Lanza, A. F. (2020). “Internal magnetic fields, spin-orbit coupling, and orbital period modulation in close binary systems”. In: *MNRAS* 491.2, pp. 1820–1831. DOI: 10.1093/mnras/stz3135. arXiv: 1911.01757 [astro-ph.SR].
- Lanza, A. F., M. Rodono, and R. Rosner (1998). “Orbital period modulation and magnetic cycles in close binaries”. In: *MNRAS* 296.4, pp. 893–902. DOI: 10.1046/j.1365-8711.1998.01446.x.

- Lanza, Antonino F. (2006). “Internal stellar rotation and orbital period modulation in close binary systems”. In: *MNRAS* 369.4, pp. 1773–1779. DOI: 10.1111/j.1365-2966.2006.10415.x.
- Lehtinen, Jyri J. et al. (2020). “Common dynamo scaling in slowly rotating young and evolved stars”. In: *Nature Astronomy* 4, pp. 658–662. DOI: 10.1038/s41550-020-1039-x. arXiv: 2003.08997 [astro-ph.SR].
- Lohsen, E. (1974). “Period variations of the white dwarf eclipsing binary BD +16 516.” In: *A&A* 36, pp. 459–460.
- Lurie, John C. et al. (2017). “Tidal Synchronization and Differential Rotation of Kepler Eclipsing Binaries”. In: *AJ* 154.6, 250, p. 250. DOI: 10.3847/1538-3881/aa974d. arXiv: 1710.07339 [astro-ph.SR].
- Marsh, T. R. et al. (2014). “The planets around NN Serpentis: still there”. In: *MNRAS* 437.1, pp. 475–488. DOI: 10.1093/mnras/stt1903. arXiv: 1310.1391 [astro-ph.SR].
- Muirhead, Philip S., Jason Nordhaus, and Maria R. Drout (2022). “Revised Stellar Parameters for V471 Tau, A Post-common Envelope Binary in the Hyades”. In: *AJ* 163.1, 34, p. 34. DOI: 10.3847/1538-3881/ac390f. arXiv: 2111.06905 [astro-ph.SR].
- Navarrete, Felipe H. et al. (2020). In: *MNRAS* 491.1, pp. 1043–1056. DOI: 10.1093/mnras/stz3065. arXiv: 1906.06787 [astro-ph.SR].
- Navarrete, Felipe H. et al. (2022). In: *A&A* 663, A90, A90. DOI: 10.1051/0004-6361/202243252. arXiv: 2102.11110 [astro-ph.SR].
- Ohlmann, Sebastian T. et al. (2016). “Hydrodynamic Moving-mesh Simulations of the Common Envelope Phase in Binary Stellar Systems”. In: *ApJL* 816.1, L9, p. L9. DOI: 10.3847/2041-8205/816/1/L9. arXiv: 1512.04529 [astro-ph.SR].
- Paczynski, B. (1976). “Common Envelope Binaries”. In: *Structure and Evolution of Close Binary Systems*. Ed. by Peter Eggleton, Simon Mitton, and John Whelan. Vol. 73, p. 75.
- Parker, Eugene N. (1955). “Hydromagnetic Dynamo Models.” In: *ApJ* 122, p. 293. DOI: 10.1086/146087.
- Popovas, Andrius, Åke Nordlund, and Mikolaj Szydlarski (2022). “Global MHD simulations of the solar convective zone using a volleyball mesh decomposition. I. Pilot”. In: *arXiv e-prints*, arXiv:2211.09564, arXiv:2211.09564. arXiv: 2211.09564 [astro-ph.SR].
- Pulley, D. et al. (2022). “Eclipse timing variations in post-common envelope binaries: Are they a reliable indicator of circumbinary companions?” In: *MNRAS* 514.4, pp. 5725–5738. DOI: 10.1093/mnras/stac1676. arXiv: 2206.06919 [astro-ph.SR].
- Reiners, A. et al. (2022). “Magnetism, rotation, and nonthermal emission in cool stars. Average magnetic field measurements in 292 M dwarfs”. In: *A&A* 662, A41, A41. DOI: 10.1051/0004-6361/202243251. arXiv: 2204.00342 [astro-ph.SR].

- Rincon, François (2019). “Dynamo theories”. In: *Journal of Plasma Physics* 85.4, 205850401, p. 205850401. DOI: 10.1017/S0022377819000539. arXiv: 1903.07829 [physics.plasm-ph].
- Schleicher, Dominik R. G. and Stefan Dreizler (2014). “Planet formation from the ejecta of common envelopes”. In: *A&A* 563, A61, A61. DOI: 10.1051/0004-6361/201322860. arXiv: 1312.3479 [astro-ph.EP].
- Tobias, S. M. (2021). “The turbulent dynamo”. In: *Journal of Fluid Mechanics* 912, P1, P1. DOI: 10.1017/jfm.2020.1055. arXiv: 1907.03685 [physics.flu-dyn].
- Vanderbosch, Z. P. et al. (2017). In: *20th European White Dwarf Workshop*. Ed. by P.-E. Tremblay, B. Gaensicke, and T. Marsh. Vol. 509. Astronomical Society of the Pacific Conference Series, pp. 571–574.
- Völschow, M., R. Banerjee, and F. V. Hessman (2014). “Second generation planet formation in NN Serpentis?” In: *A&A* 562, A19, A19. DOI: 10.1051/0004-6361/201322111. arXiv: 1312.7512 [astro-ph.EP].
- Völschow, M. et al. (2016). “Eclipsing time variations in close binary systems: Planetary hypothesis vs. Applegate mechanism”. In: *A&A* 587, A34, A34. DOI: 10.1051/0004-6361/201527333. arXiv: 1512.01960 [astro-ph.SR].
- Völschow, M. et al. (2018). “Physics of the Applegate mechanism: Eclipsing time variations from magnetic activity”. In: *A&A* 620, A42, A42. DOI: 10.1051/0004-6361/201833506. arXiv: 1809.00910 [astro-ph.SR].
- Wright, Nicholas J. and Jeremy J. Drake (2016). “Solar-type dynamo behaviour in fully convective stars without a tachocline”. In: *Nature* 535.7613, pp. 526–528. DOI: 10.1038/nature18638. arXiv: 1607.07870 [astro-ph.SR].
- Wright, Nicholas J. et al. (2011). “The Stellar-activity-Rotation Relationship and the Evolution of Stellar Dynamos”. In: *ApJ* 743.1, 48, p. 48. DOI: 10.1088/0004-637X/743/1/48. arXiv: 1109.4634 [astro-ph.SR].
- Wright, Nicholas J. et al. (2018). “The stellar rotation-activity relationship in fully convective M dwarfs”. In: *MNRAS* 479.2, pp. 2351–2360. DOI: 10.1093/mnras/sty1670. arXiv: 1807.03304 [astro-ph.SR].
- Zorotovic, M. and M. R. Schreiber (2013). In: *A&A* 549, A95, A95. DOI: 10.1051/0004-6361/201220321. arXiv: 1211.5356 [astro-ph.SR].